Lehigh University
Lehigh Preserve

Theses and Dissertations

2014

Modeling of the Structure of Disordered Metallic Alloys and Its Transformation Under Thermal Forcing

Ryan Paul Cress
Lehigh University

Follow this and additional works at: http://preserve.lehigh.edu/etd

Part of the Physics Commons

Recommended Citation
Cress, Ryan Paul, "Modeling of the Structure of Disordered Metallic Alloys and Its Transformation Under Thermal Forcing" (2014). *Theses and Dissertations.* Paper 1464.

This Dissertation is brought to you for free and open access by Lehigh Preserve. It has been accepted for inclusion in Theses and Dissertations by an authorized administrator of Lehigh Preserve. For more information, please contact preserve@lehigh.edu.

Modeling of the Structure of Disordered Metallic Alloys

and Its Transformation Under Thermal Forcing

by

Ryan Paul Cress

A Dissertation

Submitted to the Graduate Committee

Of Lehigh University

In Partial Fulfillment of the Requirements

For the Degree of

Doctor of Philosophy

In

Physics

Lehigh University

January 2014

© (2013) Copyright

Ryan Cress

Approved and recommended for acceptance as a dissertation in partial fulfillment of the requirements for the degree of Doctor of Philosophy

Ryan Cress

Modeling of the Structure of Disordered Metallic Alloys and Its Transformation Under Thermal Forcing

_____

Defense Date

_____

Yong W. Kim

Dissertation Director

_____

Approved Date

Committee Members:

_____

Yong W. Kim, Chairman

_____

James D. Gunton

_____

Michael Stavola

_____

Xiaolei Huang

_____

Dimitrios Vavylonis

Acknowledgements

I would like to first thank my advisor, Professor Yong W. Kim for his guidance over my time at Lehigh University. Before even entering graduate school he showed an eagerness to help me in my pursuit to become a physicist. The numerous lessons he has taught me over the past five years will stay with me forever, and I am truly grateful to have been able to learn under him. I would also like to thank my committee members, Professor Michael Stavola, James D. Gunton, Dimitrios Vavylonis, and Xioalei Huang, for their support and encouragement. Many students have helped in the progress of my dissertation work. I would especially like to thank Andrew Abraham and Jerry Kim for their initial work on 2-D RCP structure measurements, and Nathan Tomer for his work on the mechanical oven experiment.

I am lucky to have a strong support group of friends and family who have helped me more than they will ever know the past five years. I would like to thank my parents for their support, always allowing me to make my own decisions and pursue my passions. My brothers and sister have also always been there for me and provided encouragement. I will always appreciate my friends from Moravian College who always make my life interesting. I was also lucky enough to have a great relationship with many colleagues in the Lehigh physics department. For all these people in my life I will always be grateful.

Table of Contents

Table of Contents v

Table of Figures viii

Abstract 1

Chapter 1 Introduction 4

1.1 Motivation 4

1.2 Scope of Dissertation 7

1.3 Outline of Dissertation 10

Chapter 2 Thermal Transport in Disordered Alloys 14

2.1 Experimental Measurements of Transport Properties 14

2.2 Electronic Thermal Conductivity 15

2.3 Lattice Thermal Conductivity 17

2.4 Measurement Discrepancy in Nichrome 21

2.5 Grain Boundaries in Binary Alloys 27

Chapter 3 Random Close Packing 31

3.1 Introduction 31

3.2 Characterizing Random Close Packing 36

3.3 Two Dimensional Monodisperse Random Close Packing Simulation 39

3.4 Defect Detection 44

3.5 Crystal identification 46

3.6 Two Dimensional Binary Random Close Packing Simulation 48

Chapter 4 Mechanical Oven Experimental 53

4.1 Experimental Strategy 53

4.2 Experimental Apparatus 54

4.3 Driving the System 56

4.4 Measuring the Angle of Tilt 59

4.5 Illuminating the Bed of Spheres 62

4.6 Effect of the Baseplate 66

Chapter 5 Measurement of Experimental Data 67

5.1 Images Produced From the Mechanical Oven Experiment 67

5.2 Pre-Processing the Imaging Data 68

5.3 Identifying circle centers 71

5.4 Program Structure 77

5.5 Assessment 82

5.6 Uncertainty in Measurements 91

Chapter 6 Modeling Thermal Dissociation with the Law of Mass Action 94

6.1 Dissociation of Nano-Crystallites 94

6.2 Law of Mass Action Treatment 96

6.3 The Degree of Dissociation 98

6.4 Writing the Partition Function 101

6.5 Important Parameters 103

6.6 Calculating the Dissociation Potential 106

6.7 Fitting the Dissociation Potential as a Function of Nano-Crystallite Size 111

6.8 Morphology of the alloy structure 114

6.9 Number of Atoms in the Glassy Matter. 117

Chapter 7 Thermophysical Property Calculation 121

7.1 Thermal Conductivity 121

7.2 Treatment of Boundaries 123

7.3 Treatment of the Glassy Matter 126

Chapter 8 Summary and Conclusions 129

8.1 Summary and Conclusions 129

8.2 Future Research 130

List of References 132

Vita 140

Table of Figures

Figure 1.1 A comparison of lattice Thermal conductivity values of a copper –nickel alloy at room temperature 5

Figure 2.1- Measured Mass loss and W% concentration as a function of depth from the surface are compared for three different Nichrome specimens 24

Figure 2.2-Measured mass loss and W% concentrations are shown for two Nichrome specimens (Specimen 4 and 5) as a function of depth from the surface. 26

Figure 2.3-Overview from of thermal conductivity data for silicon films with varying microstructural quality and impurity concentrations. T 28

Figure 3.1 Phase diagram for the hard-sphere system[48] 33

Figure 3.2a. A plot of the order parameter Ψ versus volume fraction Φ. [53]

Figure 3.2b. A plot of the translational (T) versus orientational (Q) order parameters for the hard-sphere system (right). [53] 35

Figure 3.3 Example of 2-D RCP experimental data used in the characterization of the RCP system at different concentrations. 36

Figure 3.4 The four possible size 3 crystallites in a binary 2-D RCP 37

Figure 3.5-Experimental binary 2-D RCP crystallite size distributions for six binary concentrations. Degree of crystallinity γ shown for each distribution. 39

-Example of minimum crystallite that acts as a seed for the 2-D RCP building algorithm. 40

Figure 3.7 Example of shells being drawn around initial seed crystallite which will be used to form the contour of points where the next circle can be added to the cluster.. 41

Figure 3.8- Contour used for addition of next circle in 2-D RCP Building algorithm. Red points signify bindpoints which keep track of specific points used to add crystallite points to the structure. 42

Figure 3.9-Example of 2-D RCP structure built with basic building algorithm with one control parameter. 44

Figure 3.10-Example of defect formation in 2-D RCP structure algorithm. 45

Figure 3.11-Example of the role of defect detection in the 2-D RCP building algorithm. 46

Figure 3.12-Monodisperse RCP structure built with defect detection. Crystallites are identified by size and signified by filled colored circles. 48

Figure 3.13-Example of the two contours needed when building a binary RCP structure. 50

Figure 3.14- Binary RCP structure with crystallites identified by size and signified by filled colored circles. 51

Figure 3.15- Comparison of crystallite size distributions from (a) experimental 2-D RCP data and (b) trained 2-D RCP building algorithm simulation. 52

Figure 4.1-Schematic diagram of mechanical oven experimental apparatus.. 55

Figure 4. 2- Top view schematic of the mechanical oven experiment.. 58

Figure 4.3- Schematic ray diagram for measuring the angle of tilt. 60

Figure 4.4- Equivalent ray diagram for measuring the angle of tilt. 60

Figure 4.5 - Schematic diagram of the illumination of the bed for imaging. 62

Figure 4.6- Example of ambient light causing noncircular defects in the images..... 64

Figure 4.7- 2 figures taken at different illumination intensities highlighting the difference in circle radius seen when light saturation affects the imaging. 66

Figure 5. 1-Example of original image from 33 image burst taken with the apparatus 68

Figure 5.2- Example of image after preprocessing technique which results in a cropped image of the circle images prepared for the analysis software. 71

Figure 5.3-Example illustrating how the Hough transform can be used to find the center of a circle using the circles edge points. 72

Figure 5.4- Hough transform intensity map for the large diameter with the original edge data superimposed on top. 75

Figure 5.5 -Hough transform intensity map for the small diameter with the original edge data superimposed on top. 76

Figure 5.6- Schematic diagram of the programs operational procedure. 79

Figure 5.7-Graphical representation of the detected structure of the the image. Filled circles represent the crystallites detected in the image. 82

Figure 5.8-Velocity distributions for a 60 burst (1980 image) data run at the T* Speed setting. 84

Figure 5.9-Velocity distributions for a 60 burst (1980 image) data run at the 2T* Speed setting. 85

Figure 5.10- Velocity distributions for a 60 burst (1980 image) data run at the 4T* Speed setting. 86

Figure 5.11- Velocity distributions for a 60 burst (1980 image) data run at the 8T* Speed setting. 87

Figure 5.12-The degree of crystallinity of an equal number mixture of two different size spheres is shown at four different effective temperatures: (a)T* ; (b)2T* ;(c)4T*; and 8T*. 90

Figure 5.13-Affect of the Hough transform diameter on the calculated degree of crystallinity. 92

Figure 6.1-Initial room temperature crystallite size distribution for sample alloy $AuCu3$ 106

Figure 6.2- An example of a lattice built in accordance with the unit cell structure of the alloy. All atoms at a distance greater then the crystallite radius from the center of the lattice are removed in order to create a spherical crystallite. 107

Figure 6.3- Visualization of the dissociation potential calculation for a surface atom on a spherical crystallite.. 109

Figure 6.4-The three Lennard Jones-Potential interactions affecting a surface atom on a spherical crystallite of a gold copper alloy. 110

Figure 6.5-FCC unit cell structure for the $AuCu3$ alloy, used as the lattice structure to build the spherical crystallite. 111

Figure 6.6-Different sized $AuCu3$spherical nano-crystallites. 111

Figure 6.7-Example data for dissociation potential vs. nano-crystallite size for the $AuCu3$ alloy.. 113

Figure 6.8 –Fitting technique for example data for dissociation potential vs. nano-crystallite size for the $AuCu3$ alloy. 113

Figure 6.9-Evolution of the Crystallite Size distribution for the thermal dissociation of the $AuCu3$alloy..... 116

Figure 6.10-Evolution of the number of atoms in the glassy matter as a function of temperature for the $AuCu3$alloy. 118

Figure 6.11- Evolution of the degree of crystallinity as a function of temperature for the $AuCu3$alloy..... 119

Abstract

The morphology of disordered binary metallic alloys is investigated. The structure of disordered binary metallic alloys is modeled as a randomly close packed (RCP) assembly of atoms. It was observed through a 2-D binary hard sphere experiment that RCP structure can be modeled as a mixture of nano-crystallites and glassy matter. We define the degree of crystallinity as the fraction of atoms contained in nano-crystallites in an RCP medium. Nano-crystallites by size in a crystallite size distribution were determined experimentally to define the morphology of the RCP medium. Both the degree of crystallinity and the crystallite size distribution have been found to be determined by the composition of a given binary mixture.

A 2-D Monte Carlo simulation was developed in order to replicate the RCP structure observed in the experiment which is then extended to cases of arbitrary composition. Crystallites were assumed to be spherical with isotropic cross sections. The number of atoms in an individual crystallite in 2-D is simply transformed into the number of atoms in 3-D; we then obtain the crystallite size distribution in 3-D. This experiment accounts for the contribution from the repulsive core of the inter-atomic potential. The attractive part of the potential is recovered by constructing spherical nano-crystallites of a given radius from a crystalline specimen of each given alloy. A structural model of a disordered alloy is thus obtained.

With the basic structure of the RCP medium defined, the response to heating would be in the form of changes to the crystallite size distribution. This was first investigated in a hard sphere mechanical oven experiment. The experimental setup consists of a 2-D cell which is driven by two independent stepper motors. The motors drive a binary RCP bed of spheres on a slightly tilted plane according to a chaotic algorithmm. The motors are driven at four different speed settings. The RCP medium was analyzed using a sequence of digital images taken of the beds. The bursts of images provide a Gaussian distribution of particle speeds in x and y directions thus giving rise to the notion of "temperature." This temperature scales with the motor speed settings. The measured average degree of crystallinity is found to decrease as the effective temperature was raised suggesting that nano-crystallites dissociate under thermal forcing.

The evolution of a specimen's structure is calculated rigorously by means of the law of mass action formalism. A system of thermal dissociation reaction equations is written out for the set of nano-crystallites according to the 3-D crystallite size distribution. The equilibrium treatment is justified because the energy differences between metastable RCP structures fall within kT. Thermal dissociation of one surface atom at a time is assumed because the energy cost in dissociation of a surface atom on a nano-crystallite is significantly less than that of a multi atom cluster. The full set of reaction equations cover all possible dissociation steps, which may amount to several thousand for a disordered alloy specimen.

The primary determining factor in each of these dissociation equations is the dissociation potential or the amount of attractive energy needed to remove a surface atom on a nano-crystallite of a given size. The attractive potential between atoms is calculated using a Lennard-Jones potential between a pair of atoms for which quantum chemistry calculations exist in the literature. All interactions impinged on the surface atom by all other atoms in a crystallite are summed. As the nano-crystallites dissociate due to heating, the structure of the alloy changes, and this leads to modifications of alloy's transport properties. The model is found to predict the melting temperature of various disordered binary alloys as well as refractory metals in good agreement with known data. The structure model for disordered binary alloys gives an excellent characterization of the alloy morphology. It therefore provides fruitful avenues for making predictions about how thermophysical properties of disordered binary alloys change as the alloy temperature is raised by heating.

Chapter 1

Introduction

1.1 Motivation

Thermophysical properties of disordered metallic alloy specimens, such as thermal diffusivity, electrical resistivity, spectral emissivity and other properties, are modified under thermal, mechanical and chemical forcing applied to them. The degree to which such modifications are materialized depends on both the temperature and duration of heating as referenced to each specimen's melting point. The modification has serious consequences in utilization of metallic alloys in high-temperature and high-stress processes. Examples are found in nuclear and fusion reactors, chemical reactors, pyro-metallurgical processing environments and others. The thermophysical properties of alloys drift away from the design values, compromising the performance metrics or even leading to failures. An example of the problems faced in the characterization of disordered binary alloys can be seen in Figure 1.1. The figure shows a summary of room temperature experimental results for the lattice thermal conductivity of a disordered binary alloy system composed of the elements copper and nickel at different compositions. What can be seen are the differences between the different experimental results for the lattice thermal conductivity over a variety of alloy compositions at room temperature. These differences can be caused by impurities in the alloys as well as effects of thermal

history changing the thermophysical properties of the alloy. The figure also presents the most recent theoretical prediction of the lattice thermal conductivity.

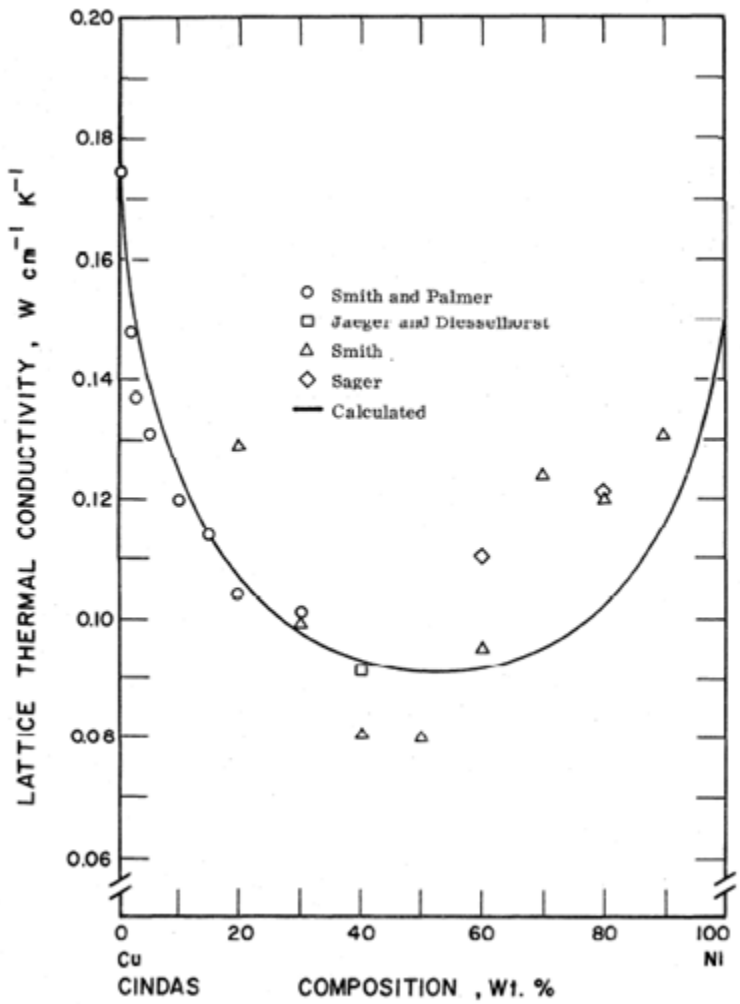

Figure 1.1 A comparison of lattice thermal conductivity values of a copper – nickel alloy at room temperature (300K) between calculated values from [9] and experimental data from Smith and Palmer[10], Jaeger and Diesselhorst [11], Smith [12], and Sager [13]

Two characteristic features effect alloy modification due to thermal forcing: enrichment of the more mobile atoms near the alloy surface, which has been demonstrated by direct measurement in simple alloys, [1, 2] and the morphological transformation as quantified in terms of nano-crystallite size distribution. These two factors influence the transport of mass, momentum, and energy because the exact nature of the pathways for transport of flux quanta through a given surface is determined by them. The latter feature is a precursor to alloy melting and the associated morphological transformation can be theoretically treated. This theoretical treatment will lead to a better understanding of the changing factors influencing the thermophysical properties of the alloy.

Our research has been pursuing the physical basis of thermophysical properties of simple metallic alloys. The proposition is that the changes in thermophysical properties are mediated by the changes in the size distribution of nano-crystallites due to redistribution of nano-crystallites by size at elevated temperatures. Transport of excitations through an alloy specimen entails two different material media and transmission of excitations across the interfaces between them. As the population of the crystallites undergoes changes, the rates of excitation transport through the specimen are modified. It has been shown for a number of different alloys that the thermal forcing results in changes of the specimen's elemental composition as a function of depth from the surface, distinctly different from the bulk composition.[3, 4, 5]

The theoretical understanding of the morphology of metallic binary alloys will contribute to the understanding of the factors influencing the changing thermophysical properties of the alloys. By establishing the state of the atomic structure of a disordered binary alloy we can estimate the structural contributions to the thermal transport inside the alloy. After setting up a model of how this structure will change as a function of temperature, we can model how the thermal transport will be affected by this change and move on to mapping out the changing thermophysical properties. The theoretical prediction of such changes will go a long way toward developing new materials and forecasting unforeseen structural failures in pre-existing materials.

1.2 Scope of Dissertation

The morphology of disordered metallic binary alloys is first approached through a structural characterization. This characterization is based on the observation of a RCP medium as a mixture of nano-crystallites and glassy matter. This provides a basis for the structure of the alloy. This differs from the polycrystalline structure used in recent analysis of alloy structure. The polycrystalline structure is defined by a mixture of grains and grain boundaries. [6] The objectives of the proposed dissertation research are to formulate a RCP model of hard spheres suitable for binary metallic alloys in terms of the size distribution of crystallites at room temperature and then to formulate a physical procedure to prescribe the evolution of the size distribution of crystallites under thermal forcing; The crystallite size distribution is measured in 2- and then transformed to produce a 3-D structure model. A law of mass action formalism is used to treat the evolution of this structure under thermal forcing. The

resulting structural morphology provides a basis for future exploration of the temperature dependant thermophysical properties of disordered metallic alloys.

In our work we take cues from previous work as well as add our own distinction to the model of RCP media. To begin, we make a numerical model that correctly maps RCP in 2-D. We use an algorithm to build the alloy structure based on a seed. This seed is the minimum-size crystallite. Our structure grows with a focus on its degree of crystallinity. There is a parameter that controls whether the next sphere added to the surface contributes to a crystallite. If the sphere does not contribute to a crystallite it is added at random to the surface of the structure. Using this parameter we are able to control the degree of crystallinity of the structure as well as the order. We explore binary mixtures of spheres which closely resemble Bernal's original hypothesis of hard sphere mapping of alloys [42]. This simulation generates a crystallite size distribution which can be transformed to 3-D and used as a basis of the room temperature structure of our disordered binary alloy.

In order for our simulation to be physically realistic, we have found it necessary to set the probability for placing a new sphere into a crystalline site versus a disordered site – that is, random numbers need to be picked from the output of the usual pink-noise random number generator. We have successfully made use of the images of a bed of spheres arranged at random. A large number of the images from the experiment were analyzed to find the average degree of crystallinity, on the one hand. RCP beds in 2-D were built by numerical simulation with a chosen value for the

probability of placing the next sphere to a crystalline site. The average degree of crystallinity was computed from the simulated beds of spheres. The procedure is repeated with different values of the probability until the average degree of crystallinity has been matched between experiment and simulation.

Once we have obtained the size distribution of crystallites within a disordered alloy specimen, we quantify the morphology of the alloy with a goal of understanding the thermophysical properties of the alloy. There are computational or molecular dynamics approaches attempted previously.[7, 8] A disordered metallic alloy as a RCP system of spheres consists of crystallites, glassy matter and the interfaces between them. The effect of changing temperature on the size distribution of crystallites was examined both by theory and by experiment with a vibrating 2-D bed of spheres. The bed is driven by two independent stepping motors in two mutually orthogonal directions on a nearly horizontal plane. A Maxwellian velocity distribution is realized for the spheres, providing a means to define and raise temperature. A sequence of photographs is taken to track the moving spheres and the images are analyzed to quantify how the RCP structure changes with increasing temperature. The experimental observations are used to guide the modeling of thermal dissociation of crystallites. The change in the size distribution of crystallites is the basis of the change in the morphology of the alloy specimen under thermal forcing.

The changes in the size distribution of nano-crystallites are modeled by means of the law of mass action formalism based on a set of reaction equations

representing the thermal dissociation of the nano-crystallites in the alloy structure. The structure is represented by a transformed 3-D RCP crystallite size distribution and the degree of crystallinity. The thermal dissociation is assumed to happen one atom at a time because the energy cost of the dissociation of a surface atom on a nano-crystallite is significantly less than that of a multi atom cluster. The primary factor in each of these equations is the dissociation potential or the amount of attractive energy experienced by a surface atom on a nano-crystallite of a certain size. As the structure evolves due to heating, the nano-crystallites dissociate thereby changing the structure of the alloy via the crystallite size distribution. The model shows good agreement with the melting temperature of various refractory binary alloys and pure metals. The evolution of the structure modeled with this law of mass action approach can be generalized to model the thermophysical properties for more complex alloys and their response to heating. The structural effect on thermal transport is discussed and a potential calculation technique for the thermal conductivity of the structure is presented.

1.3 Outline of Dissertation

In Chapter 2, thermal transport in binary alloys is discussed. Experimental results highlighting current results and the understanding of disordered alloys are presented, and theoretical approaches for predicting the transport properties in these alloys are summarized. The important parameters needed for predicting thermal conductivity are highlighted. This involves parameters needed in the calculation of both the electronic thermal conductivity and lattice thermal conductivity. The role of

disorder in thermal conductivity calculations and the shortcomings of the theoretical approaches are also discussed. The current method for characterization of binary alloys through a polycrystalline approach is explored. This method involves breaking the structure down into crystallite grains separated by grain boundaries. The role of these grain boundaries in thermal transport in the polycrystalline model is discussed.

In Chapter 3, the characterization of RCP media by both experiment and Monte Carlo simulation is discussed. This characterization centers on identifying crystallites in the RCP structure. After the crystallites are identified, the degree of crystallinity is calculated, and the crystallites are categorized by size to yield a crystallite size distribution. The Monte Carlo simulation of RCP media is discussed in detail, summarizing the algorithmic technique used to build this structure. This simulation starts with a seed crystallite and is expanded through a semi-random placement of surface particles in either crystalline points or into glassy matter points according to the parameter used to control the degree of crystallinity. The packing fraction is maintained in the RCP medium by means of a defect detection technique. The experimental results for RCP media are used to refine the parameters used in the Monte Carlo simulation; the final results show a good match between experiment and simulation.

In Chapter 4, the apparatus used in our mechanical oven experiment with 2-D RCP hard sphere media is explained. The goal of the experiment is to drive a RCP bed of spheres at various elevated temperatures. This is accomplished with a 2-D cell

of hard spheres that is driven with two orthogonal stepper motors; the motor drive is controlled with a pink-noise driving program in order to generate a Maxwellian velocity distribution for the spheres. The spheres are contained with a fixed boundary on a glass baseplate. To keep the hard spheres in close-packed contact with an RCP structure, the baseplate is slightly tilted, introducing a weak gravitational force in one direction. For data acquisition, the glass baseplate is illuminated from below for imaging purposes. The images are taken by a camera in a burst mode for multiple images in order to track the structure of the hard sphere bed and also to measure the velocities of the spheres from the sequential images in the burst.

In Chapter 5, the analysis of the data obtained by the experimental apparatus is discussed. The experiment produces bursts of images to be analyzed. The analysis involves first preparing the data for a Hough transform analysis, which requires detecting just the edge pixels of the spheres to be analyzed. The Hough transform analysis is then done to find the centers of the hard spheres in each image. With information on the centers of spheres in each image, the velocities are calculated for each sphere using two successive images in the burst. The structure for each individual image is analyzed to find all crystallites. We can then measure the degree of crystallinity and the crystallite size distribution for the structure. The structural data is determined as a function of the effective temperature of the experiment; the results are discussed.

In Chapter 6, the model for the evolution of the crystallite size distribution in a binary alloy according to the law of mass action is discussed. The initial structure of the binary alloy is set by the RCP structure for the given alloy composition. The crystallite size distribution is transformed to three dimensions and a set of law of mass action equations is written out to track the thermal dissociation of each nano-crystallite by size due to heating. Important factors in this calculation are discussed. Each dissociation step involves a surface atom dissociating from a nano-crystallite. Each law of mass action equation requires the calculation of the dissociation potential for a surface atom on a nano-crystallite of each size for the binary alloy in question. Results of this calculation are discussed, and the dissociation of nano-crystallites is compared with the melting temperature of the alloy that we modeled. The evolution of the crystallite size distribution is shown, which will give the basis for the evolution of the thermophysical properties of the alloy.

In Chapter 7, we discuss a potential calculation technique for the thermal conductivity of the RCP model of binary alloys. The calculation will depend first on estimates of the thermal transport in both the nano-crystallite portions of the RCP structure as well as the glassy matter portion. The boundary between nano-crystallites and glassy matter are represented by contact points for heat flow. The calculation of thermal conductivity will depend on the classification of these boundaries. To characterize these contact points, a treatment of the glassy matter is introduced into our RCP structure. This prepares our framework for a prediction of the thermal conductivity for our RCP binary alloy model as a function of the temperature.

Chapter 2

Thermal Transport in Disordered Alloys

2.1 Experimental Measurements of Transport Properties

Available experimental data on the thermal conductivity of solids is widely divergent with high amounts of potential fluctuation. This is mostly due to difficulties in accurate measurement of the thermal conductivity of solids as well as problems in characterization of the test specimens of such solids. In the case of disordered binary alloys, this causes serious gaps in experimental data with conflicting results for the thermodynamic property data that is available. Potential errors in measurement can arise from many different sources including: poor sensitivity of measuring devices, sensors, or circuits, specimen contamination, unaccounted for stray heat flows, and incorrect form factors. Perhaps the largest problem is the instability of the alloy itself, as experimentalists are often unsure of the classification of their specimen. [9] Thermal conductivity is a measure of the ability of a substance to conduct heat. Thermal energy is carried in alloys primarily by electrons and lattice waves. The total thermal conductivity is the sum of the electronic thermal conductivity due to transport of heat by electrons and the lattice thermal conductivity due to the transport of heat by the lattice waves. In alloys, both contributions to the total thermal conductivity are significant and it is necessary to estimate both. The dominant mechanism dictating the thermal conductivity in an alloy depends on the alloy temperature; because of this, different methods for estimating the thermal conductivity were established for different temperature regions.

2.2 Electronic Thermal Conductivity

At very low temperatures (<25K) the electronic thermal conductivity only has one major contributing factor which is the residual electronic thermal resistivity due to impurity scattering of electrons W_{e0},

$$k_e = \frac{1}{W_e} \approx \frac{1}{W_{e0}} = \frac{L_0 T}{q_0} \tag{2.1}$$

q_0 is the residual electrical resistivity, T represents the temperature, and L_0 is the classical theoretical Lorenz number which is a constant. Above 25K, and up to about 100K, the electronic thermal conductivity can be estimated for an alloy with Mathiessen's rule. The electronic thermal resistivity of the alloy is found with the formula

$$W_e = W_{e0} + W_{ei} = \frac{q_0}{L_0 T} + W_{ei} \tag{2.2}$$

$$k_e = \frac{1}{W_e} = \frac{1}{\frac{q_0}{L_0 T} + W_{ei}} \tag{2.3}$$

The second contributing factor at this higher temperature is W_{ei} or the intrinsic electronic thermal resistivity. At temperatures above 100K, deviations from Mathiessen's rule are covered by the Wiedemann-Franz-Lorenz Law. This law covers deviations in the residual electrical resistivity at higher temperatures, while also including deviations from the Lorenz number [14]. The corrected equation becomes

$$W_e = \frac{q - q_i}{LT} + W_{ei} \tag{2.4}$$

which gives an electronic thermal conductivity of

$$k_e = \frac{1}{W_e} = \frac{1}{\frac{q - q_i}{LT} + W_{ei}} \tag{2.5}$$

W_{ei} and q_i are the intrinsic thermal and electrical resistivities, they arise from the interactions between electrons and phonons. These interactions occur near the Fermi surface which is derived from the periodicity and symmetry of the crystalline lattice of the alloy. q_i is a result of horizontal movement of electrons through electron wave space on the Fermi surface. For the thermal resistivity W_{ei}, vertical and horizontal movements on the Fermi surface both contribute, these contributions can be added to calculate the total intrinsic thermal resistivity. The vertical movement on the Fermi surface is caused by the local property of the Fermi surface and is not changed drastically by changes in the overall structure of the alloy. The horizontal movement on the Fermi surface is due to motion of electrons over long distances on the Fermi surfaces, this is effected by both changes in the shape of the Fermi surface as well as boundaries on the Fermi surface [15]. In order to calculate these values it is necessary to use a virtual crystal approximation for ordinary metals. If transition metals are used in the alloy it is necessary to use Mott's theory to calculate the resistivities. [16, 17] Calculations of these values for various binary alloys have been covered in previous works. [18, 19] L is the Lorenz ratio which accounts for changes from the classical Lorenz number which results from electron-electron scattering and band structure

effects. The deviations from the classical Lorenz number can be expressed by calculating the absolute thermoelectric power S, which has been done for numerous binary alloys [20]

$$L = L_0 - S^2 \tag{2.6}$$

making the equation for electronic thermal conductivity

$$k_e = \frac{1}{\frac{q - q_i}{(L_0 - S^2)T} + W_{ei}} \tag{2.7}$$

This is an equation designed to calculate the electronic component of the thermal conductivity at intermediate temperatures, though the calculation faces problems in some instances. In the case of transition-metal alloys, the Lorenz ratio faces uncertainty due to very strong electron-electron scattering contribution to the electrical and thermal resistivity. [21] Other than the case of transition metals, values obtained from the Weidemann-Franz-Lorenz law have been found to be in good agreement with the values of the electronic component of the thermal conductivity of various alloys found experimentally [9].

2.3 Lattice Thermal Conductivity

The lattice component of the thermal conductivity is affected by different processes in different temperature ranges. At low temperatures, around five percent of the Debye temperature for an alloy, the lattice thermal conductivity is dominated by electron-phonon interactions and phonon scattering due to disorder. The thermal conductivity of a pure metal at low temperatures can be calculated by the equation

$$k_g = \frac{313 k_{ei} T^4}{n^{4/3} \theta^4} \tag{2.8}$$

In this expression, $k_{ei}$is the intrinsic electronic thermal conductivity, n is the number of conduction electrons per atom, and θ is the Debye temperature. The intrinsic electronic thermal energy has a T^{-2} temperature dependence in this temperature region, giving the lattice thermal conductivity a T^2 temperature dependence. This formula is only valid for non–transition pure metals with low residual resistivity, using this expression for alloys have been shown to give values greater than those measured experimentally. The reason for this discrepancy is postulated to be because of the high amount of phonon scattering due to disorder in an alloy [22]. At temperatures less than 0.5K it has been shown that the disagreement is greatly reduced. At these low temperatures the phonon wavelengths are so large that the effect of disorder scattering is greatly reduced [23]. Currently there is not an accurate way to estimate low temperature lattice thermal conductivity. A successful theory of the low temperature lattice thermal conductivity would have to involve better quantitative theory of phonon scattering due to disorder as well as a separate theory for transition metals and metals with high residual resistivity. Progress in this area has been approached with work accounting for disorder [24], though this work still does not include the problem faced with transition metals.

At intermediate temperatures, ranging up until about 20% of the Debye temperature, the problem of estimating the thermal conductivity becomes more

difficult. The same low temperature difficulties are still present in this intermediate range, also the resistive three-phonon anharmonic interaction in this region is significant and changes rapidly as a function of temperature. [9] There is not a method available to calculate the lattice thermal conductivity in this region currently.

At higher temperatures it is possible to neglect the effect of electron-phonon interaction for most alloys. The lattice thermal conductivity can then be estimated using a theory developed by Klemens[25] and Callaway[26]. The estimation uses the formula

$$k_g = k_u(T') \frac{I_2\left(\frac{\theta}{T}\right) + \frac{{I_4}^2\left(\frac{\theta}{T}\right)}{I_6\left(\frac{\theta}{T}\right) + \frac{I_8\left(\frac{\theta}{T}\right)}{{x_0}^2}}}{J_2\left(\frac{\theta}{T'}\right) + \frac{{J_4}^2\left(\frac{\theta}{T'}\right)}{J_6\left(\frac{\theta}{T'}\right)}} \tag{2.9}$$

$k_u(T')$ is the high temperature lattice thermal conductivity for an idealized virtual crystal in which each atom has the same mass and volume taken from the averages of the alloy elements. It is calculated with the formula

$$k_u(T') = \frac{{k_B}^2}{[2\pi^2\hbar(1+\alpha)B]}\left[J_2\left(\frac{\theta}{T'}\right) + \alpha\frac{{J_4}^2\left(\frac{\theta}{T'}\right)}{J_6\left(\frac{\theta}{T'}\right)}\right] \tag{2.10}$$

$\hbar$ is planck's constant, k_B is boltzmann's constant, B is a constant determined experimentally, and α is the ratio of reciprocal relaxation times for the two processes stemming from three-phonon anharmonic interactions in the alloy. In these equations, $J_n\left(\frac{\theta}{T'}\right)$ represents the standard transport integral

$$J_n\left(\frac{\theta}{T}\right) = \int_0^{\frac{\theta}{T}} \frac{x^n e^x dx}{(e^x - 1)^2} \tag{2.11}$$

$I_n\left(\frac{\theta}{T}\right)$ is the modified transport integral given by

$$I_n\left(\frac{\theta}{T}\right) = \int_0^{\frac{\theta}{T}} \frac{x^n e^x dx}{(e^x - 1)^2\left[1 + \frac{x^2}{{x_0}^2(1+\alpha)}\right]} \tag{2.12}$$

x_0 is the reduced frequency at which the reciprocal relaxation times for point-defect scattering and three-phonon anharmonic interactions are equal. It is calculated with the equation

$$x_0 = \frac{\hbar}{k_B}\sqrt{\frac{4\pi v^3 B}{a^3 \varepsilon T}} \tag{2.13}$$

v is the speed of sound, a^3 is the average volume per atom, and ε is a quantity that characterizes the perturbation due to mass defects and distortions of the lattice and is calculated by the expression [27]

$$\varepsilon = y_L\left[\frac{M_L - M}{M} + \gamma\left(\frac{V_L - V}{V}\right)\right]^2 + y_H\left[\frac{M_H - M}{M} + \gamma\left(\frac{V_H - V}{V}\right)\right]^2 \tag{2.14}$$

M and V are the average atomic mass and volume. y_L is the percentage of the lighter element in the alloy. M_L and V_L are the mass and volume of the lighter element. H subscripts correspond to the heavier elements. γ is the Gruneisen parameter, which is a weighted average of many separate parameters accounting for phonon nonlinearities.

The solution for the high temperature lattice thermal conductivity applies only to disordered solid-solution alloys. The calculation hinges on the availability of

experimental results for various parameters. The calculation also depends on the accuracy of the virtual crystal approximation of k_u. Overall, the theoretical approach to calculating the total thermal conductivity of a binary alloy can be improved significantly. The calculations depend on a virtual crystal approximation to handle disorder that has been shown to have significant deviation for some binary alloy nanocrystals [28].

2.4 Measurement Discrepancy in Nichrome

The method of LPP plume emission spectroscopy is described in detail in a number of publications. For the experimental data presented here, a single Q-switched, amplified Nd:YAG laser pulse is delivered onto the specimen's surface to drive an ablation front traveling into the bulk in pace with the thermal diffusion front. The resulting plasma plume is representative of the alloy, having the same composition as in the specimen's surface. The plume emissions are dispersed and captured through a high-dispersion spectrograph by a gated, intensified CCD array detector. For the present round of analyses, the laser pulse of 20-ns duration is used at pulse energy of 0.4 J. The footprint of the LPP plume is oblong in shape at the specimen surface and its image is focused on the entrance slit plane of the spectrograph (Jarrell Ash Model 82–479).

The LPP plume spectra are captured in the 2-D array detector during a 400-ns period beginning at 180 ns after the initiation of the LPP plume in a vacuum. The captured spectral image consists of 256 full plasma emissions spectra, each at 1024 discrete but contiguous wavelengths, emanating from different positions of the LPP

plume along the long axis of the slit. Two sets of atomic emission lines from nickel and from chromium are calibrated in two different ways: one for the difference in emission line intensities between the two species; and another for the respective intensities as a function of masses of the two atomic species entrained within the plasma plume. The first calibration consists of determining the emission intensities of the respective emission lines emitted by LPP plumes from a fresh alloy specimen whose atomic composition is known. The calibration is applied to the entire chain of optics, ranging from the imaging optics, the entrance slit and reflective optics internal to the spectrograph and the electro-optics responsible for gating and intensification of LPP plume emissions to the CCD array as the repository of the LPP plume spectra. The second calibration entails measuring the average mass loss per laser pulse by dividing the mass change resulting in a specimen due to exposures to several hundred LPP shots by the number of laser pulses; a digital microbalance (Mettler Toledo Model UMT2) is used for this purpose. After the two rounds of calibration, both the elemental composition and mass loss per LPP shot are determined solely by spectroscopic means.

For this purpose, two emission lines at 440.155 nm and 471.442 nm are used for nickel concentration determination and three at 425.435 nm, 427.48 nm and 428.972 nm are used for chromium. Due to the particular criterion under which the physics of LPP ablation is established, the mass loss is governed by the local thermal diffusivity, subject to the heat of formation needed to release constituent atoms from the solid phase and the ability of the atomic species to disperse away from the surface.

It has been experimentally established that the thickness of the layer of the ablated target matter is dependent on the above physical attributes of the specimen bulk according to the following scaling relation:

$$\theta = C D_T^{\alpha} M^{\beta} H_f^{\gamma} \tag{2.15}$$

where θ is the material thickness ablated in cm; D_T is the thermal diffusivity in $cm^2 s^{-1}$; M is the molar weight; and H_f is the heat of formation in $J \cdot g^{-1}$. For specimens placed in a vacuum, we have $C = 11.07 \pm 0.45$; $\alpha = 0.91 \pm 0.01$; $\beta = -\alpha$; and $\gamma = -1$. [29, 30]

Figure 2.1 shows the measured mass loss per laser pulse and W% concentrations of nickel and chromium as a function of the number of the successive LPP runs generated at the same surface location. The succeeding ablations provide the elemental composition as a function of depth from the surface. The mass ablated from the surface per laser pulse varies due to changes in the thermophysical properties of the specimen during the period of heating and cooling but on average it is of the order of 0.4 μg per pulse. The figure shows the responses for three different specimens that have been thermally forced by three different mechanisms. Specimen 1 was heated by a digitally controlled electric oven (Fisher Muffle Furnace).

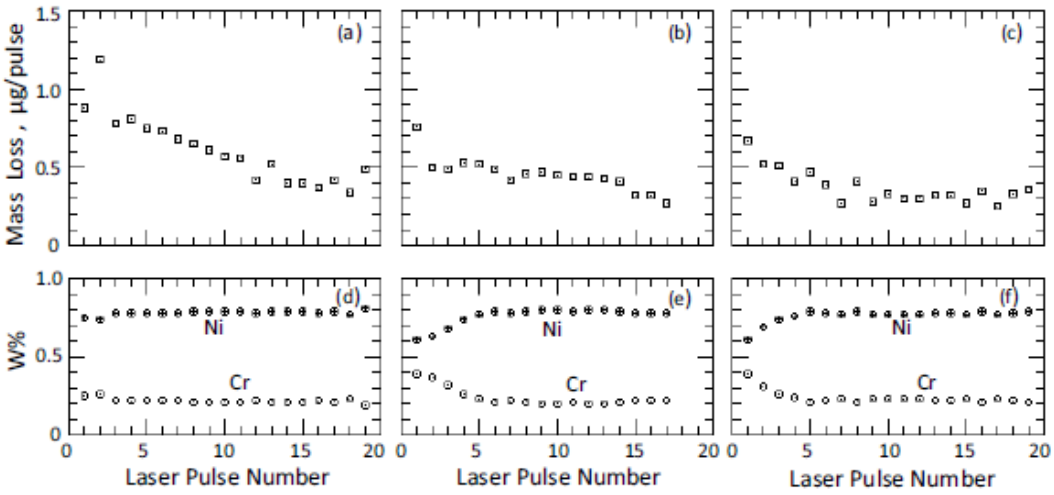

Figure 2.1- Measured Mass loss and W% concentration as a function of depth from the surface are compared for three different Nichrome specimens: i) mass loss (a) is shown as a function of LPP shot number, together with W% concentrations (d) of nickel and chromium, respectively, are shown for Specimen 1, which had been heated to 1086K for 120 minutes in the furnace; ii) mass loss (b) and W% concentrations (e) are shown for Specimen 2, which had been heated to 1111K by AC current for 120 minutes; and iii) mass loss (c) and W% concentrations (f) are shown for Specimen 3, which had been heated to 1127K by DC current for 120 minutes.

The maximum temperature was set at 1086 K. The specimen was placed on a short piece of 25-mm diameter alumina tubing resting on the furnace floor. During the ramp-up period, the temperature was raised from room temperature at the rate of 20 K per minute until the set temperature was reached, and the temperature was maintained for 120 minutes before the furnace was powered off. The furnace was allowed to cool to room temperature over the next two-hour period; the specimen remained within the furnace. A slow flow of argon was maintained in order to purge air out of the furnace during the entire heating run. Figure 2.1(a) shows the measured ablative mass loss for

each LPP plume as a function of the number of successive laser pulses delivered to the surface; the corresponding W% concentration of nickel and chromium are shown in figure 2.1(d). Specimen 2 was heated electrically by AC current running through the specimen at 1110 ± 20 K for 120 minutes.

The specimen was mounted on the specimen holder within the vacuum feed-through, which was in turn placed under vacuum. The results of mass loss measurements are shown in figure 2.1(b) and the measured W% concentrations of nickel and chromium are given in figure 2.1(e), respectively. Specimen 3 was heated also electrically but by DC current at 1128 ± 20 K for 120 minutes. The measured mass loss and W% concentrations for nickel and chromium are shown in figure 2.1(c) and figure 2.1(f), respectively. A comparison of the properties of the thermally forced specimens by the different heating methods reveals that the rate of mass loss by the LPP process is modified significantly at a much higher rate than the rate of modification of the near-surface composition profile. Heating increases the thermal diffusivity of the specimen by annealing – that is, a process by which small deviations of individual atoms from their respective equilibrium positions relative to neighboring atoms by virtue of increased thermal fluctuations of the individual atoms. Enrichment near the surface of chromium atoms, the less massive, more mobile of the two constituent atomic species, takes place much more slowly in the presence of heating alone. When the specimen is heated by an electrical current, the near-surface enrichment process seems to be accelerated; this suggests specific roles being played by the charge carriers. Judging from the shape of the W% concentration profiles of

nickel and chromium, the enrichment of chromium at the surface seems to proceed a bit faster by AC heating than by DC heating; in the case of AC heating, the surface enrichment exhibits the sign of saturation, indicating the diffusion of chromium back toward the bulk medium is in effect.

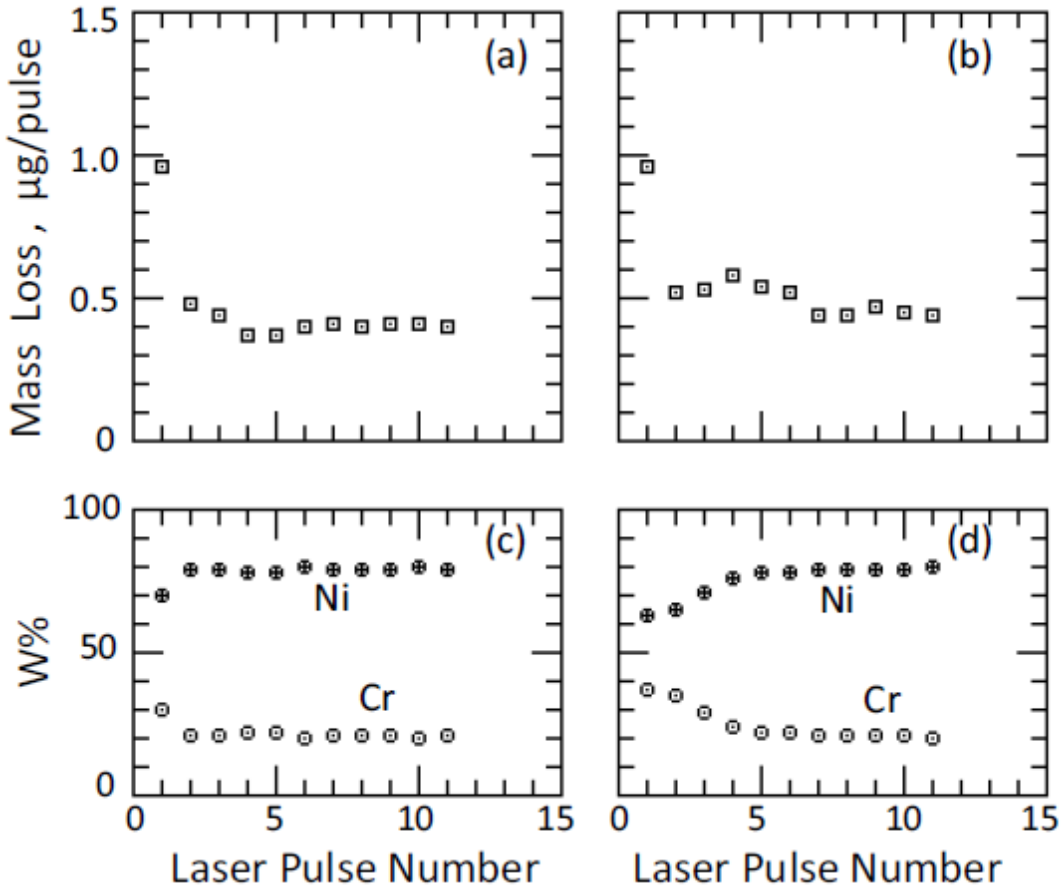

Figure 2.2-Measured mass loss and W% concentrations are shown for two Nichrome specimens (Specimen 4 and 5) as a function of depth from the surface. Both specimens had been heated by AC current but to two different peak temperatures: i) mass loss (a) and W% concentrations (c) of nickel and chromium, respectively, for Specimen 4, which had been heated to 1128K for 127 minutes, and ii) mass loss (b) and W% concentrations (d) for Specimen 5, which had been heated to 880K for 132 minutes.

Figure 2.2 shows the results of measurements with specimens designed to gauge the temperature dependence of the near-surface chromium enrichment rate. Both Specimen 4 and 5 were heated by two different AC currents: Specimen 4 at 15 A and Specimen 5 at 22.5 A. In addition, the leading end of the specimen holder was kept in contact with a brass block that was cooled by circulating water at room temperature. The specimen temperature was measured by bringing an alumel-chromel thermocouple junction into contact with the specimen as a function of position along the length of the specimen at 2.5 mm intervals. The mass loss per laser pulse as a function of the number of laser pulses is shown in figure 2.2(a) for Specimen 4 that was heated to 880 ± 15 K for 132 minutes; W% concentrations of nickel and chromium, respectively, are shown in figure 2.2(c). The corresponding results are shown for Specimen 5 in figure 2.2(b) and figure 2.2(d) that had been heated to 1128 ± 20 K for 132 minutes. The results shown in Fig. 2.2 indicate that the mass loss profile develops relatively quickly by increasing the thermal diffusivity by the effect of the annealing process but with only a weak dependence on temperature, however. On the other hand, development of the near-surface enrichment of chromium proceeds more quickly in Specimen 5, showing stronger dependence on thermal-forcing temperature.

2.5 Grain Boundaries in Binary Alloys

More recent work in understanding the properties of binary alloys has focused on viewing binary alloys as polycrystalline materials. In the context of binary alloys, the polycrystalline model suggests crystallite grains separated by grain boundaries. In

such a material the role of the interface physics between crystallites begin to dominate the transport properties of the alloy. [31] Because of the high density of grain boundaries, recent efforts have focused on controlling the formation of grain boundaries in order to produce more stable binary alloys for high temperature processes [32]. Grain boundaries are found at the interface between two grains, in the case of polycrystalline materials this occurs at the interface between crystallites. In silicon thin films the roles of grain boundaries in polycrystalline thin films and single crystal thin films has been explored in detail showing that poly-crystal silicon conductivities are reduced compared to those of pure crystalline films [33].

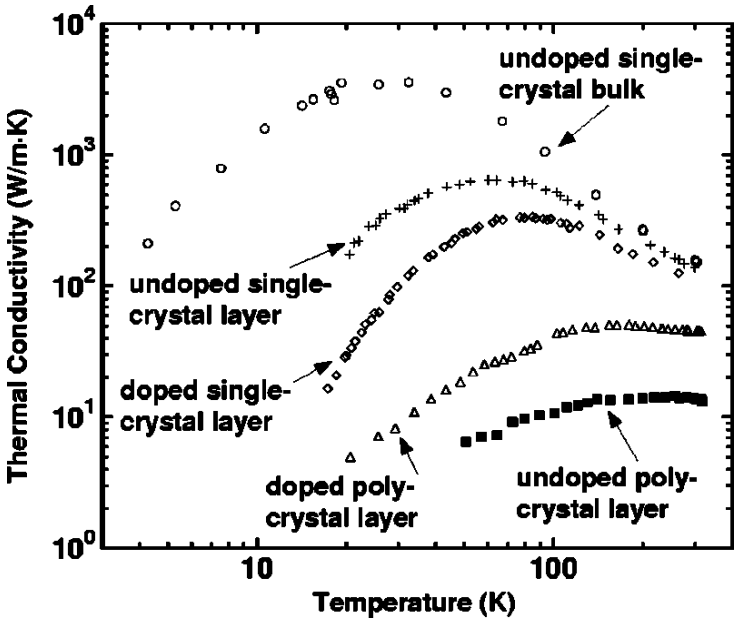

Figure 2.3-Overview from [34]of thermal conductivity data for silicon films with varying microstructural quality and impurity concentrations. The data illustrates the effect of impurity phonon scanning versus grain boundary phonon scattering. The data for undoped single-crystal bulk samples are taken from [35]. Both single crystal films have thickness of 3 µm, and for the doped

film, a boron concentration of $10^{19}\ cm^{-3}$.[36] The undoped and doped($1.6\ x\ 10^{19}\ cm^{-3}$) polycrystalline films have grain sizes of 200 and 350nm, respectively [37, 38]

The problem is that the roles of impurities in the crystallites and the role of grain boundaries are difficult to separate. In evaluating grain boundaries it is important to evaluate the grain boundary energy γ, which can be calculated by [39]

$$\gamma = \gamma_0 - \Gamma(\Delta H_{Seg} + kTlnX) \tag{2.16}$$

γ_0 is the pure material energy which is lowered by Γ which is the saturation at the boundary of one alloy element. This is multiplied by the sum of the enthalpy of segregation ΔH_{Seg} and the product of the thermal energy kT and lnX where X is the composition of the alloy. Since these boundaries play such a large role in the thermal transport in a polycrystalline material it is important to understand the boundary energy. The important parameter in the boundary energy equation is the enthalpy of segregation which can be calculated based on the elements contained in a binary alloy [32]. The formula for this calculation is

$$\Delta H_{Seg} = z\left[\omega_c - \frac{\omega_{gb}}{2} - \frac{\left(\Omega^B\gamma^B - \Omega^A\gamma^A\right)}{2zt}\right] \tag{2.17}$$

ω_c and ω_{gb} are bond energies for the crystal and grain boundaries that are collected into interaction parameters. Ω^B and Ω^A are the atomic volume of the two different elements of the binary alloy. Z is the coordination number and t is the mean grain boundary thickness.

These various methods developed for handling the thermal transport in binary alloys have the potential for improvement in their predictive capabilities. The theoretical efforts suffer from short comings mostly created by the lack of information about the inner structure of the alloy, and specifically how to deal with the disorder present in the alloy. Recent efforts have focused on the polycrystalline model for handling the structure of the alloy, in this model it is tough to tell the difference in contributions between the large grain boundaries and the disorder present in the grains themselves. A more complete structure model for binary alloys would be beneficial in the quest to obtain a complete understanding of thermal transport in binary metallic alloys.

Chapter 3

Random Close Packing

3.1 Introduction

Since complex metallic alloys were first introduced as a material, physicists have been interested in learning how the atoms in such metals arranged themselves. An understanding of the inner structure would also lead to further understanding of the properties of such metals. In this context, Bernal first imagined the atoms that made up an alloy as different sized hard spheres, the radii of the spheres corresponding to the atomic radius of the atoms of the alloy. The alloy was imagined as a random assembly of these hard spheres.[40]

Studying the packing of spheres has a long history because of its ability to serve as a simple but useful model for a variety of physical systems. [41] The molecular nature of fluids and glasses have also seen contributions from hard sphere packing. [42,43] Dense packing of hard spheres is generally seperated into three separate subclasses: ordered close packing, random close packing, and random loose packing. Ordered close packing in three dimensions consists of periodic symmetry coming from a set unit cell structure, and accounts for the highest density of hard spheres. [44] Random close packing has historically been studied experimentally by filling a container with hard spheres at random and shaking the container to achieve a maximum random packing. [45] Random loose packing is the result of not shaking the container creating a less dense version of random close packing. [46]

Berryman formalized random close packing (RCP). In order to have a randomly close packed structure, it was required that all spheres be arranged at random and that the structure filled a volume at maximum density where all spheres are in contact with another sphere.[47] Berryman also reported a packing fraction of 0.64 on average for RCP in three dimensions. He found that random loose packing is in some sense less fundamental than the concept of random close packing, as the definition of random loose packing requires a minimum density below which the configurations of the structure are unstable and therefore not "packed". As packing fraction increases the phase of the matter being simulated changes, as shown in Fig. 3.1. The lowest branch corresponds to the liquid phase, a packing fraction of around 0.49 corresponds to the freezing point. Packing fractions greater than 0.49 correspond to a solid phase. We are interested in the metastable branch equivalent to a mixed phase of disordered glassy arrangements and ordered crystallites. This branch will provide a foundation for the structure of disordered alloys. The metastable branch is an extension of the liquid phase and extends to the random close packed state.[48]

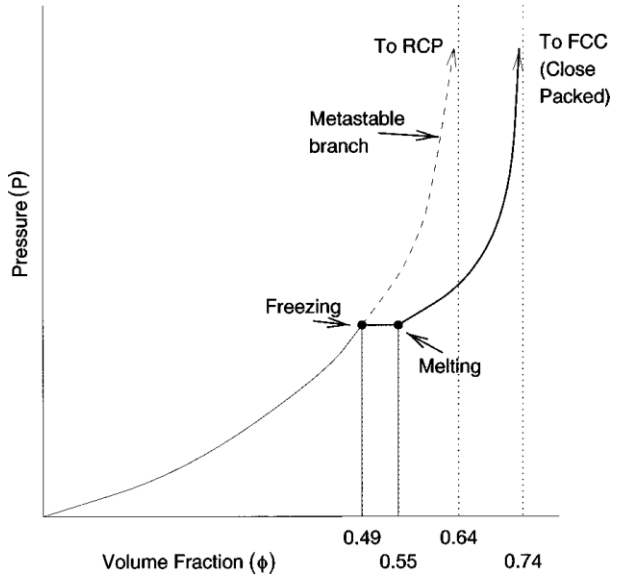

Figure 3.1 Phase diagram for the hard-sphere system[48]

Two different algorithms have been developed to simulate random packing. The first algorithm starts with choosing a number and size for the spheres that would satisfy the desired packing fraction in a given volume. Each sphere is given a random initial position, and this causes many overlaps among the spheres initially. The spheres are then moved until the structure contains no overlaps.[49] The second algorithm starts from a seed. Spheres are randomly positioned but in contact with the surface of the seed until a given volume is filled. The reason for development of the second algorithm is that the first became more and more computation-intensive the higher the packing fraction became. The density is controlled by tracking the average coordination number. The coordination number for a given sphere represents the number of neighboring spheres in contact with its surface. The higher the average coordination number is, the more dense the packing will be.[50]

There have been several attempts at analyzing and identifying RCP structure. The early computer models used a pair distribution function to map the structure of the random packings.[51] The pair distribution function measures the average density of spheres at a certain radial distance from a given sphere. The pair distribution function is still frequently used in classifying RCP media, but there is a lot more information about the RCP structure than the pair distribution function captures. Another analysis of the short range order is the Voronoi analysis. A Voronoi cell of a given sphere includes all points that identify this sphere's center as being the closest. The size and shape of a Voronoi cell for a given sphere provides rich information regarding its local order, including the statistics of different neighboring spheres.[52]

There is a criticism that RCP models should not be studied in great detail because they lack a solid definition. Torquato argues that the packing fraction for a RCP medium is not concrete and varies in the neighborhood of 0.64 because of different physical properties the model is subject to. To remedy this deficiency, Torquato proposes a state of maximum random jamming. The change in the model introduces an order parameter for controlling the structure of the random arrangement, measuring the number of spheres in the structure that are jammed. A sphere is considered jammed if it has no freedom to move while all other spheres remain stationary. A maximal random jammed state is then described as the state with minimum order, i.e., being at a state with a packing fraction of 0.64. [53]

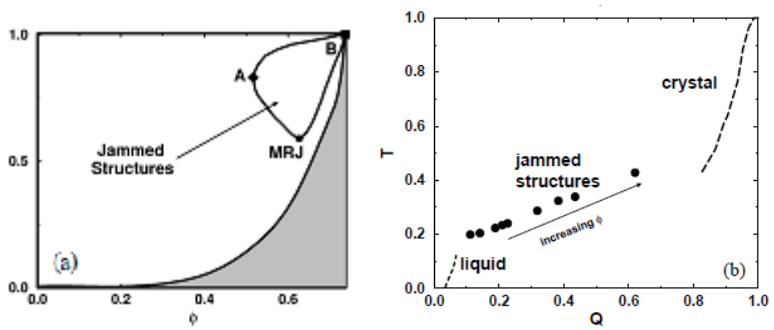

Figure 3.2a. A plot of the order parameter Ψ versus volume fraction Φ. [53]
Figure 3.2b. A plot of the translational (T) versus orientational (Q) order parameters for the hard-sphere system (right). [53]

Without introducing a new model, the order within an RCP model can be defined by means of the degree of crystallinity of the structure. The degree of crystallinity is the total fraction of spheres in the structure that have arranged themselves as part of small crystallites in contrast to glass-like strucutures. These crystallites can be distinguished as being in a tetrahedral form made by four spheres. This tetrahedral form is the smallest sized crystallite that can be formed in an RCP structure.[54] As it turns out, the degree of crystallinity of a structure has a high dependence on the packing fraction.

Larger crystallites can also form in the structure. These polytetrahedral shapes can take many different forms depending on how many spheres constitute the crystallite. One measure of the size of a crystallite is the number of spheres within the crystallite; the degree of crystallinity does not include this information.[55]

3.2 Characterizing Random Close Packing

The structure we will use as the basis for the arrangement of atoms in a binary alloy will be based on random close packing. Our first step in characterizing an RCP medium was to develop a hard sphere experiment to reproduce and characterize the structure. Hard spheres of two distinct sizes were placed in a container and images of the spheres were taken with the random arrangement reset between photos. An example of the data analyzed is shown in figure 3.3.

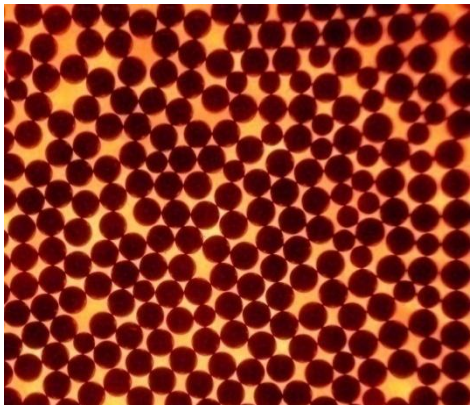

Figure 3.3 Example of 2-D RCP experimental data used in the characterization of the RCP system at different concentrations.

With some investigation, we realized that binary RCP systems could be characterized by splitting the spheres into two groups: nano-crystallites and glassy matter. In two dimensions we define a crystallite as a minimum of three hard spheres that are mutually in contact. For a binary mixture this introduces four possible nano-crystallites of the smallest size 3

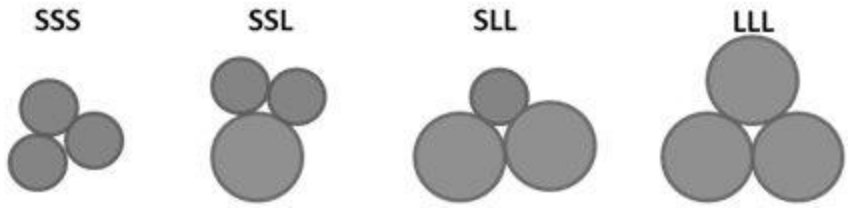

Figure 3.4 The four possible size 3 crystallites in a binary 2-D RCP

The pictures were first analyzed by identifying the crystals by eye and recording the data for each bed of spheres at each binary composition. This ensured confidence in the data, but was slow compared to computational approaches. Initial attempts at computer analysis for these images made the data more easily processed though the error in the results was concerning. Hard sphere data were successfully obtained and analyzed for six different binary hard sphere compositions.

The experimental data were investigated and different sized crystallites were identified and documented. After an entire photo was analyzed we define the degree of crystallinity as

$$Degree\ of\ Crystallinity = \frac{Number\ of\ Spheres\ Belonging\ to\ Nano - Crystallites}{Total\ Number\ of\ Spheres\ in\ the\ System} \qquad (3.1)$$

The degree of crystallinity is one important characterization of the RCP structure. To distinguish the subtleties of the crystallite portion of RCP media we indentify the crystallites by size and present them in histogram form via the crystallite size distribution. As can be seen with our figure 3.4, the number of spheres in a nano-crystallite is an ambiguous characterization and fails to capture the full composition of individual crystallites. A crystallite of a certain number of circles can be made up of a

variety of combinations of small and large spheres. To remedy this, the nano-crystallite size was identified by an effective radius. The effective radius is determined by finding the total area of the crystallite by adding the area of each circle that makes up that crystallite. In general, the effective radius can then be found using the equation

$$r_{effective} = \sqrt{N_{large}\pi {r_{large}}^2 + N_{small}\pi {r_{small}}^2} \tag{3.2}$$

Initial experimental results showed a strong composition dependence on both the degree of crystallinity and the crystallite size distribution. The results are shown in figure 3.5. To further explore the structure and to establish the initial room temperature boundary condition for our disordered binary alloy we explored this structure further. Taking photos and analyzing them is very time consuming and small sample sizes were necessary in order to get results over different composition conditions. The study was successful for providing a preliminary basis of the RCP structure at various compositions, though further analysis was required.

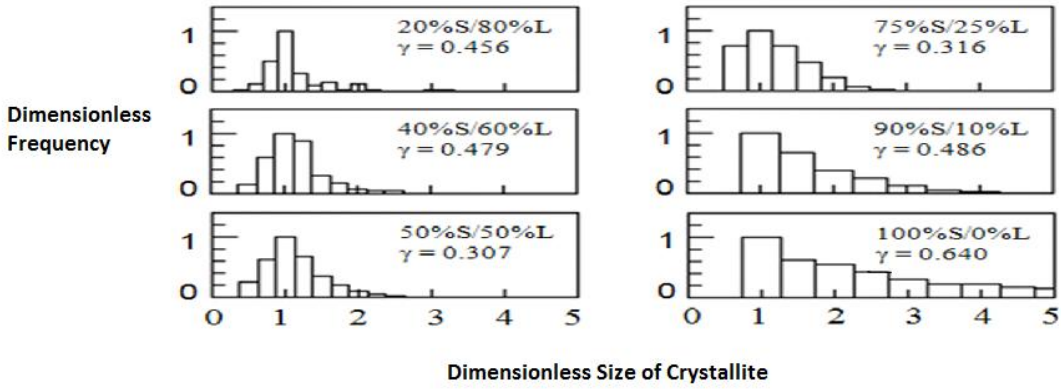

Figure 3.5-Experimental binary 2-D RCP crystallite size distributions for six binary concentrations. Degree of crystallinity γ shown for each distribution.

3.3 Two Dimensional Monodisperse Random Close Packing Simulation

For further analysis and a more generalized model of the RCP structure, we developed a Monte Carlo simulation of a RCP medium. To start, we began with a simulation focusing on a monodisperse RCP structure. This RCP structure model is composed of a mixture of nano-crystallites and disordered glassy matter. The Monte Carlo simulation was developed to replicate experimental results. Control over the mixture of the two phases allowed us to train the simulation to match what was measured. The control parameter for this simulation matches the degree of crystallinity to experimental results. To start the simulation we create a starting nano-crystallite of three circles. This crystallite is located in the middle of the total area and will be used as a seed for the structure to grow.

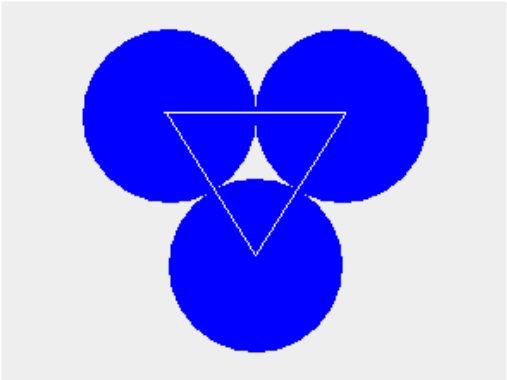

Figure 3.6-Example of minimum crystallite that acts as a seed for the 2-D RCP building algorithm.

The program begins by identifying locations for a circle that can be placed on the outer surface of the seed crystallite that will be in contact with one of the circles of the initial crystallite. The program will replicate the random close packing of beads by building off of this initial crystallite in a semi-random way. If left to build at random the structure would be more akin to glass because of the pure disorder. To replicate a structure of nano-crystallites and glassy matter our simulation needs to have order that we will control to produce a structure with a certain degree of crystallinity. The set of contact points found by the program on the surface of the cluster form a contour. To make this identification of points as computationally inexpensive as possible each circle center is visited and a shell with a radius that is twice that of the circles is superimposed.

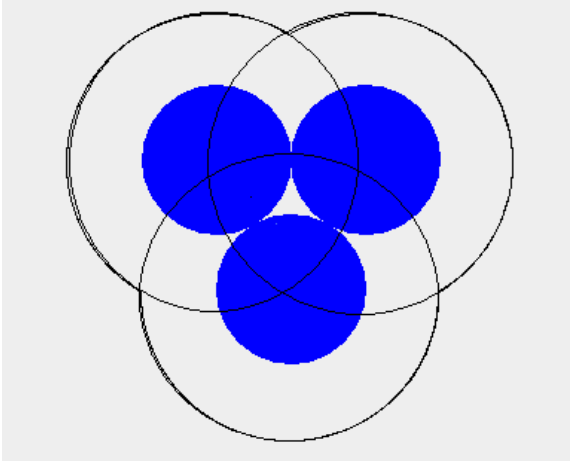

Figure 3.7 Example of shells being drawn around initial seed crystallite which will be used to form the contour of points where the next circle can be added to the cluster

The portions of these shells that are less than a diameter from any of the centers of the other circles in the cluster are removed from the contour, since a circle placed here would overlap one of the already present circles. Any points that match these criteria will be kept as possible points that a new circle can be placed. We also want to find points that will result in an extended crystallite. These points will have the centers of two of the circles exactly one diameter away and will be referred to as bindpoints. Bindpoints are points that will cause a crystallite to be formed or extended. This characterization will be used to control the semi-random formation of the RCP medium. Points matching this specification will be kept separately which will give the program a parameter that can control the degree of crystallinity. This will be done by systematically adding crystallites to the structure but also adding them at random. Any other point on the contour is kept as a potential point where a circle

can be placed randomly on the outside of the seed crystal. Non bindpoints are places on the contour which glassy matter can be formed in the RCP structure.

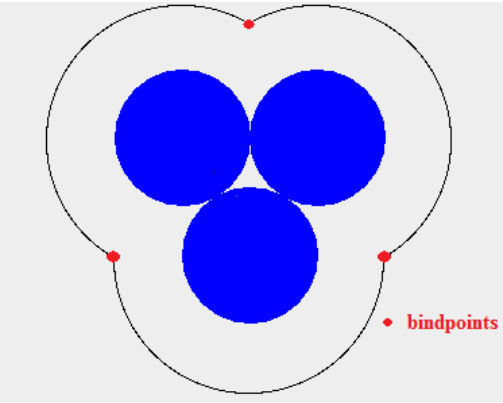

Figure 3.8- Contour used for addition of next circle in 2-D RCP Building algorithm. Red points signify bindpoints which keep track of specific points used to add crystallite points to the structure.

With these two sets of points the program has a control parameter when building the RCP structure. A random number generator is used to choose if a circle is placed randomly on the surface or if the circle will bind to two of the existing circles and expand the crystallite. If the random number is higher than our probability threshold for binding, a circle is randomly placed on one of the surface contour points. If the number falls below the probability threshold, the circle is placed on one of the aforementioned bindpoints. The probability can then be adjusted so that the probability for the circle to be added to a crystallite is controlled. This probability controls the degree of crystallinity of the RCP structure which allows us to match the experimental results.

With the new circle added to the cluster the program redefines the contour to account for new points where circles can be added. The program first checks the previous contour and only keeps points that are a distance greater than a diameter away from the newly added circle to account for overlap with the newly added circle. A shell is then superimposed unto the new circle center to add any new contact points to the contour. This can be done repeatedly as new circles are added to the structure. The simple algorithm described will produce a cluster that is randomly formed; it will also give control over crystallite formation. The problem is that the cluster has large defects that do not agree with the defined randomly closed packed structure. The packing fraction, or the amount of area occupied by circles in a 2-D RCP medium is not satisfied by this method. Packing fraction can be tested using the formula

$$\rho = \frac{N * A}{w * h} \tag{3.3}$$

Where ρ is the packing fraction, N is the number of circles in the area filled with the RCP structure, A is the area of one of the circles, and w and h are the width and height of the area filled by the cluster respectively. With the simple algorithm proposed the packing fraction falls well short of the .82-.89 that is predicted for two dimensional random close packing [47].

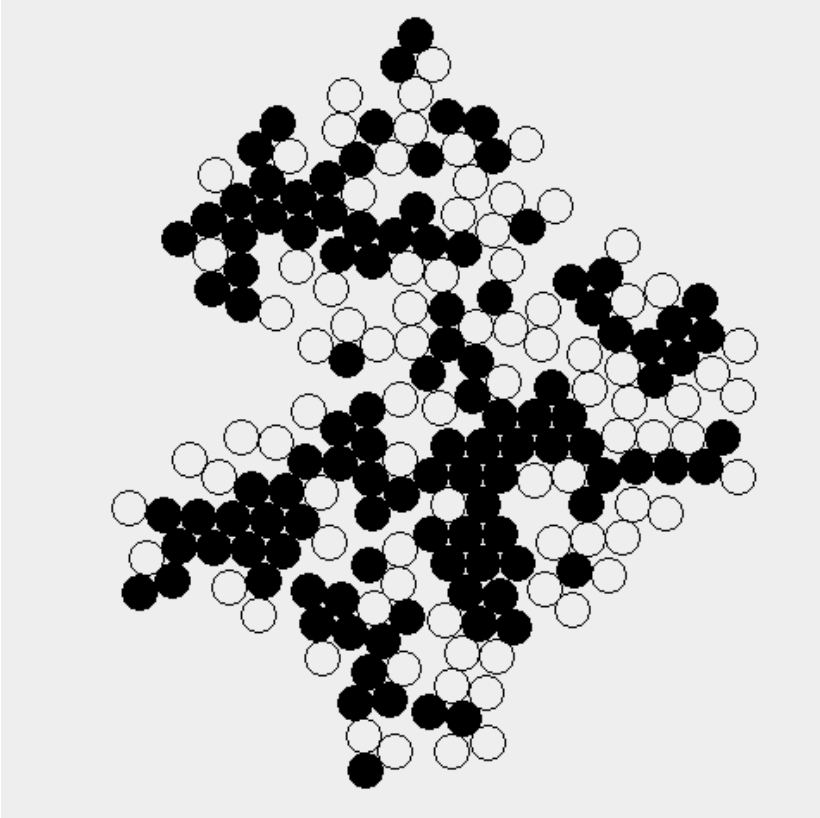

Figure 3.9 Example of 2-D RCP structure built with basic building algorithm with one control parameter.

As can be seen in figure 3.9, large nonphysical defects are made that would not exist in a RCP medium. The black circles represent the bound circles while the white circles represent the randomly placed circles corresponding to glassy matter. In order to correctly simulate a RCP medium the simulation will have to prevent the formation of the large voids seen in the figure.

3.4 Defect Detection

The large non-physical defects in the RCP structure are not acceptable as the packing fraction value is considerably lower than the accepted packing fraction value

for a RCP medium. The defects must be addressed before the simulation can accurately be used to replicate a RCP structure. In our simulation, the problem was solved by preventing the defects from ever forming. A defect is formed when a circle is placed as glassy matter and its center is between one and two diameters away from another circle's center that is already part of the structure.

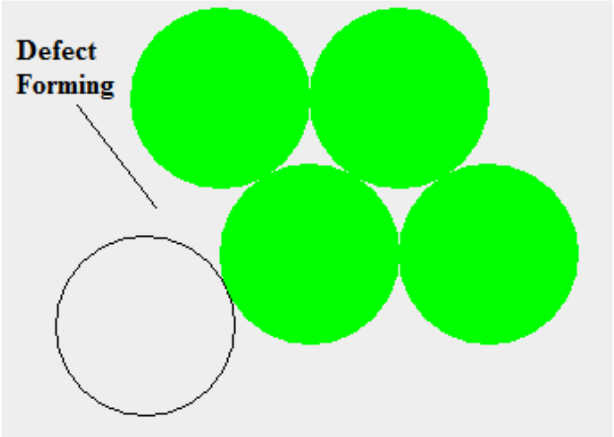

Figure 3.10 Example of defect formation in 2-D RCP structure algorithm.

This defect is caused by the small space created by the new circle, if this void is not addressed it can potentially grow and form the non physical voids in the structure that cause the packing fraction discrepancy in our simulation. To prevent this defect from becoming any larger, the program places a circle on the other side of the defect in order to prevent large voids in the structure from ever forming. This defect detection will prevent non-physical voids while also keeping the packing fraction in the accepted values of a RCP medium.

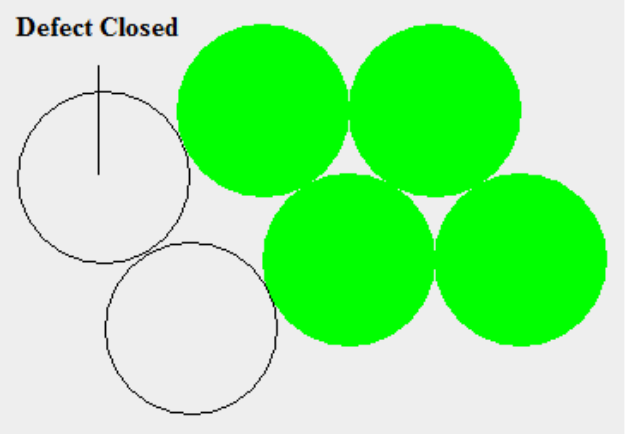

Figure 3.11 Example of the role of defect detection in the 2-D RCP building algorithm. A circle is places to prevent non-physical defects from forming in the structure

With this defect prevention in the program the cluster now has a packing fraction within the accepted range for 2-D RCP medium. With the simulation producing random iterations of RCP structure that have values that agree with theory, the simulation can be run multiple times and the degree of crystallinity and crystallite size distribution can be analyzed over a large sample size. The bindpoints provide a control over the software which is used to match the degree of crystallinity measured via experiment.

3.5 Crystal identification

To characterize RCP we use a combination of the degree of crystallinity and the crystallite size distribution. The degree of crystallinity is an important tool in the classification of the structure and is established by the frequency of using bindpoints in the building of the RCP structure in our simulation. Once the structure is built it is

necessary to measure the crystallite size distribution. The program accomplishes this by visiting each circle center and finding all nearest neighbors, if the centers of three nearest neighbors form an equilateral triangle then they are part of a crystallite. The crystallite is then analyzed to find any adjoining circles that extend that crystallite. Once all the circles in the crystal are found, the program stores the crystallite according to its size and then searches for the next crystallite. After all the crystallites are found the contribution to the crystallite size distribution for that structure is recorded. Below is a figure expressing the results of the crystal identification by displaying each crystallite size as a certain color corresponding to their size, or the number of circles in the nano-crystallite.

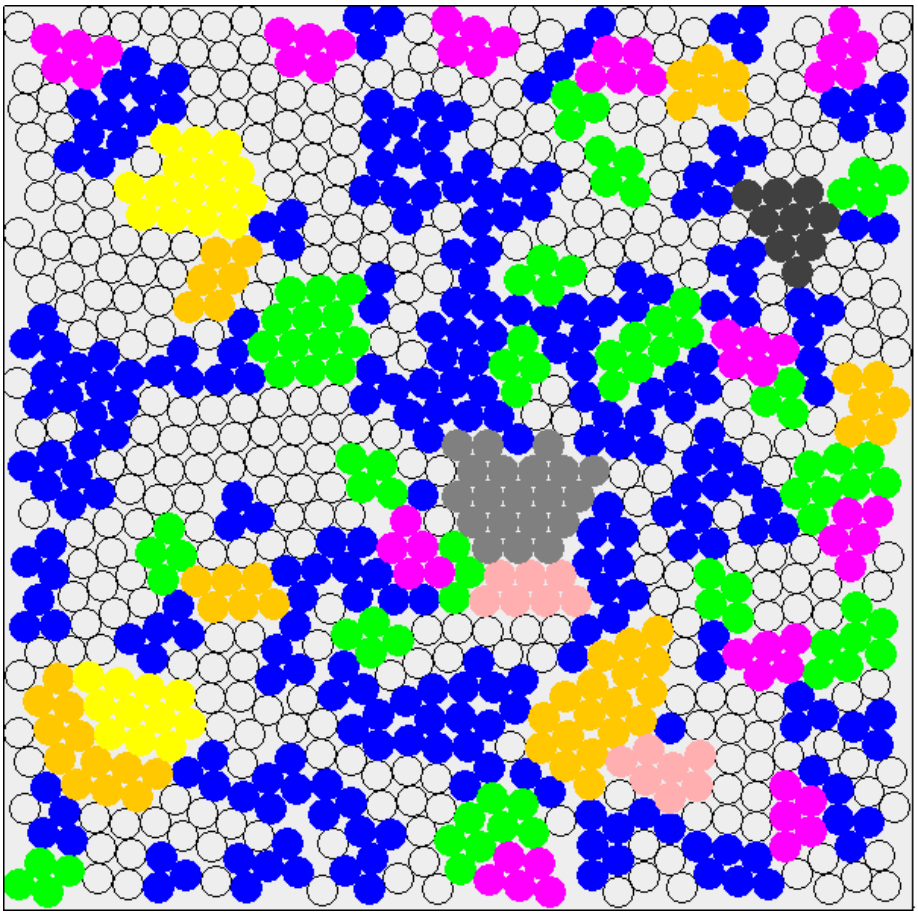

Figure 3.12-Monodisperse RCP structure built with defect detection. Crystallites are identified by size and signified by filled colored circles.

3.6 Two Dimensional Binary Random Close Packing Simulation

We have established an algorithm for assembling monodisperse hard spheres in a randomly close packed structure in two dimensions. Our interest lies in disordered binary alloys made of multiple atom sizes, so to simulate this, our RCP structure needs to be able to handle multiple circle sizes. To accomplish this, we reconfigure the algorithm to deal with multiple circle sizes. The two different particle

sizes add a new parameter for the simulation. With information gained from our experimental work we can examine how the statistics differ with different binary concentrations. The program can also be analyzed with different ratios of circle size. With two different particle sizes, the initial seed for the cluster must be reconfigured. There are now four different possibilities for the initial seed in two dimensions as highlighted in figure 3.2. To decide whether a large circle or a small circle is chosen, the program uses a random number generator and a probability threshold determined by the goal concentration of each circle size. This technique is similar to the one that is used in determining binding probability in the simulation. With different seed crystallites the surface contour will be different depending on the initial seed crystallite. The program keeps track of all the locations on the surface where both a small circle and a large circle can be placed. This results in two surface contours created with two sets of bindpoints for each circle size. The contours are created with the same shell approach used in the monodisperse algorithm, though since there are three possible contacts three different shells have to be used to create the contours. The three different contact types are two small circles in contact, two large circles in contact, and a small circle in contact with a large circle.

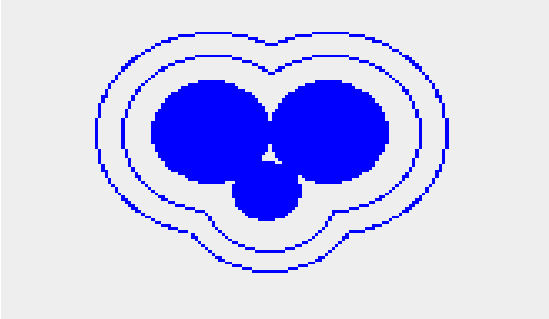

Figure 3.13-Example of the two contours needed when building a binary RCP structure.

The rest of the program runs as previously described for the monodisperse case. Each circle added to the structure has a size chosen randomly weighted by the goal composition of the binary structure. After a new circle is added two surface contour plots must be updated to keep track of potential places for the next circle to be added at both sizes. Defect detection is used to prevent non-physical voids in the structure, though the plugging of the voids is done with a circle with the size selected at random. This technique produces results that correspond to the binary RCP system in terms of packing fraction. The crystallite identification changes slightly in a binary system, instead of an equilateral triangle being the basis of a crystallite in our monodisperse system, a crystallite can be defined in the four ways displayed in figure 3.2. The minimum basis for any crystallite is now three neighboring circles forming an equilateral or isosceles triangle. The identification is still done by identifying these crystallites and categorizing them by size. The result of the 2-D binary RCP simulation can be seen below.

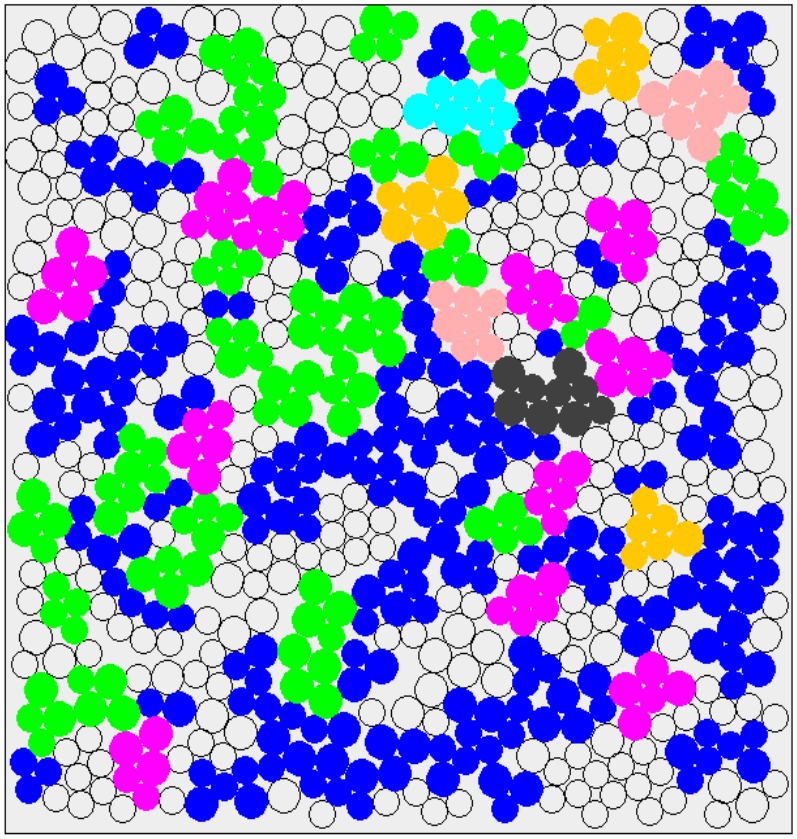

Figure 3.14- Binary RCP structure with crystallites identified by size and signified by filled colored circles.

The crystallite size distributions experimentally measured are replicated using the parameter that assigns added circles to bindpoints. Crystallite size is expressed by an effective radius to remove ambiguity in the crystallite identification by number of circles. A crystallite of a certain number of circles can be made up of a variety of combinations of small and large circles. The effective radius is determined by finding the total area of the crystallite by adding the area of each circle that makes up the crystallite. The radius is then found by taking that area and finding an effective radius that is the radius for a circle with that area as expressed in equation 3.2. We use the

structural information gathered experimentally to choose the parameters used at different binary concentrations. The degree of crystallinity and crystallite size distribution from the experimental data were matched with this Monte Carlo Simulation.

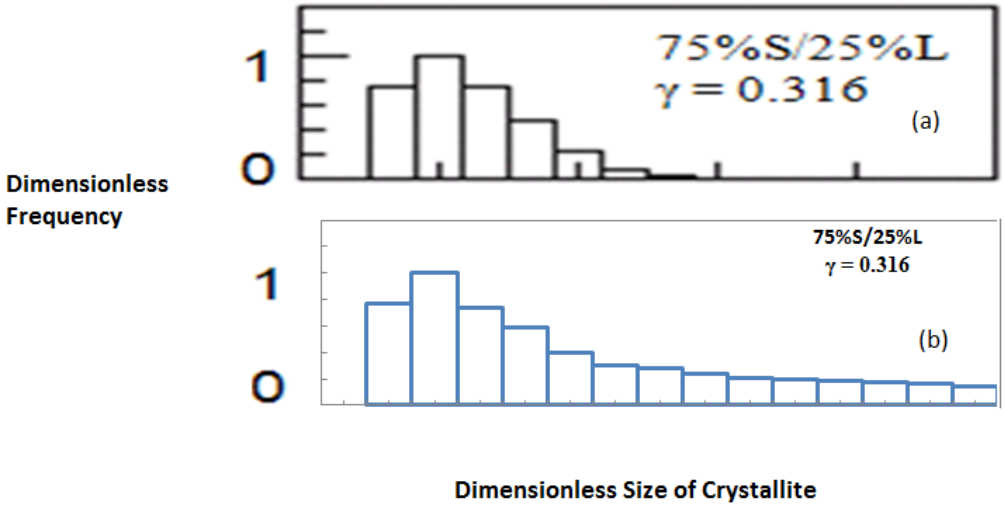

Figure 3.15- Comparison of crystallite size distributions from (a) experimental 2-D RCP data and (b) trained 2-D RCP building algorithm simulation.

With our Monte Carlo simulation trained to replicate experimental RCP data, we have a tool for generating the RCP structure that will be used in modeling the structure of a disordered binary metallic alloy. For a disordered metallic alloy, the simulation can be tuned based on the atom sizes in the alloy as well as the atomic composition of the alloy to generate its RCP structure. This will be an important step in monitoring the morphology of the disordered alloy as it provides an initial condition for the alloy.

Chapter 4

Mechanical Oven Experimental

4.1 Experimental Strategy

After characterizing RCP in two dimensions, our next step towards the eventual goal of understanding the morphology of disordered binary alloys was to investigate the RCP structures' reaction to temperature change. Our investigation aimed to explore how the distribution of nano-crystallites in a RCP medium evolves at elevated temperatures by the mechanism of thermal forcing. The initial RCP structure of a disordered alloy was found to depend sensitively on alloy composition in our work described in chapter 3. The nano-crystallite size distribution has been obtained for a number of compositions under the stationary condition. To simulate heating, the 2-D cell on a horizontal plane, containing an RCP assembly of binary spheres, has been instrumented for time-dependent actuation by two stepping motors in two mutually orthogonal directions; each motor is driven independently according to a chaotic algorithm.

We have demonstrated that the control programs for driving the 2-D RCP assembly can be fine-tuned to produce a robust Gaussian velocity distribution for the individual spheres. The distribution function meets the scaling requirement between the distributions of the x- and y-component for like particles and between the distributions of the velocities of unlike particles. The width of the velocity distribution, i.e., the measures of medium temperature, has been shown to be

responsive to the amplitude of mechanical forcing by the stepping motors. In other words, the temperature of the 2-D assembly scales essentially linearly with the mechanical amplitude, and as a result, the temperature of the driven RCP bed of spheres has been raised from T*, the lowest temperature, to 2T*, 4T* and 8T* in linear proportion to the drive amplitude of the stepping motors.

4.2 Experimental Apparatus

The apparatus used to simulate our disordered binary alloy can be seen in Figure 4.1. The arrangement of spheres rest on a piece of glass surrounded and held in place by a steel frame. The glass is tempered to prevent the glass becoming a charged surface after long periods of exposure to the moving metallic spheres. This steel frame is attached to the stepper motor arrangement that is used to drive the system at the various temperature settings. The boundary of the 2-D bed of spheres is provided by a fixed boundary that is separated from the base plate so that it remains stationary. The data is taken by a Fujifilm S2000 digital camera, which is kept above the 2D bed and is held by a base with precision position controls that can be used to finely tune the alignment of the camera image axes with the axes of motion for the 2-D bed. To illuminate the 2-D bed of spheres, light is reflected off a thick piece of reflective white paper tilted at a shallow angle. Light is provided by a lamp not shown in the schematic diagram; the lamp is fixed with a frosted transparent piece of paper fixed in front of it to produce homogenous illumination reflected off the white paper. To minimize vibrations, the moving pieces of the apparatus are supported separately from the main lab table of the apparatus. This includes the base plate and stepper motors.

The beads used in the experiment are steel ball bearings. To facilitate our simulation of a binary alloy we used two sizes of ball bearing with radii of 2.488±0.099 mm and 3.193±0.033 mm, and a mass of 0.0641g and 0.104g respectively.

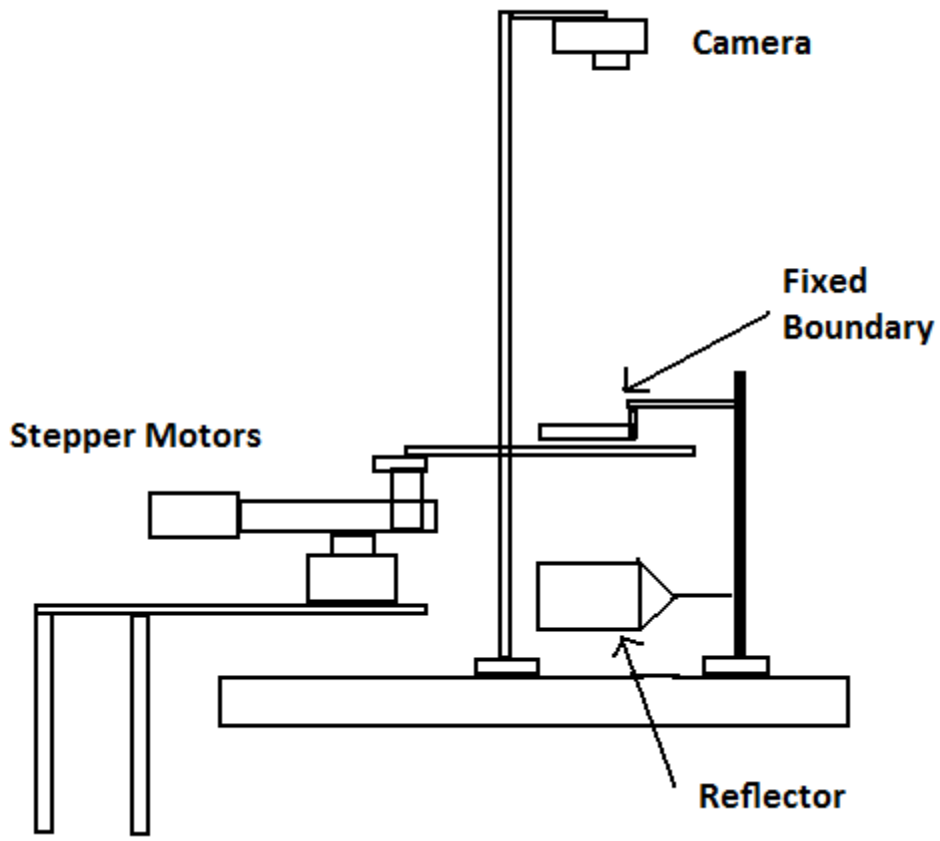

Figure 4.1-Schematic diagram of "mechanical oven" experimental apparatus. Two orthogonal stepper motors drive the transparent base plate due to a chaotic algorithm used to simulating effective temperatures. A fixed boundary kept separate from the moving portions of the experiment keep the hard spheres contained. The baseplate is illuminated off a reflector by a diffuse light source (not shown). Data are taken using a ten megapixel camera using a burst setting.

4.3 Driving the System

The bed of spheres is driven by two single axis stepper motors that operate in orthogonal directions to each other creating a 2-D driving system. A stepper motor is run by rotating a leadscrew which drives the base in the desired direction. The movement of the base can be split into microsteps that break the rotation of the leadscrew into small partial rotations. For the stepper motors used in this experiment we use a 2mm leadscrew that can split a rotation into 256 microsteps. This gives us a movement resolution of 0.04 µm per microstep. The stepper motors have a maximum velocity of 40mm/sec giving more than enough movement speed for our desired displacements.

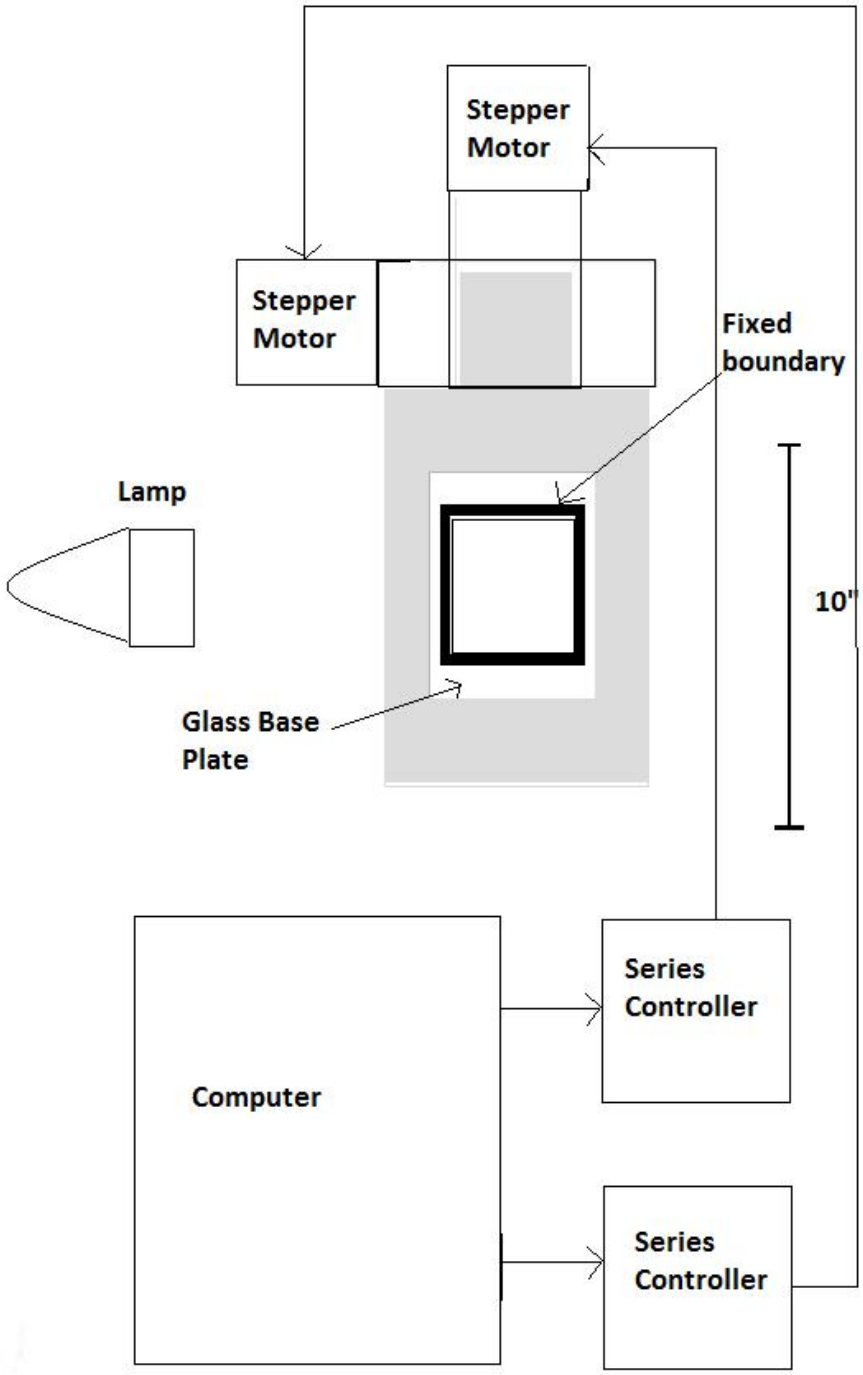
Stepper Motor
Stepper Motor
Fixed boundary
Lamp
10"
Glass Base Plate
Computer
Series Controller
Series Controller

Figure 4.2- Top view schematic of the mechanical oven experiment. The stepper motors are controlled by two separate series controllers with the driving routines uploaded from a computer.

Figure 4.2 shows a schematic of the driving system. Two Single Axis controllers are fed a pink noise chaotic driving routine from a computer. The controllers then drive the stepper motors in relation to the driving routine. The controllers operate using Intelligent Motion Systems (IMS) software designed specifically for controlling the stepper motors used. Our driving routine is designed to simulate temperature in a hard sphere system. After experimentation, it was observed that this could be accomplished by cyclically driving the motors in a pink noise chaotic fashion. The two motors are offset so they don't provide identical motion. Parameters are set at the beginning of the routine to determine the conditions of the stepper motors' movements. The first parameter is the motor resolution select variable which sets the amount of steps per revolution. The maximum steps per revolution setting is 256 and the minimum is 2. Other values come in binary increments from the minimum to maximum motion per step. The second parameter is the motor unit variable, which sets the amount of microsteps per user variable. This sets the unit of length for the motion, and needs to correlate with the steps per revolution for the program to operate correctly.

The routine used to drive the system accesses a stored list of random numbers to create the oscillations. The stepper motor cycles through the random displacements, the two motors are offset to prevent synchronization of the movements.

These displacements are determined by multiplying these stored random numbers by a maximum displacement. The initial parameters can create four different operating temperatures for the stepper motors. These operating temperatures correspond to 256, 128, 64, and 32 steps per revolution settings. The maximum displacement variable can be incremented to reach temperatures in between these four base temperatures, though for this study we looked at the discrete temperature steps associated with the binary settings of the stepper motors. To run the program, the routine is downloaded from the computer to the controllers and then a go command starts the motion routine and will continue until the program is stopped manually. These commands are fed through a terminal on the computer which is part of the IMS system. Each controller is operated separately for independent control of the two directions.

4.4 Measuring the Angle of Tilt

One of the major physical parameters for our experiment is the angle of tilt of the baseplate. The tilt of the baseplate determines the amount of packing in the system, as well as determining the amount of gravitational acceleration that will be incident to one of the directions of motion. Figure 4.3 shows a schematic ray diagram for measuring this angle. A laser diode emits light that is fed through a beam splitter. The light reflects off the base plate, and also reflects off of a water surface that is kept below the base plate. The light is then reflected off the beam splitter and measured to see the difference of reflected angle between the two surfaces. The beam reflected from the base plate is equal to two times the angle of tilt with respect to a level surface represented by the water.

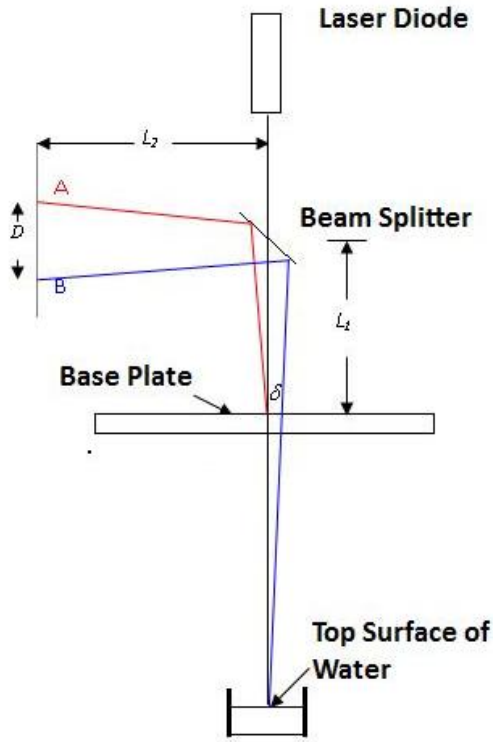

Figure 4.3- Schematic ray diagram for measuring the angle of tilt. Two light rays are reflected off the base plate and the top surface of water which is level and compared to measure the tilt in the base plate with respect to the surface of the water.

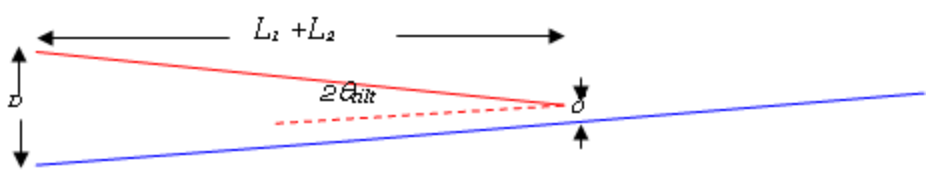

Figure 4.4 - Equivalent ray diagram for measuring the angle of tilt.

The equivalent ray diagram can be seen in figure 4.4. After measuring the appropriate distances the angle of tilt can be measured using the formula

$$\tan(2\theta_{tilt}) = \frac{D - \delta}{L_1 + L_2} \tag{4.1}$$

The water surface reflects a beam that is coincident with the beam reflected from the base plate. If that is not the case, it is necessary to add the value δ. The distance D can have both vertical and horizontal components for the two degrees of freedom for the base plate. After measurement, it was determined that the angle of tilt for the data presented in the y direction was $\theta_y = 0.855°$ and in the x direction it was $\theta_x = 0.418°$. The effect of the tilt in the x direction can be seen by the free boundary of the bed of spheres not being orthogonal with the y-direction.

4.5 Illuminating the Bed of Spheres

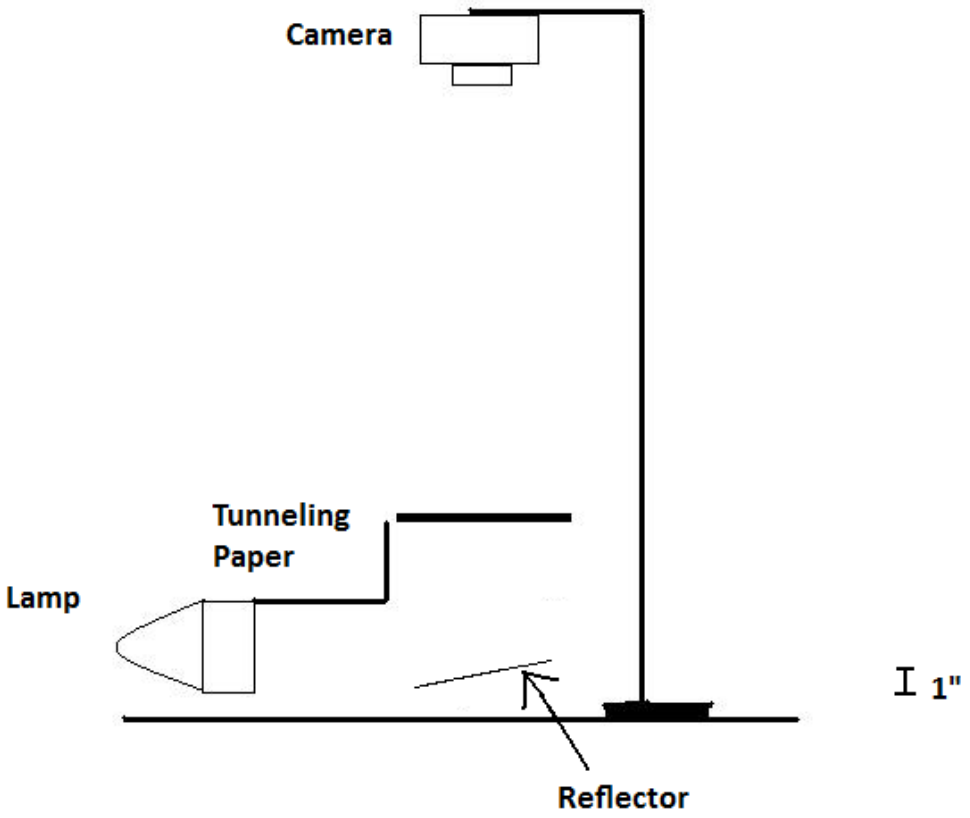

Figure 4.5 - Schematic diagram of the illumination of the bed for imaging. The lamp provides a diffuse light source that is reflected at a shallow angle to provide illumination from underneath the baseplate. Tunneling paper refers to paper used to prevent non reflected light from directly affecting the imaging.

The image bursts are taken with a Fujifilm S2000 digital camera. The camera is set to its Ultra High Speed burst function which captures 33 images at 13.5 frames per second at a resolution of 3 megapixels. The camera is zoomed into its super macro setting which provides a consistent zoom setting throughout a large quantity of bursts.

The camera is mounted on two translational stages that give fine alignment control for capturing the bed of spheres in the camera's field of view.

The bed of beads is illuminated by a lamp that has its illumination intensity controlled by a variac generator. The variac generator is necessary in order to control the illumination of the bed of spheres with a precision that gives a desired contrast between the beads and the background. The light from the lamp is funneled to a thick white piece of paper that serves as a reflector to give an even background for the bed of beads as seen in figure 4.5. To get an even distribution of light to the reflector we do not use a point light source. The lamp's light is fed through frosted paper to diffuse the light and create an even light intensity across the reflector. The light reflector is set at a shallow angle to provide the best even illumination of the bed. The funneling of the light is used to minimize the ambient light that can affect the accuracy of the images. The edges of the circles become non circular due to the direct light from the lamp if it is not funneled as seen in figure 4.6.

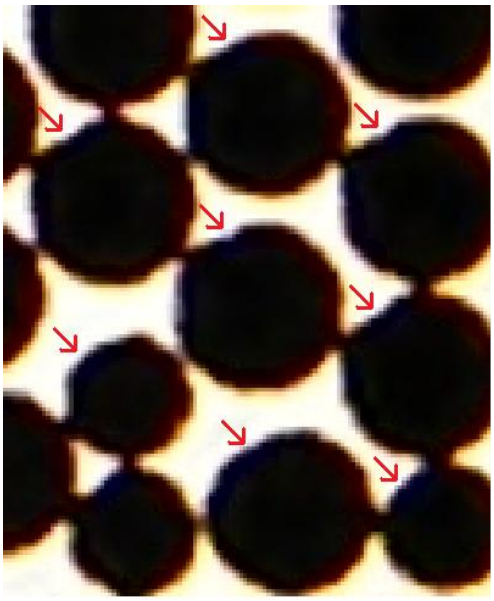

Figure 4.6- Example of ambient light causing noncircular defects in the images. This is prevented by careful illumination highlighted in figure 4.5.

The camera has a minimum shutter speed of 1 ms, so the exposure has to be controlled with the illuminating light. The variac generator is set at a low intensity so that the camera is not over exposed. An example of the effect of the lamp intensity can be seen in figure 4.7. Digital cameras take images via light sensors that operate by converting light energy into electrical energy. If the shutter speed is too high there will be light saturation which will cause much of the image to have a maximum brightness because the sensors were exposed to the illuminating light for too long. The shutter speed for the cameras burst setting is fixed, so it is necessary to use the incident light intensity to control the amount of light on the sensors for the shutter speed time period.

The exposure of the camera is very important in insuring that the image will provide accurate data representing the structure of the beads. If the image is over exposed, the diameter of the spheres can be incorrectly represented. Ideally, the largest circular cross section of the sphere will be represented in the image. If there is too much light being fed to the camera, reflections from the spheres will shrink the circular cross section which will create problems during the analysis of the image. This effect can be seen in figure 4.7. One of the factors we are most interested in studying in these images is the structure of the bed of spheres during movement. To analyze the structure, it is necessary to know whether the spheres are in contact; this means that the diameter has to be accurate so that it can be determined whether the edges of spheres are touching. In figure 4.7 it is clear that the overexposed image will not facilitate any contact between the spheres because the cross sections of the spheres are being misrepresented. In the right image, it can be clearly seen where spheres are in contact at the edges of the cross sections, making accurate analysis possible.

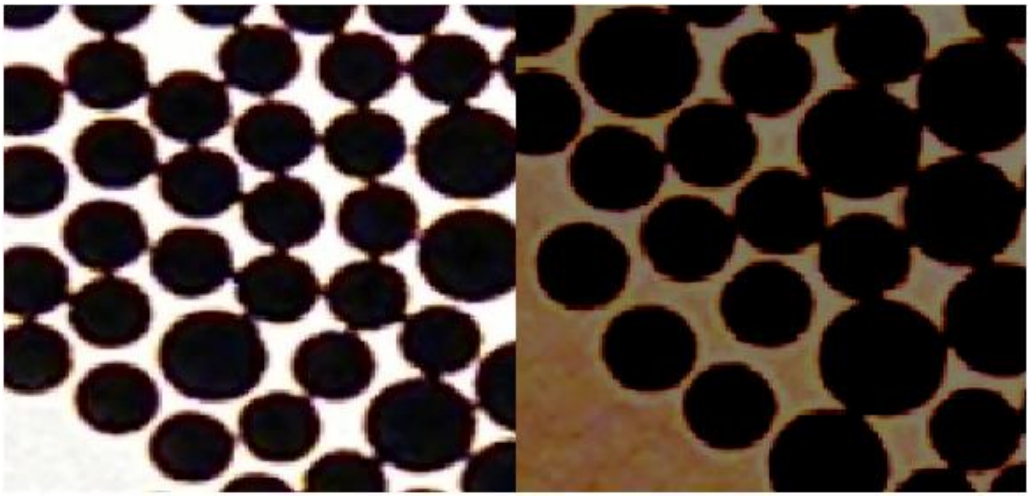

Figure 4.7- 2 figures taken at different illumination intensities highlighting the difference in circle radius seen when light saturation affects the imaging.

4.6 Effect of the Baseplate

The baseplate is a piece of tempered glass held by a steel frame. It provides the surface for the steel ball bearings to travel. Glass has the added benefit of being clear so that the bed of spheres can be illuminated for imaging. The motion we are trying to simulate is free motion interrupted by collisions, both between spheres and with the boundaries. The base plate provides friction so that the particles can move freely in relation to each other without sliding as one unit. With a clean glass surface this is possible; problems arise when dust is collected on the glass surface. The beads move as a group if dust causes a reduction in friction to the point where beads can slide together. Regular cleaning of the glass surface is needed to ensure consistent free movement of the spheres in relation to each other.

Chapter 5

Measurement of Experimental Data

5.1 Images Produced From the Mechanical Oven Experiment

Figure 5.1 shows an example of the image data produced by our imaging technique described in chapter 4. The image is 2048x1536 pixels, though only a portion of the image is our fixed boundary data field. Each pixel represents 0.16mm in length for our zoom setting. Our data comes in bursts of these images, which contains 33 sequential images. Our measurement strategy is to analyze the RCP structure of the spheres for each image and to track the movement of the spheres inside the fixed boundary over a pair of images. Typically, many bursts of images are taken in order to produce a sufficient sample size for each movement speed. After taking our data, we will need to be able to sufficiently analyze a large number of images.

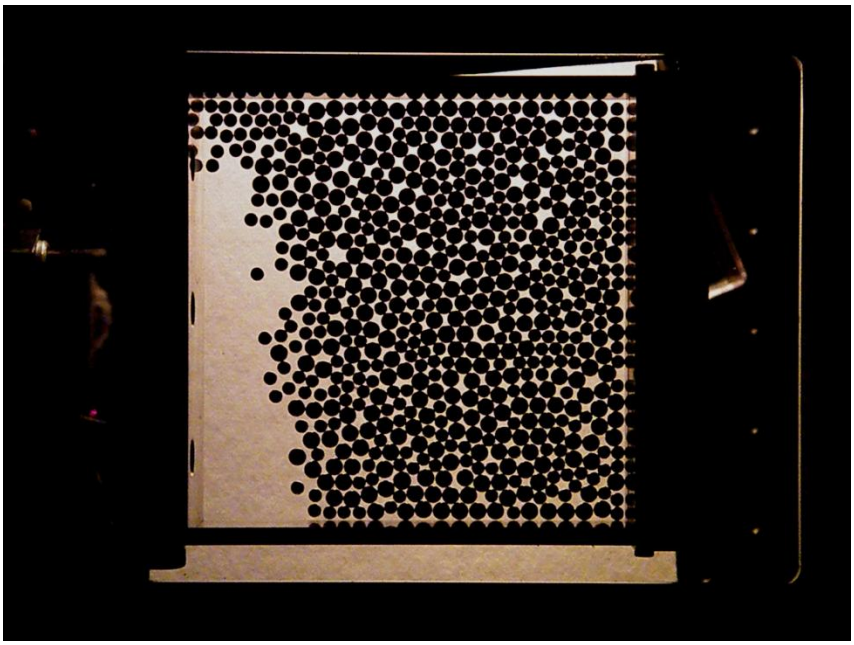

Figure 5.1-Example of original image from 33 image burst taken with the apparatus .

When dealing with large amounts of data, computational efficiency becomes paramount for analyzing data in a reasonable time. We had to successfully develop techniques for preparing the images for analysis, analyzing the images to obtain data, and evaluating the data for analysis. All of our techniques have to be capable of operating with large amounts of information in a reasonable time. Our developed technique also must withstand careful inspection to ensure the accuracy of the analysis for the captured data.

5.2 Pre-Processing the Imaging Data

Before the image is analyzed, a certain amount of preprocessing is required to transform the image in a more computationally digestible form for analysis. The first

step in the preprocessing is to crop the image field so that only the portion of the image inside the fixed boundary is present. This removes all unnecessary portions of the image from the original. The image is also checked to see if the boundary corresponds to the horizontal and vertical axis of the picture. If this is not the case, the picture is rotated. The initial image is a 12MB rgb color image, for our purposes the image color does not provide any of the information we are interested in. The analysis only needs to differentiate between circles and background. After cropping the image, it is converted into a binary image. A binary image is an image where the pixel value can either be a one or a zero providing the information we need for the analysis in the simplest form possible. An rgb image consists of three channels for each pixel, these channels are the red, green and blue channels. Each channel contains a number between 0 and 255 which corresponds to the intensity of each color. Brightness transcends the color channels though, and the contrast between the circles and background is present in all three channels. To convert each of these complex pixels to a value of either one or zero the three channels of the rgb image are averaged to one value. Once each pixel has an average intensity value, the values are subjected to a threshold where every value above the threshold becomes a one and every value below the threshold becomes a zero. The threshold is chosen based on the values present after the channel merger, but can be fine tuned to adjust where the edge of each circle appears since that is where the channel intensity will drastically change.

To find the circle centers our program relies on the edges of the circles, so our image is run through an edge detection program. All image analysis is provided by the

ImageJ software library. ImageJ is open source image processing and analysis for the java programming language. The edge detection will convert the solid circles into circle edges. For an image, edge detection looks for sharp changes in intensity. For a binary image, this corresponds to changes from background zero values to foreground one values. The edge detection keeps a three pixel thick edge around each circle. The design of our analysis program requires calculation at each edge pixel in the image, this means that more edge pixels will correspond to more computation time. The last process performed on the image is to thin the edges, this process is called skeletonizing. Skeletonizing an image creates a topological skeleton for all shapes in the image. A topological skeleton of a shape consists of all points equidistant from two of the shapes boundaries. In the case of our circle edges, this will create a one pixel thick circle edge between the boundaries of the thick edge. The end result of this preprocessing can be seen in figure 5.2, this is an example of the image that is analyzed to find the circle centers.

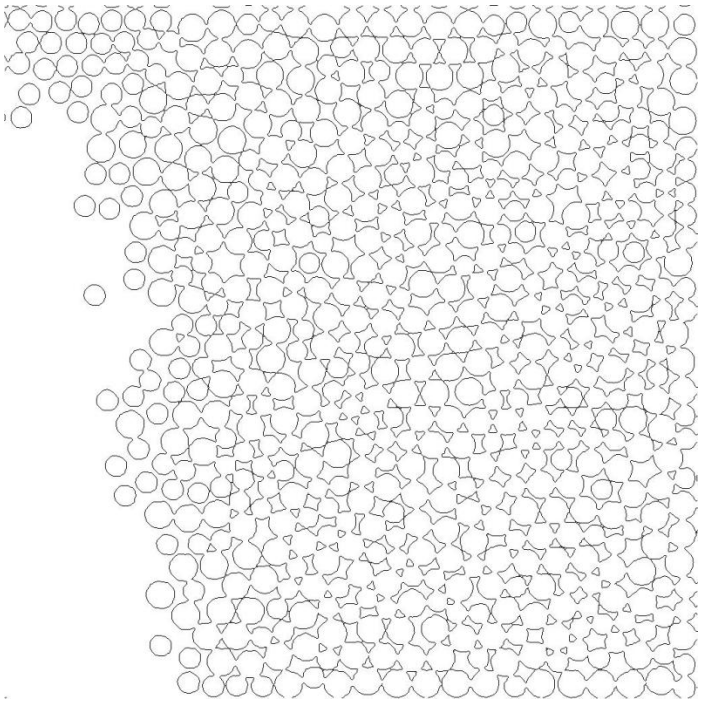

Figure 5.2- Example of image after preprocessing technique which results in a cropped image of the circle images prepared for the analysis software.

5.3 Identifying circle centers

An analysis program based on a Hough transform is used to find the centers of the circles in the image. Specifically we use the circular Hough transform, as Hough transforms can be used for fitting various functions in an image. The edge point of a circle with a radius r and a center point (a,b) can be represented using the functions

$$x = a + r\cos\theta \tag{5.1}$$

$$y = b + r\sin\theta \tag{5.2}$$

Since we know the radii of our two circles in the image we can search the image field and use the edge points to find the centers. For any edge point of a circle, the center of the circle will lie on some point of a circle of radius r centered at the edge point (x,y). If a circle of radius r is drawn around all the edge points of a circle, the circles will meet at the center of the circle as seen in figure 5.3.

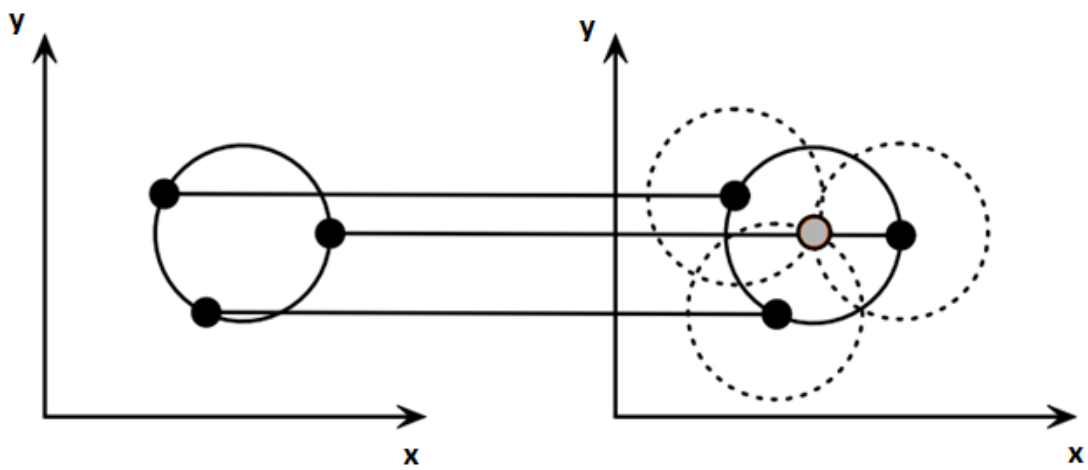

Figure 5.3-Example illustrating how the Hough transform can be used to find the center of a circle using the circles edge points.

The spheres used for our experiment are of two sizes. The Hough transform requires the diameter of the circle to be known in order for detection. For each circle edge pixel in the image, each point one radius away is incremented by one in the Hough transform space. The Hough transform space is an integer array that keeps track of the drawn circles from the Hough transform. Since the center is exactly one

radius away from all the edge pixels for a circle, the center of the circle will have a high integer value in the Hough space once the transform is complete. For an ideal circle edge, this integer value would correspond to the number of edge pixels for the circle. If the radius of the circles is not chosen correctly, the Hough transform space will not have peaks at the circle centers but will instead have volcano like peaks with a small integer value at the circle center.

To begin each burst of images, the image is passed to a subroutine that finds the best diameter for the Hough transform with precision to the tenth decimal place. This is run to account for possible zoom fluctuation from the camera. The subroutine operates by iterating over 10 diameters, since there are two sphere sizes we have to find the best diameter for both of the sphere sizes. To find the ideal diameters, the image is analyzed to find the circle centers that will be monitored over the diameter iterations. The initial diameters are chosen based on the diameters that are most often the ideal diameter for the experimental zoom setting. The subroutine then runs through the 10 nearest diameters to a tenth precision and monitors how the Hough peak sizes change as a function of diameter at the circle center value. When the average Hough peak size is maximized, the ideal diameter is chosen. For the rest of the burst of 33 images, this diameter is used.

After the diameter is chosen, circular array shells are created to be used in the Hough transform. For each diameter, a 360 element array is filled with coordinates for the edge of a circle with the given radius. This is a quick and efficient way to

perform a Hough transform to the image files. Instead of calculating 360 points a distance r away from each edge point, an array element can be called and added to each of those points, which is much more computationally efficient. Creating the Hough space is a simple procedure, the program starts by searching through the image looking for edge points. When an edge point is found, the program calls all 360 elements of the circle shell array. At each element, the Hough space array element at that point is incremented by one. The Hough space array is the same size as the original image, any shell point that falls outside the bounds of the image is disregarded. Because there are two different diameters, a Hough space array has to be made for each diameter. A result of these transforms can be seen in figure 5.4 and 5.5.

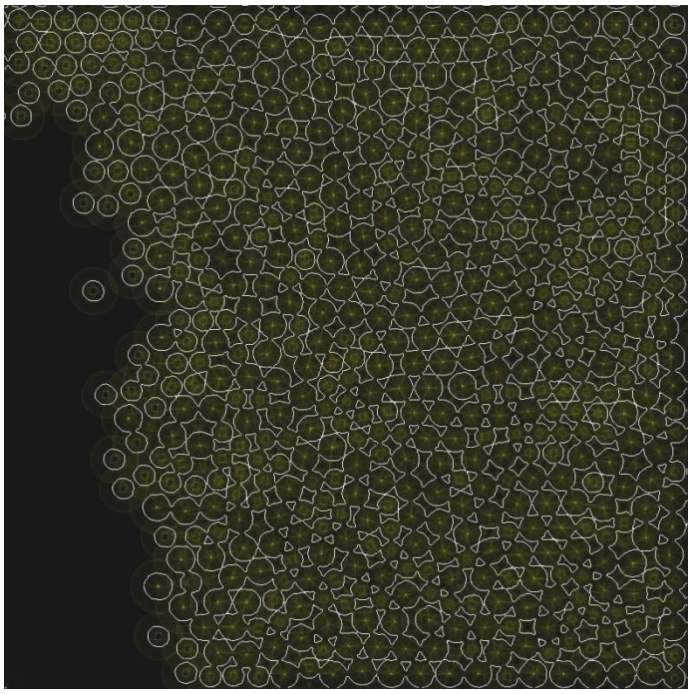

Figure 5.4- Hough transform intensity map for the large diameter with the original edge data superimposed on top. Bright spots at the center of the large circles correspond to circle centers.

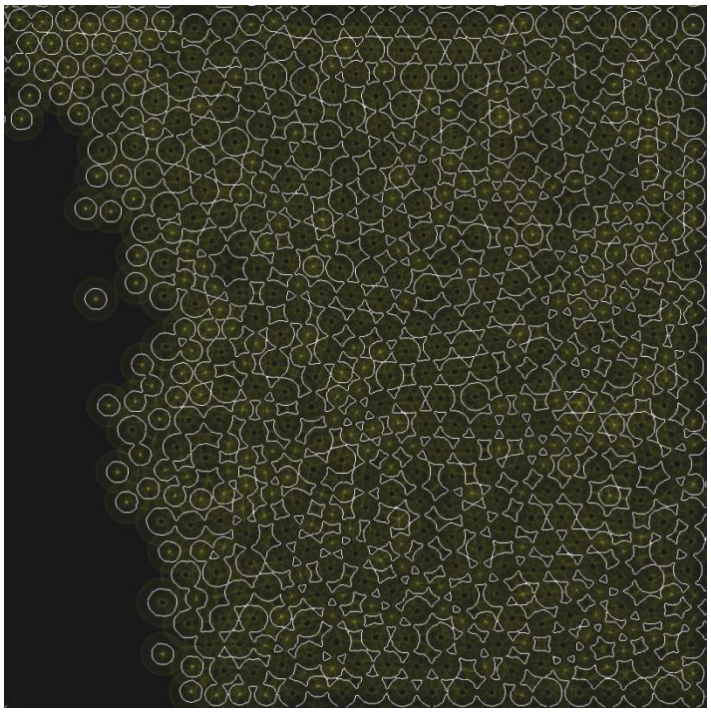

Figure 5.5 Hough transform intensity map for the small diameter with the original edge data superimposed on top. Bright spots at the center of the large circles correspond to circle centers.

After each edge point has been visited by the software, the Hough transform is complete and the circle centers can be found from the Hough space. This is done by sweeping through the Hough space and finding the peaks. To do this, a threshold variable is set for each diameter. When a value in the Hough space array is greater than the threshold, it is saved as a potential center. It is important that the threshold is set such that it is high enough that each peak is found but not so low that noise in the Hough space is falsely identified as a circle center. There is the potential that a given center peak has multiple pixels above the threshold. If this happens, and there are multiple points in a few pixel region above the threshold, they are all saved together

into clusters. After all the peaks are organized into clusters, the clusters are averaged to get the preliminary circle centers.

The original Hough transform is run with integer precision. Our goal is to get center precision to the tenth decimal place. To do this with a single Hough transform, a Hough space array ten times the original image size would be needed. Dealing with an array of this size is too computationally expensive to be practical. Instead of making a large array, we revisit each preliminary circle center pixel and break it into a ten by ten sub- pixel array. For each center point, the program revisits the image edge points around that center pixel. The Hough transform procedure is repeated at these edge points, except that now we are only interested in the center point which has been broken into a ten by ten Hough space array for one circle located at the center pixel. After running through the edge pixels, the ten by ten center point array gives a new higher precision Hough space for the peak of the original center Hough peak. The maximum peak in this higher precision Hough space allows us to add an extra digit of precision to our circle centers.

5.4 Program Structure

Software was written in order to take a large number of images and obtain data relating to the movement of the spheres. The Hough transform technique is used to identify circle centers, but the analysis of the data needs to track the centers over multiple images. Figure 5.7 shows a schematic diagram of the programs operational procedure. The camera used to take the images is run in burst mode. The bursts

contain 33 consecutive images, and often times there will be multiple bursts taken in order to obtain a large sample size for analysis. Therefore to begin the program we iterate over the number of bursts in the sample. Also at the beginning of the program text files are created for keeping the data obtained by the program. At the start of each burst, the subroutine that finds the optimal diameter is run to compensate for possible fluctuations in the zoom of the camera. Once the two diameters are chosen for the burst, the program iterates over the 33 images in each burst. For each image, the centers need to be found for every circle in the image. This is done with the previously discussed Hough transform technique, which is done once for the initial centers, and again for an extra digit of precision.

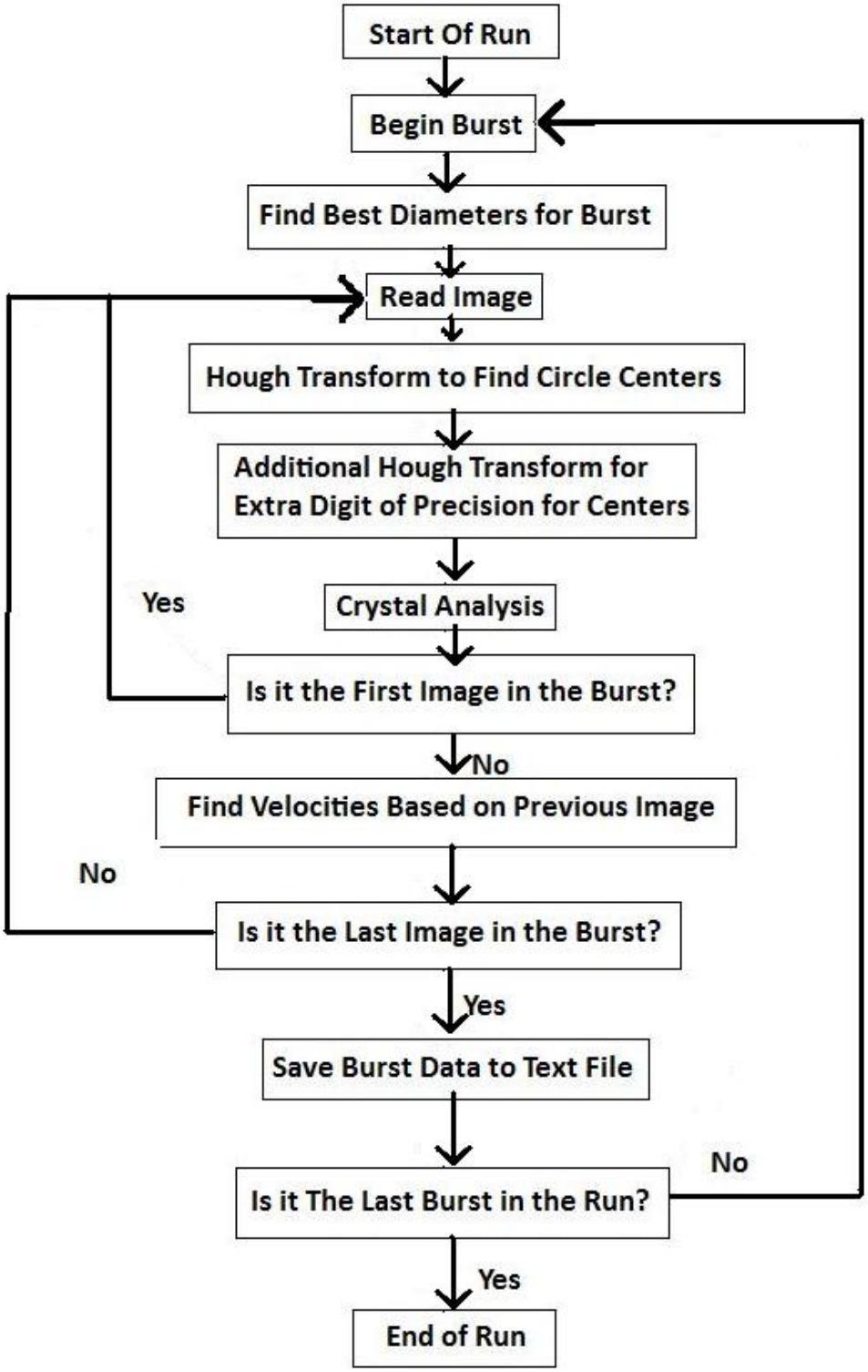

Figure 5.7- Schematic diagram of the programs operational procedure.

After the circle centers are detected with the desired precision, the goals of the analysis are to analyze the structure and measure the movement of the circles. To this point we have kept the two circle sizes entirely separate from each other based on the separate Hough transforms needed to detect the centers. In order to analyze the structure of the bed we have to recombine both circle sizes as one coherent structure as it is in the original image. Before combining the circle centers, the structure is checked for any overlap. After assuring that there is no overlap in the structure, the bed can be analyzed for structure and movement. The combination of the right threshold values and diameters set for the program parameters, as well as good image quality causes overlap to not be present in the combined structure. If the two circle sizes are sufficiently different, which they were for this study, a circle will not be detected at both sizes. In order to characterize the structure of the detected circles the array of circle centers and sizes are passed to a crystal identification subroutine. This subroutine is designed to indentify crystallites in the structure and then to categorize them by size.

A crystallite is a minimum of three circles that are all in mutual contact. The first step in crystal identification is to separate the circles into crystalline circles and non-crystalline or glassy matter circles. To first identify the crystal circles we go through each circle in the bed and check any circles that are nearest neighbors. Both circles are then checked to see if there is a third circle that is touching both of them forming a crystallite. If this condition is satisfied, all three circles are then identified as crystallite circles. If there is no such condition with any of the circles' nearest

neighbors it is identified as a glassy matter circle. Once all the circles are identified as such they are then categorized by size. This is done by going through the crystallite points and grouping all circles that are part of the same crystallite. Circles are then organized based on the crystallite they are in. It is then possible to identify the crystallites by size which can be summarized with a crystallite size distribution. The end result of the analysis can be seen in figure 5.8.

The final piece of information we want to gain from the circle data is the average velocity of the circles from image to image. This is done by comparing the circles from a current image to the circles from the previous image. After finishing center detection on an image, the circle data is saved in an array to be used in the next image in the burst. To find the velocities, each circle's current position is compared to that in the previous frame. The velocity is then found by taking the displacement and dividing it by the time between frames which is a constant given by the burst mode of the camera. We are interested in the velocity data in histogram form, so once a velocity is found the bin corresponding to that velocity is incremented. This velocity data is taken for both circle sizes separately, because the distributions are affected by the mass of the sphere.

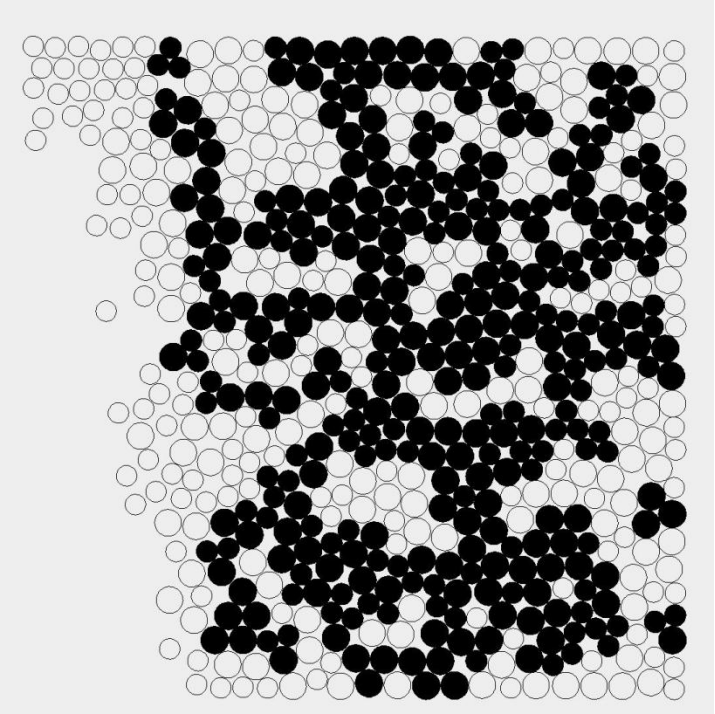

Figure 5.8-Graphical representation of the detected structure of the the image. Filled circles represent the crystallites detected in the image.

5.5 Assessment

With the centers located, we can calculate physical data contained in the image such as the average velocities of the spheres, the degree of crystallinity, and crystallite size distribution of the RCP structure. This degree of crystallinity measurement is the value that we wish to explore over the range of effective temperatures. With this information we hope to be able to better understand the structure of randomly close packed hard spheres at the effective temperature created by the experimental setup, and also how that structure changes under thermal forcing.

The velocity is the last piece of information calculated before the loop is incremented to the next image in order to measure the effective temperature. A sample of the velocity data for a 60 burst run can be seen in figures 5.9-5.12. The velocity histogram is shown for the four different speeds of the stepper motors. A different histogram is made for the two different bead sizes, and the two different directions are each given a separate histogram. The histogram is shown with a Gaussian curve in order to relate it to a Maxwellian velocity distribution. The variance $\sigma^2$is calculated for each velocity distribution and used to compare the statistical distribution of velocities to a Maxwellian distribution. This relation can be used to relate the variance of the distribution to an effective temperature using equations 5.3 and 5.4

$$\sigma^2 = \frac{1}{n}\sum_{k=0}^{n}(v_k - \bar{v})^2 = \frac{k_B T}{m} \tag{5.3}$$

$$f(v) = \frac{1}{\sqrt{2\pi\sigma^2}} e^{\frac{-(v-\bar{v})^2}{2\sigma^2}} \tag{5.4}$$

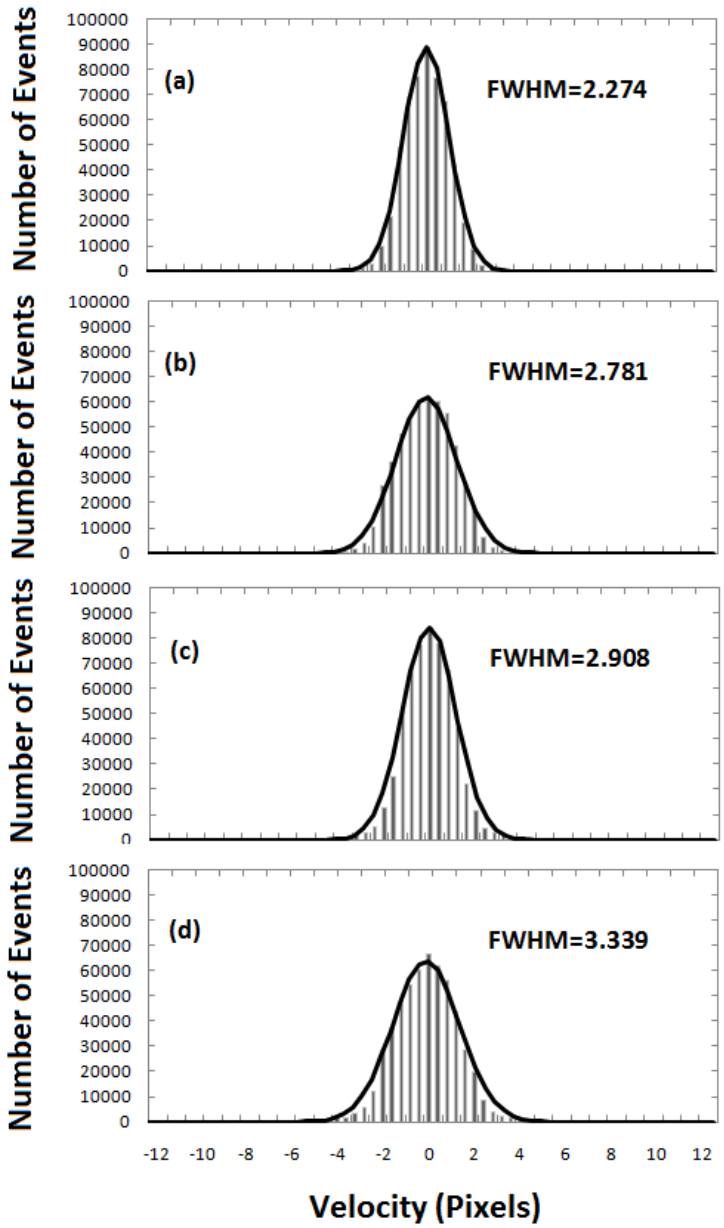

Figure 5.9-Velocity distributions for a 60 burst (1980 image) data run at the T* Speed setting. The driving algorithm was tuned to produce Gaussian distributions which are superimposed on top of the raw velocity data according to the calculated variance value. The figures are as follows: (a) large sphere x-direction (b) large sphere y-direction (c) small sphere x-direction (d) small sphere y-direction

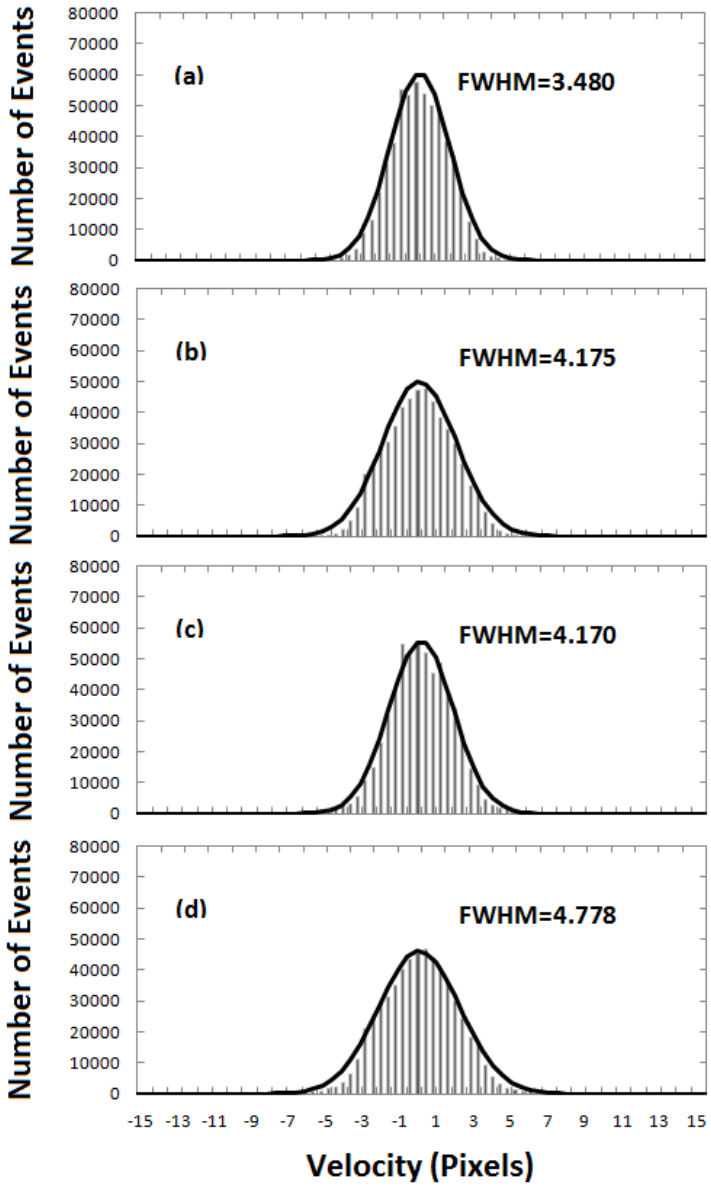

Figure 5.10-Velocity distributions for a 60 burst (1980 image) data run at the 2T* Speed setting. The driving algorithm was tuned to produce Gaussian distributions which are superimposed on top of the raw velocity data according to the calculated variance value. The figures are as follows: (a) large sphere x-direction (b) large sphere y-direction (c) small sphere x-direction (d) small sphere y-direction

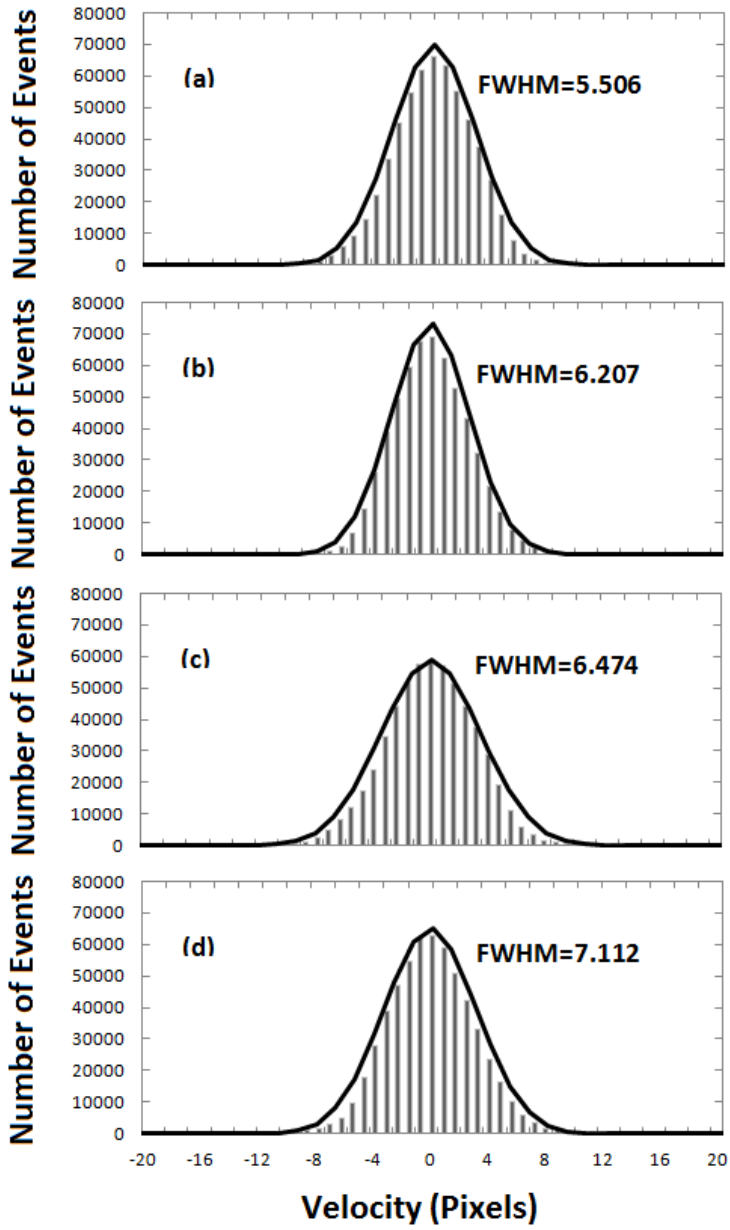

Figure 5.11- Velocity distributions for a 60 burst (1980 image) data run at the 4T* Speed setting. The driving algorithm was tuned to produce Gaussian distributions which are superimposed on top of the raw velocity data according to the calculated variance value. The figures are as follows: (a) large sphere x-direction (b) large sphere y-direction (c) small sphere x-direction (d) small sphere y-direction

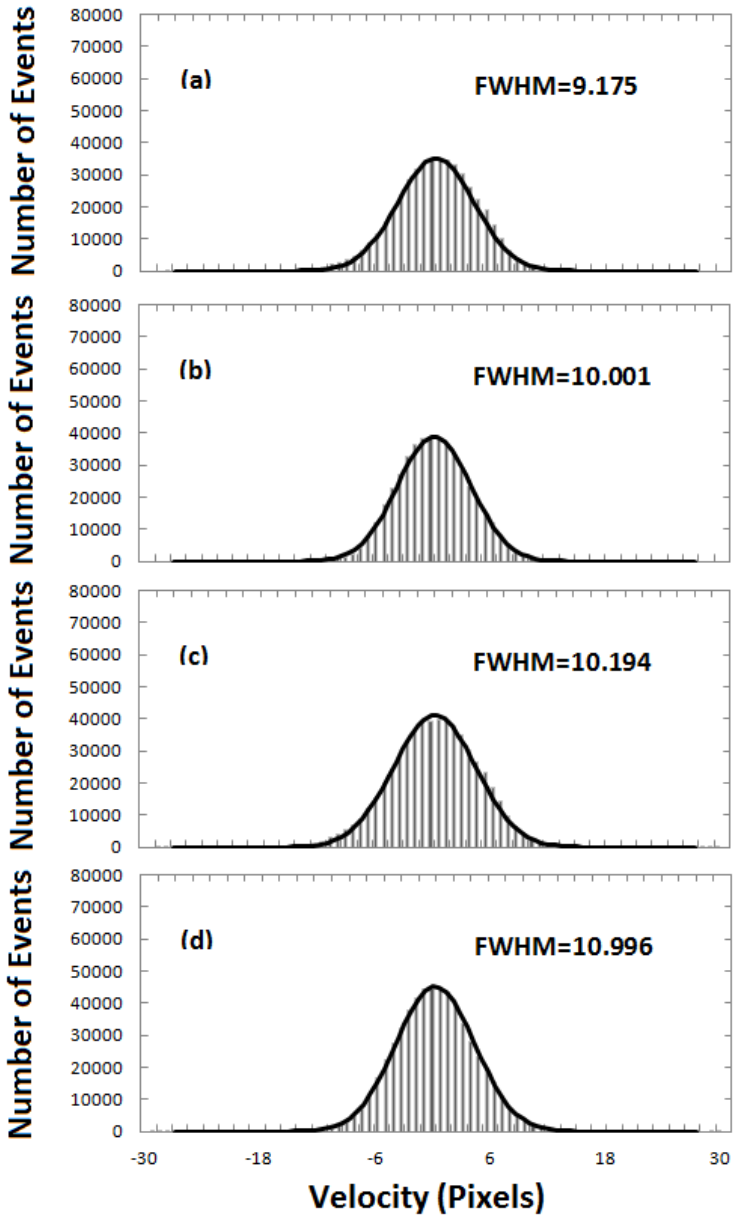

Figure 5.12- Velocity distributions for a 60 burst (1980 image) data run at the 8T* Speed setting. The driving algorithm was tuned to produce Gaussian distributions which are superimposed on top of the raw velocity data according to the calculated variance value. The figures are as follows: (a) large sphere x-direction (b) large sphere y-direction (c) small sphere x-direction (d) small sphere y-direction.

Figure 5.13 compares the measured degree of crystallinity in the RCP bed of binary spheres under four different intensities of the drive in 2-D. Sixty bursts of 33 successive images were analyzed in this example, which is a larger sample size than previous work [5]. The crystallites within each image have been identified. The degree of crystallinity is then obtained from the fraction of the total number of spheres that are part of the crystallites to the total number of spheres in the entire structure. Four histograms are shown for the degree of crystallinity, each corresponding to a unique driver intensity, i.e., at a temperature corresponding to the width of the Maxwellian velocity distribution: T^*, $2T^*$, $4T^*$ or $8T^*$. In each case the distribution has a characteristic width, consistent with the nature of RCP packing of spheres in 2-D. When the driver intensity is increased, i.e., the temperature is raised higher, the distribution of the degree of crystallinity shows movement toward smaller values but without significant changes in the width. As the temperature is doubled from T^* to $2T^*$, the histogram barely registers a movement. At higher temperatures at $4T^*$ and $8T^*$, however, the movement becomes significantly larger. This is interesting in that it seems to suggest the existence of a threshold temperature for morphology modification or possibly, the existence of an annealing temperature.

Taking a difference of an image frame from the next frame shows that the morphology transformation is primarily carried out by single spheres that are coming off a set of crystallites or attaching themselves to other crystallites. This is significant in that there is a pecking order in the way crystallites break up: single spheres separate from a crystallite more frequently than larger crystalline pieces. It also shows that the

higher the temperature gets, the more frequently the spheres break off the crystallites. Of course, the single spheres cluster to form new crystallites as well.

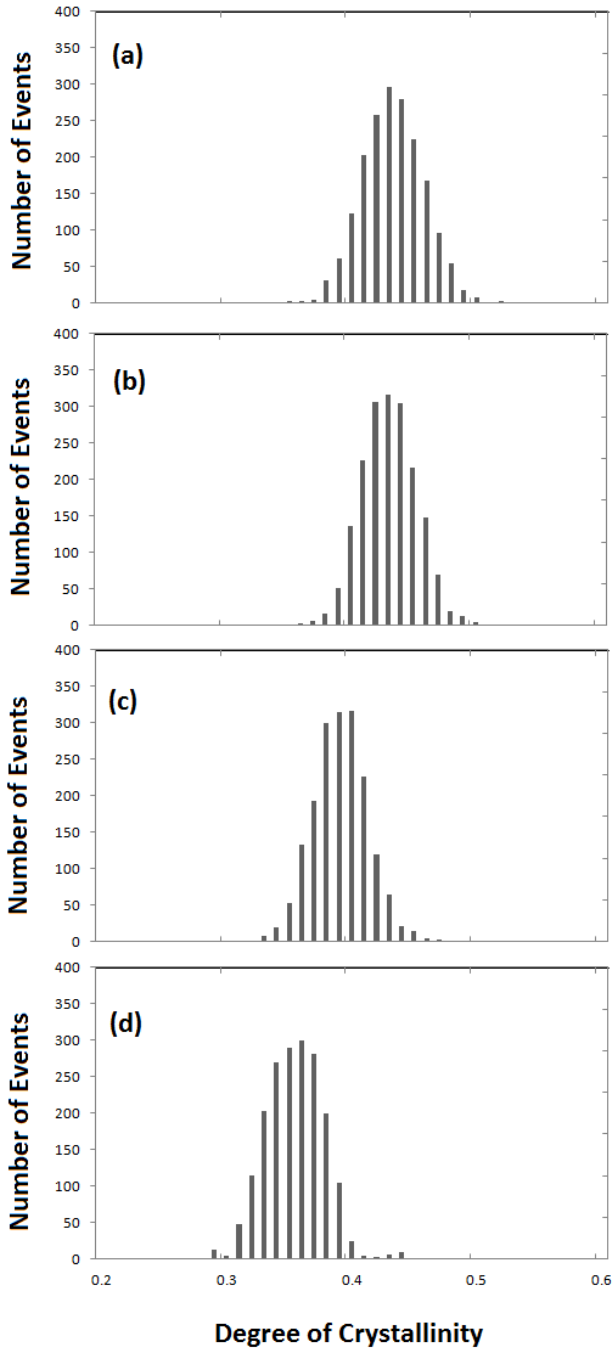

Figure 5.13-The degree of crystallinity for a 60 burst (1980 image) data run of an equal number mixture of two different size spheres is shown at four different effective temperatures: (a)T* ; (b)2T* ;(c)4T*; and 8T*.

5.6 Uncertainty in Measurements

The limiting factor in the accuracy of the Hough transform analysis is the assumed knowledge of the circle diameters in the image. The ball bearings used in the setup are machined to high precision, so any difference in size from sphere to sphere is assumed to be negligible. The main challenge in accurate measurement is assuring that the diameter used for all of these spheres is accurate. In regards to just sphere detection, an accurate diameter is not essential. Diameters over a certain range (often ±1 pixel) will still provide accurate detection within 1% of the total spheres in the image. Any analysis of the fine structure of the spheres requires accurate representation of the circle diameters. The identification of crystallites hinges on the ability to decide if two circles are in contact. The accuracy of the diameter plays a large role in determining the error in the degree of crystallinity, which is the basis of our structural morphology analysis. Figure 5.14 shows the fluctuation of the degree of crystallinity over various detection diameters; each point represents a burst of images at the 1x stepper motor speed run at varying Hough transform diameters.

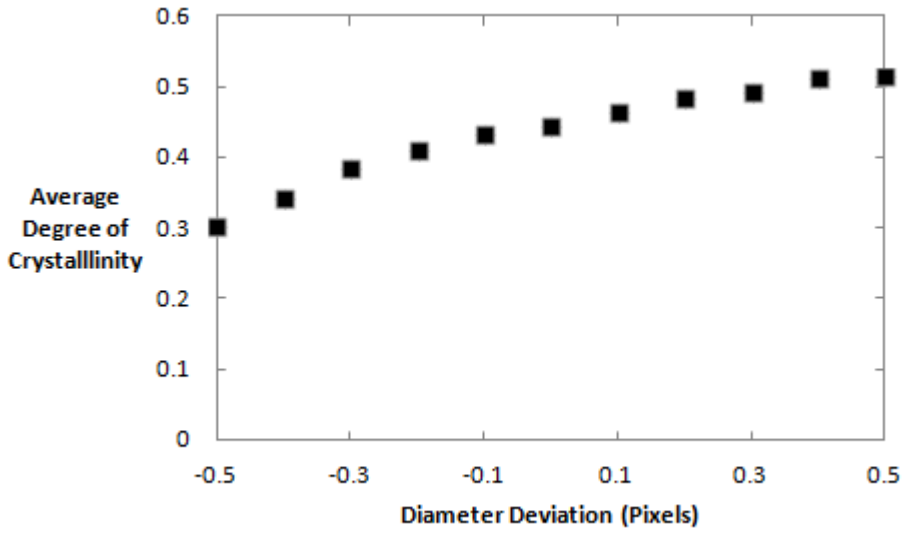

Figure 5.14-Affect of the Hough transform diameter on the calculated degree of crystallinity.

The fluctuation of the average degree of crystallinity over the deviation in diameters is significant, but it covers the range seen in the degree of crystallinity histogram seen in figure 5.13. Outside of this deviation window the detection starts to become less and less reliable. At small diameters the crystallinity begins to drop drastically as the contact between spheres becomes impossible under the misrepresented hard sphere structure. At larger diameters, the crystallinity raises as the spheres begin to overlap due to the spheres having diameters that are larger than their physical counterpart. As diameter deviations become significant, the detection of the circles becomes unreliable so that any analysis of the structure becomes wildly inaccurate. This figure also highlights the need for the precision used in the diameter

variable for the Hough transform analysis. Setting the diameter to the nearest integer would create large uncertainty in the degree of crystallinity analysis.

Chapter 6

Modeling Thermal Dissociation with the Law of Mass Action

6.1 Dissociation of Nano-Crystallites

In order to model the thermal dissociation of nano-crystallites seen in our mechanical oven experiment for a real disordered binary alloy specimen, we use a law of mass action treatment of the dissociation of nano-crystallites. To start we define the room temperature basis for the disordered binary alloy. As discussed before we model a disordered metallic binary alloy as a mixture of nano-crystallites and glassy atoms. At room temperature, we define the structure of the disordered binary alloy as having a certain mixture of these two states. The degree of crystallinity at the alloy composition will determine the ratio of glassy matter to nano-crystallites. To define the structure of the nano-crystallite particles we use the crystallite size distribution found through our experimental and simulation study for the composition transformed to 3-D. These parameters for the structure of the binary alloy are composition dependent, and we will use the lessons learned from the RCP modeling discussed in previous chapters to determine the room temperature structure of each disordered alloy we investigate.

The crystallite size distribution sets the initial amount of crystallites of a given size present in the disordered binary alloy. To model the thermal dissociation of a nano-crystallite in the alloy we start with a nano-crystallite of i particles. We are interested in calculating the percentage of i size crystallites that will thermally

dissociate j times and lose j particles from its surface. For any size crystallite we write the thermal dissociation equations for a mixture of crystallites as

$$\begin{gathered} C_i \rightarrow C_{i-1} + A \\ C_{i-1} \rightarrow C_{i-2} + A \\ \vdots \\ C_2 \rightarrow 2A \end{gathered} \tag{6.1}$$

For each thermal dissociation step, a nano-crystallite loses one atom from its surface and that atom then becomes part of the glassy matter (signified as A). This assumption is based on the fact that the lowest energy thermal dissociation reaction is one atom being removed from the surface of the nano-crystallite. A nano-crystallite breaking off chunks of atoms would be a much higher energy process. With this system of reactions for each size i nano-crystallite we have established a dissociation path for each i sized nano-crystallite to become i atoms in the glassy matter.

The equation of state for the system of crystallites and glassy matter is expressed in the total volume occupied by all nano-crystallites and glassy-state atoms, which expands according to the alloys thermal expansion coefficient ξ

$$V(N_0, T) = V_{C0}[1 + \xi_C(T - T_{rm})]^3 + V_{g0}\left[1 + \xi_g(T - T_{rm})\right]^3 \tag{6.2}$$

The equation of state depends on the system's state at room temperature. The system will be constrained to the number of particles at room temperature N_0 which is conserved for the alloy specimen.

$$N_0 = N_g + \sum_{s=2}^{s_{max}} D(R_S, T) N_S s \tag{6.3}$$

Where N_g is the number of glassy atoms, $D(R_S, T)$ is a formula representing the crystallite size distribution, N_S is the number of size s nano-crystallites in the specimen. The initial volume of the crystallite and glassy matter portions are, respectively

$$V_{C0} = \sum_{s=1}^{s_{max}} D(R_S, T) \frac{4\pi {R_S}^3}{3} \tag{6.4}$$

$$V_{g0} = N_g \frac{4\pi {R_g}^3}{3} \tag{6.5}$$

Where R_S is the crystallite radius and R_g is the radius of a glassy matter cluster. The morphology of the alloy structure represented by the degree of crystallinity and the crystallite size distribution changes the individual parameters in each of these equations dictating the evolution of the alloy specimen as a function of temperature.

6.2 Law of Mass Action Treatment

To model the dissociation of crystallites we start with the Gibbs free energy of the RCP system at room temperature. The Gibbs free energy of the system of nano-crystallites in qualified equilibrium is expressed with the formula

$$F(T, V, C_N, C_{N-1}, \dots\ C_2, A) = N_N \mu_N + N_{N-1} \mu_{N-1} + \cdots + N_2 \mu_2 + N_A \mu_A \tag{6.6}$$

where N_N is the number of size N crystallites (C_N), and μ_N is the chemical potential or the energy needed to add a C_N crystallite to the system. A global crystal would provide the ground state of the system, but the RCP state sits on the metastable branch

of the phase diagram in terms of packing fraction. The equilibrium treatment is justified because the energy differences between metastable RCP structures fall within kT. For a chemical reaction, the law of mass action tells us

$$\sum_{i\ reactants} \mu_i \upsilon_i = 0 \tag{6.7}$$

Or that the chemical potential for each reaction has to be conserved. For a dissociating crystallite the law of mass action can be written as

$$\begin{gathered} C_i \rightarrow C_{i-1} + A \\ \mu_i - \mu_{i-1} - \mu_A = 0 \end{gathered} \tag{6.8}$$

The chemical potential of the i sized nano-crystallite has to be equal to the summation of its resultant after the thermal dissociation reaction. To calculate the chemical potential for each part of the reaction equation we return to the Gibbs free energy and use the formula

$$\mu_i = \frac{\partial F}{\partial N_i} = -k_B T \ln(\frac{q_i}{N_i}) \tag{6.7}$$

Where k_B is the Boltzmann constant, T is the temperature of the binary alloy, N_i is the total number of i sized crystallites, and q_i is the partition function for an i sized crystallite. Combining this and the law of mass action give

$$-k_B T \sum_i \upsilon_i \ln(\frac{q_i}{N_i}) = 0 \tag{6.8}$$

$$\sum_i \ln(\frac{q_i}{N_i})^{\upsilon_i} = 0 \tag{6.9}$$

$$\ln \prod_i (\frac{q_i}{N_i})^{\upsilon_i} = 0 \tag{6.10}$$

$$\prod_i (\frac{q_i}{N_i})^{\upsilon_i} = 1 \tag{6.11}$$

For each reaction equation in the series of dissociation steps for an i sized crystallite the formula becomes

$$(\frac{q_N}{N_N})^1 (\frac{q_N}{N_N})^{-1} (\frac{q_N}{N_N})^{-1} = 1 \tag{6.12}$$

$$\frac{q_N}{q_{N-1} q_A} = \frac{N_N}{N_{N-1} N_A} \tag{6.13}$$

Equation 6.13 establishes an equation relating the partition function for each part of the thermal dissociation reaction equation to the number or occupation of each part of the dissociation. This treatment of each dissociation step will guide the morphology of the specimen through the temperature dependent partition functions.

6.3 The Degree of Dissociation

For the purpose of evaluating the temperature dependant behavior of the nano-crystallites we must evaluate the law of mass action equation for each of the dissociation reactions. To summarize the behavior of each of these reactions at a given temperature, we define the degree of dissociation. To calculate the degree of

dissociation, or the percentage of i size particles that will dissociate j times. We use the formula

$$\alpha_{i,j} = \frac{N_{i,i-1} + N_{i,i-2} + \cdots + N_{i,i-(j-1)}}{N_{i,i-1} + N_{i,i-2} + \cdots + N_{i,i-j}} \tag{6.14}$$

Since the distribution of nano-crystallites by size will be determined by the crystallite size distribution at a given atomic composition, each crystallite size will be populated at a certain number N. In order to track the evolution of the number of N sized nano-crystallites as a function of temperature the degree of dissociation is used. The degree of dissociation is the percentage of N sized crystallites that will dissociate j times. This expresses the remaining number of N sized crystallites after a temperature step, while also providing information on the size of the resulting crystallites after the dissociation. In order to write the law of mass action equation in terms of the degree of dissociation, the number of N sized crystallites is replaced with the degree of dissociation corresponding to that point in the full dissociation of the crystallite.

$$N_N = \left[\sum_{i=1}^{N} N_i\right] * (1 - \alpha_{N,1}) \tag{6.15}$$

$$N_{N-1} = \left[\sum_{i=1}^{N-1} N_i\right] * (1 - \alpha_{N,2}) \tag{6.16}$$

Substituting this into the law of mass action equation gives

$$\frac{q_N}{q_{N-1} q_A} = \frac{\left[\sum_{i=1}^{N} N_i\right] * (1 - \alpha_{N,1})}{\left[\sum_{i=1}^{N-1} N_i\right] * (1 - \alpha_{N,2}) N_A} \tag{6.17}$$

The right side of the equation can be simplified yielding

$$\frac{\left[\sum_{i=1}^{N} N_i\right]}{\left[\sum_{i=1}^{N-1} N_i\right]} = \frac{1}{\alpha_{N,1}} \tag{6.18}$$

$$\frac{(1-\alpha_{i,j})}{\alpha_{i,j}(1-\alpha_{i,j-1})} = \frac{N_A q_{i-j}}{q_{i-j-1} q_A} \tag{6.19}$$

For the system of crystallites present in the alloy specimen each crystallite size will have a set of degrees of dissociation equations to map the step by step dissociation of the crystallite. For example, a crystallite of size 10 will have a set of 9 coupled equations to calculate its degrees of dissociation

$$\begin{gathered}
\frac{(1-\alpha_{10,1})}{\alpha_{10,1}(1-\alpha_{10,2})} = \frac{N_A q_9}{q_8 q_A} \\
\vdots \\
\frac{(1-\alpha_{10,8})}{\alpha_{10,8}(1-\alpha_{10,9})} = \frac{N_A q_3}{q_2 q_A} \\
\frac{(1-\alpha_{10,9})}{\alpha_{10,9}} = \frac{N_A q_2}{{q_A}^2}
\end{gathered} \tag{6.20}$$

This series of coupled equations gives a method for calculating each degree of dissociation. It is dependent on knowing the partition function for each nano-crystallite as well as the glassy matter atoms in the alloy. With these partition functions we are still left with multiple unknowns for each of these equations. All of the equations in the set are coupled besides the last equation which has only one degree of dissociation. It is possible to calculate the degree of dissociation for this last equation directly. The other equations can then be solved sequentially with this result. The other unknown in these equations is the number of atoms in the glassy matter N_A. As nano-crystallites dissociate, this number will change as a function of temperature.

To start we initialize the variable and make the calculation to see if the number is accurate. This number of glassy atoms can then be reassessed and adjusted to correct after calculating the series of law of mass action equations.

6.4 Writing the Partition Function

To calculate the coupled law of mass action equations it is necessary to write the partition function for each part of the thermal dissociation reaction equation. The partition functions needs to consider all the energies present in a nano-crystallite of a certain size as well as the partition function for any atom in the glassy matter. For a single atom that dissociates and becomes part of the glassy matter the only energy remaining after the thermal dissociation is the translational energy or $q_{translation}$ which is written as

$$q_{translation} = V\left(\frac{2\pi m k_B T}{h^2}\right)^{3/2} \tag{6.21}$$

In this partition function, V is the volume of the alloy specimen, m is the mass of the atom in the glassy matter, T is the temperature of the specimen, k_B is Boltzmann's constant, and h is Planck's constant. For the other parts of the thermal dissociation reaction equation we need to write the partition function for an i sized nano-crystallite as well as the resulting i-1sized nano-crystallite. For an i-sized nano-crystallite the partition function will contain multiple relevant energies. The partition function is a product of the partition functions of these different energies

$$q_i = q_{translation} \cdot q_{rotational} \cdot q_{vibrational} \cdot q_{dissociation} \tag{6.21}$$

The larger crystallites will have both vibrational and rotational energies; these energies are not drastically changed by reducing the size of the nano-crystallite by 1 atom. These portions of the partition function will be present in both the numerator and the denominator when inserted into the law of mass action equation, and were ignored for this model. The most important part of the partition function for the thermal dissociation reaction equation is the energy overcame by the surface particle that dissociates. The surface particle will experience an attractive potential from the large crystallite which will decrease as it is dissociated to the glassy matter. We account for this change in attractive potential with the dissociation partition function

$$q_{dissociation} = e^{\frac{D_{0,i}}{k_B T}} \tag{6.22}$$

Where D_0 is the dissociation potential, or the potential that a surface atom on an i-sized nano-crystallite will have to overcome in order to thermally dissociate and join the glassy matter. The three partition functions for the reaction equations are then

$$q_{i-j} = V\left(\frac{2\pi(i-j+1)mk_BT}{h^2}\right)^{3/2} \cdot e^{\frac{D_{0,i-j+1}}{k_BT}} \tag{6.23}$$

$$q_{i-j-1} = V\left(\frac{2\pi(i-j)mk_BT}{h^2}\right)^{3/2} \tag{6.24}$$

$$q_A = V\left(\frac{2\pi mk_BT}{h^2}\right)^{3/2} \tag{6.25}$$

When we substitute these partition functions into the degree of dissociation law of mass action equation the result is

$$\frac{(1-\alpha_{i,j})}{\alpha_{i,j}(1-\alpha_{i,j})} = \frac{N_A V \left(\frac{2\pi(i-j+1)mk_BT}{h^2}\right)^{3/2} \cdot e^{\frac{D_{0,i-j+1}}{k_BT}}}{V\left(\frac{2\pi(i-j)mk_BT}{h^2}\right)^{3/2} V\left(\frac{2\pi mk_BT}{h^2}\right)^{3/2}} \tag{6.26}$$

The ratio then simplifies to

$$\frac{(1-\alpha_{i,j})}{\alpha_{i,j}(1-\alpha_{i,j-1})} = \frac{N_A}{V}\left(\frac{i-j+1}{i-j}\right)^{3/2}\left(\frac{2\pi mk_BT}{h^2}\right)^{-3/2} \cdot e^{\frac{D_{0,i-j+1}}{k_BT}} \tag{6.27}$$

For an i sized crystallite we will have i-1 coupled equations needed to calculate the degrees of dissociation. For the sized 10 example discussed previously the result is

$$\begin{gathered}
\frac{(1-\alpha_{10,1})}{\alpha_{10,1}(1-\alpha_{10,2})} = \frac{N_A}{V}\left(\frac{10}{9}\right)^{3/2}\left(\frac{2\pi mk_BT}{h^2}\right)^{-3/2} \cdot e^{\frac{D_{0,10}}{k_BT}} \\
\vdots \\
\frac{(1-\alpha_{10,8})}{\alpha_{10,8}(1-\alpha_{10,8})} = \frac{N_A}{V}\left(\frac{3}{2}\right)^{3/2}\left(\frac{2\pi mk_BT}{h^2}\right)^{-3/2} \cdot e^{\frac{D_{0,3}}{k_BT}} \\
\frac{(1-\alpha_{10,9})}{\alpha_{10,9}} = \frac{N_A}{V}\left(\frac{\pi mk_BT}{h^2}\right)^{-3/2} \cdot e^{\frac{D_{0,2}}{k_BT}}
\end{gathered} \tag{6.28}$$

6.5 Important Parameters

There are multiple unknowns in each of the law of mass action dissociation equations. The strategy is to directly solve the final degree of dissociation equation to solve for the probability of the i-sized crystallite fully dissociating. Once this degree of dissociation is calculated the rest of the coupled equations in the set can be solved directly. To directly solve the last equation it is essential to know the initial properties of the alloy. Since we are interested in the temperature dependence of the degree of

dissociation, we start by setting the initial parameters of the alloy at room temperature. For our model it is important to know how the atoms are contained in nano-crystallites versus how many are contained in glassy matter. This is covered by the degree of crystallinity for the composition of the alloy being modeled. In order to calculate each of the degree of dissociation equations, we also need to know how the nano-crystallites are distributed in terms of the number of atoms. This is covered through the use of the crystallite size distribution which is given by the atomic composition of the alloy. Through our experimental and simulated look at random close packing we explored a 2-D binary RCP system. The 2-D crystallite size distribution is transformed to a 3-D distribution for use in this model.

As a sample calculation we can look at the binary alloy $AuCu_3$, which has a 75% Small 25% Large atomic composition according to atomic radius. The structure of the alloy is modeled based on the 3-D crystallite size distribution. In order to determine the number of atoms contained in each crystallite size it is necessary to know the total number of atoms in the alloy specimen to be modeled. With the different sizes of the initial nano-crystallites known, the set of law of mass action equations can be written to model the temperature evolution of the structure. For each i-sized crystallite there will be i-1 reaction equations which will have to be written twice to account for the different atom types in the binary alloy. Many important parameters in the calculation have to be defined to calculate the degrees of dissociation for the alloy

$$\frac{(1-\alpha_{10,9})}{\alpha_{10,9}} = \frac{N_A}{V}\left(\frac{\pi m k_B T}{h^2}\right)^{-3/2} \cdot e^{\frac{D_{0,2}}{k_B T}} \tag{6.29}$$

Each set of degree of dissociation equations for an i-sized crystallite will depend on first calculating the last equation in the set. Certain parameters need to be initialized in order to calculate this last equation. Using $AuCu_3$as an example again, to calculate the series of law of mass action equations we need the mass of each atom type in the alloy($m_{copper} = 6.655\ x\ 10^{-23} g$, $m_{gold} = 3.27\ x\ 10^{-22} g$) We also need to know the relationship between the number of particles in the alloy specimen and the volume of the specimen. In order to calculate this we use the mass density of the alloy $\rho_{AuCu_3} = 10.9946 \frac{g}{cm^3}$ ($AuCu_3$parameters obtained from ref. [56])

$$N_{total} = \rho_m \ \frac{4}{3 * m_{copper} + m_{gold}} \tag{6.30}$$

$$N_{total} = 5.9793\ x\ 10^{22} \text{ for } 1cm^3 \text{ sample} \tag{6.31}$$

The relevant portion of the number of particles for the degree of dissociation calculation is the number of particles contained in the glassy matter. This can be obtained through the degree of crystallinity of the composition.

$$N_{Glass} = (1-\gamma) * N_{total} \tag{6.32}$$

$$\gamma = 0.316\ Crystallinity \tag{6.33}$$

$$N_{Glass} = 4.0898\ x\ 10^{22} \tag{6.34}$$

The remaining atoms will be contained in nano-crystallites.

$$N_{Crystal} = \gamma * N_{total} \tag{6.35}$$

$$N_{Crystal} = 1.8894\ x\ 10^{22} \tag{6.36}$$

These crystal atoms will be distributed into the different nano-crystallite sizes according to the crystallite size distribution of the atomic composition. This translates to an initial RCP structure shown in figure 6.1.

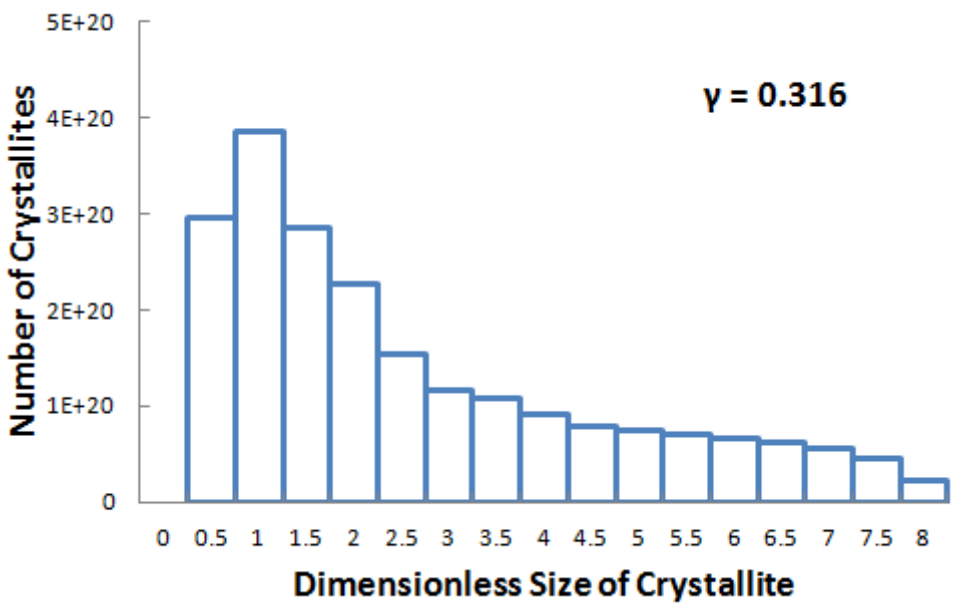

Figure 6.1-Initial room temperature crystallite size distribution for sample alloy $AuCu_3$

6.6 Calculating the Dissociation Potential

The last of the essential parameters for calculating the series of law of mass action equations is the dissociation potential $D_{0,i}$ which is the potential energy experienced by an atom on the surface of an i-sized nano-crystallite. For each alloy we calculate this based on structural information for the alloy as well as the Lennard-

Jones parameters for the atoms contained in the alloy. To begin, a nano-crystallite of a certain size is constructed based on the unit cell of the alloy. Our first assumption is to make each i-sized nano-crystallite spherical. Using the structural information for the alloy we are interested in we first build a cubic lattice of a certain size, we then remove any particle farther than a radius r from the center of the lattice. After the removal of these atoms we are left with a spherical nano-crystallite of a certain size as seen in figure 6.2.

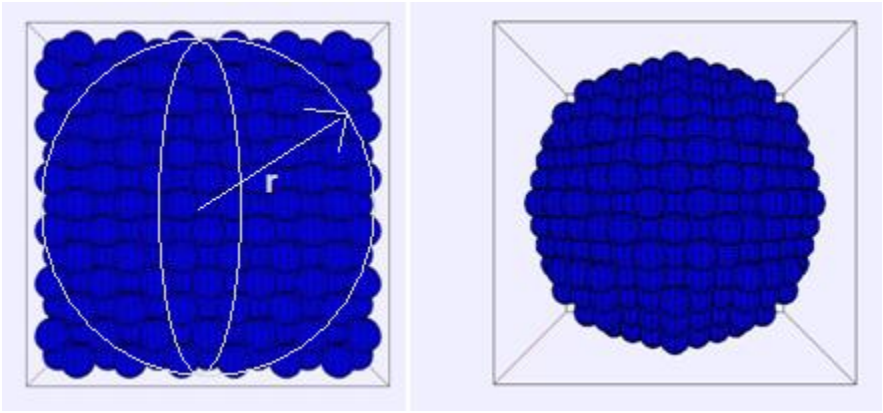

Figure 6.2- An example of a lattice built in accordance with the unit cell structure of the alloy. All atoms at a distance greater than the crystallite radius from the center of the lattice are removed in order to create a spherical crystallite.

After the spherical nano-crystallite is built, the surface particles are identified to be examined as potentially dissociated particles. All particles that are within a lattice constant of the surface of the sphere are defined as surface atoms. These particles will be the basis of the calculation; we want to know what potential these surface atoms experience in order to determine the dissociation potential for each

crystallite size. To find the dissociation potential we have to take into consideration the Lennard-Jones potential contribution from every other atom in the nano-crystallite. The total Lennard-Jones potential experienced by a surface particle is calculated with the formula

$$V_i = \sum_{j=1}^{N} 4\varepsilon_j \left[\left(\frac{\sigma_j}{r_{ij}} \right)^{12} - \left(\frac{\sigma_j}{r_{ij}} \right)^{6} \right] \tag{6.37}$$

The metallic element Lennard-Jones potential constants σ_j and ε_j are obtained through a quantum chemistry calculation [57]. In a binary nano-crystallite these quantum chemistry values will only cover the like atom interactions. To account for potential interactions between different atoms we use the Kong combination rules for Lennard-Jones potential parameters[58].

$$\epsilon_{ij}\sigma_{ij}{}^{6} = \left(\epsilon_{ii}\sigma_{ii}{}^{6}\epsilon_{jj}\sigma_{jj}{}^{6}\right)^{\frac{1}{2}} \tag{6.38}$$

$$\epsilon_{ij}\sigma_{ij}{}^{12} = \frac{\epsilon_{ii}\sigma_{ii}{}^{12}}{2^{13}} \left[1 + \left(\frac{\epsilon_{jj}\sigma_{jj}{}^{12}}{\epsilon_{ii}\sigma_{ii}{}^{12}} \right)^{\frac{1}{13}} \right]^{13} \tag{6.39}$$

For the example of an alloy composed of gold and copper in $AuCu_3$, the Lennard-Jones potential of a copper atom interacting with a gold atom can be seen in figure 6.4. This calculation will give information on the surface atom potential at its initial position. We are interested in the maximum potential seen as the particle is removed from the surface. In order to calculate the potential as the surface atom is removed we move the surface atom radially outward from the center of the nano-crystallite and calculate the total Lennard-Jones Potential at each radial position.

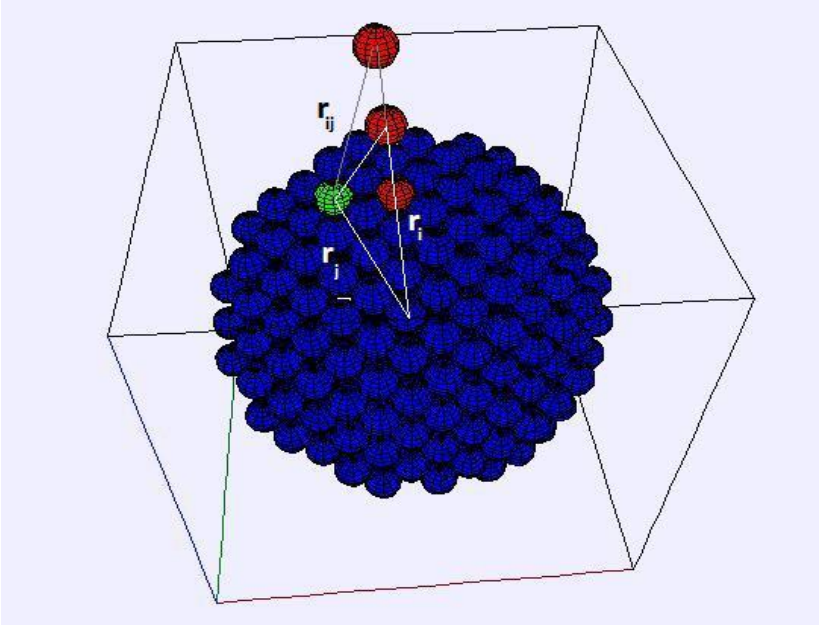

Figure 6.3- Visualization of the dissociation potential calculation for a surface atom on a spherical crystallite. The surface atom is moved radially outward in order to calculate the total potential the surface atoms experiences from the nano-crystallite as a function of distance. The dissociation potential is then the minimum of this calculated total potential function.

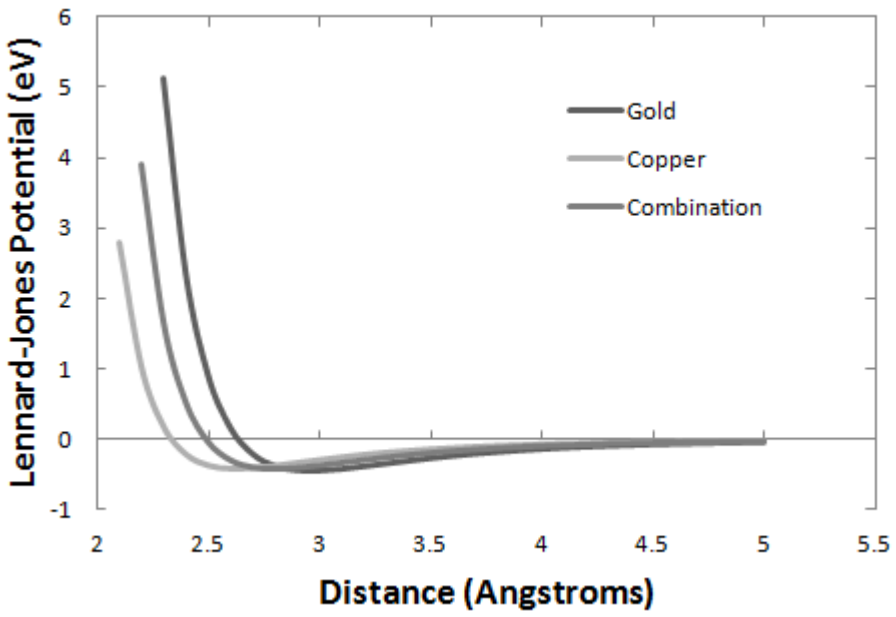

Figure 6.4-The three Lennard Jones-Potential interactions affecting a surface atom on a spherical crystallite of a gold copper alloy. Like atom interactions are calculated using the atom parameters [57], while different atoms interact via the Kong combination rules [58]

After calculating the surface atom Lennard-Jones potential as a function of the distance from its initial position, we define the dissociation potential as the minimum of the potential function. Since the surface contains many different atoms, we repeat this calculation for all the atoms on the surface and average over all the particles on the surface. For a binary nano-crystallite there will be different dissociation potentials for the different atom types on the surface of the nano-crystallite. The dissociation potential is calculated for both atom types, but the final dissociation potential value is calculated with a weighted average of the two atom types depending on the atomic composition of the binary alloy specimen.

6.7 Fitting the Dissociation Potential as a Function of Nano-Crystallite Size

Nano-Crystallites of different sizes are built and analyzed as described in chapter 6.6. An example of different nano-crystallite sizes based on the $AuCu_3$ alloy can be seen in figure 6.6. $AuCu_3$ has a face centered cubic lattice structure.

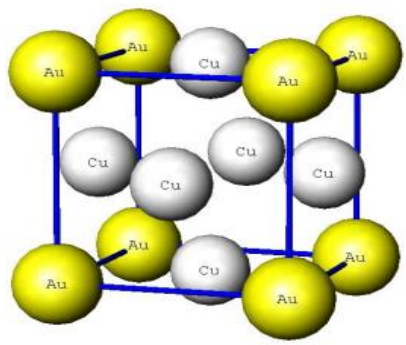

Figure 6.2-FCC unit cell structure for the $AuCu_3$ alloy, used as the lattice structure to build the spherical crystallite.

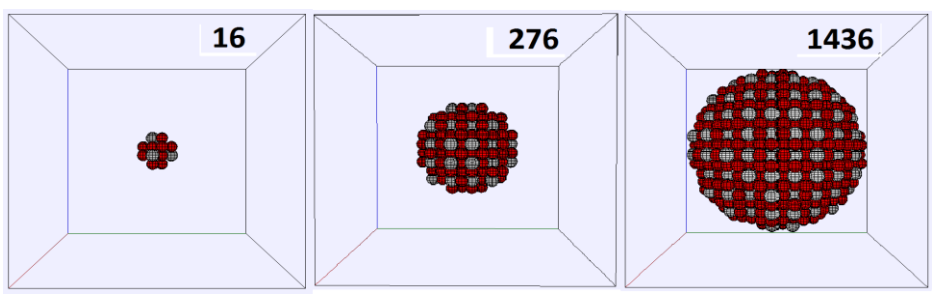

Figure 6.3-Different sized $AuCu_3$spherical nano-crystallites.

Viewing the dissociation potential as a function of nano-crystallite size will give a functional parameter to use in the law of mass action degree of dissociation equations needed to model the thermal evolution of the alloy. The dissociation potential grows as a function of nano-crystallite size to an asymptotic value for large

nano-crystallites. To fit the dissociation potential as a function of nano-crystallite size it is necessary to look at how the dissociation potential differs from the asymptotic value. When the dissociation potential values are subtracted from the large nano-crystallite dissociation potential and plotted on a log-log scale a linear relation between dissociation potential and nano-crystallite size is seen. To get the best fit possible for this functional dependence a constant is added to all values of dissociation potential until the best linear fit is obtained. This fit then represents a functional form for the dissociation potential of

$$D(i) = D(Large\ i) - A * i^B + Constant \tag{6.40}$$

An example of the fitting process for the alloy $AuCu_3$ can be seen in figure 6.7 and 6.8.

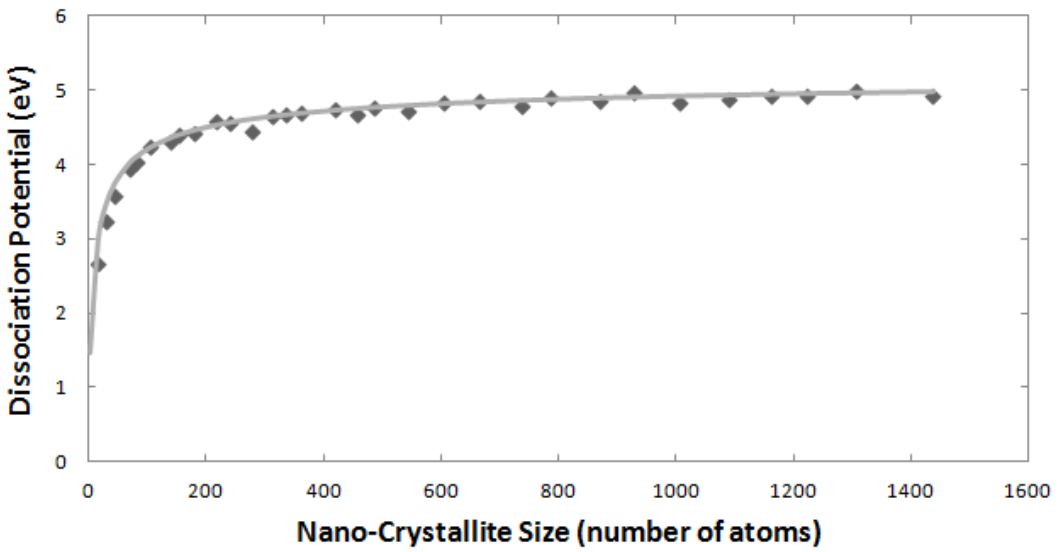

Figure 6.7-Example data for dissociation potential vs. nano-crystallite size for the $AuCu_3$ alloy. Data is fit with equation 6.40 for use in the law of mass action treatment of thermal dissociation.

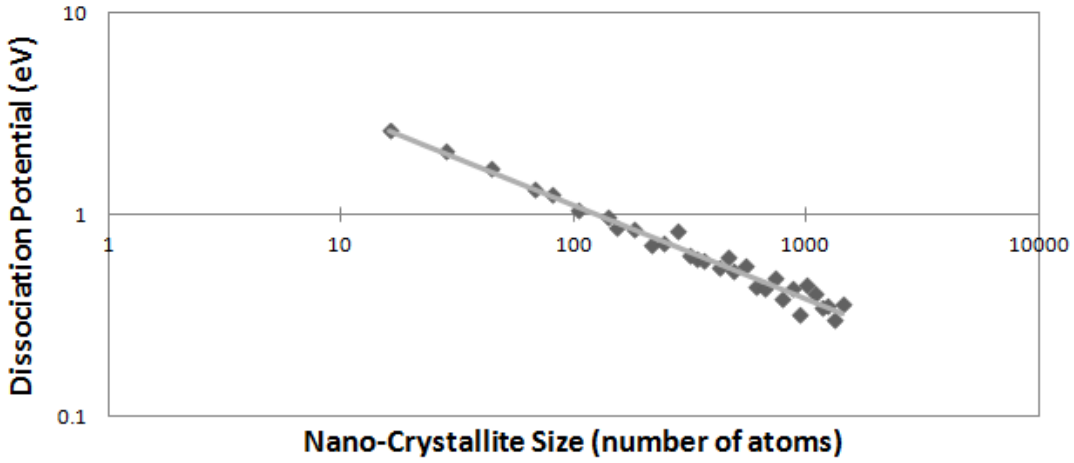

Figure 6.8 –Fitting technique for example data for dissociation potential vs. nano-crystallite size for the $AuCu_3$ alloy. A constant value is added to the data

subtracted from the asymptotic dissociation potential value in order to get the best linear fit when plotted on a log-log scale.

6.8 Morphology of the alloy structure

The initial parameters necessary to carry out the degree of dissociation law of mass action equation have been defined. In order to explore the morphology of the alloy as a function of the specimen temperature it is necessary to iterate the temperature and carry out the law of mass action calculation numerous times to explore the temperature dependant behavior of the structure. The value that is calculated through the series of equations is the degree of dissociation, or the amount of nano-crystallites of a certain size dissociating and changing sizes. Each degree of dissociation above a value of zero suggests a thermal dissociation reaction for a certain nano-crystallite size. The result of any reaction is a change in the nano-crystallite size distribution as well as a change in the total number of atoms in the glassy matter. Each nano-crystallite size will be adjusted after a series of degree of dissociation values are calculated. For each i-sized nano-crystallite the number of crystallites of that size will be adjusted by this formula

$$N_i = N_{i0}(1-\alpha_{i,1}) + \sum_{j>i}^{j=max} N_j(1-\alpha_{j,j-i+1})(\prod_{k=1}^{k=j-i} \alpha_{j,k}) \tag{6.41}$$

N_{i0} is the number of i-sized nano-crystallites before the temperature change. The first term in the formula accounts for any of the nano-crystallites that dissociated which will in turn decrease the number of that sized crystallites. The second term in the formula accounts for the nano-crystallites that have a size larger than i that go through

enough dissociation steps that they become i-sized nano-crystallites. This term will account for an increase in the number of i-sized crystallites. Figure 6.9 maps the result of calculating the series of degrees of dissociation for various temperatures of the $AuCu_3$ alloy. As can be seen, the crystallite size distribution evolves as the temperature is raised and the populations of the different nano-crystallite sizes are affected by the temperature change. As the nano-crystallites dissociate the total number of atoms contained in crystallites will decrease, this causes a change in the degree of crystallinity. The degree of crystallinity at each temperature step is shown in figure 6.9 as well.

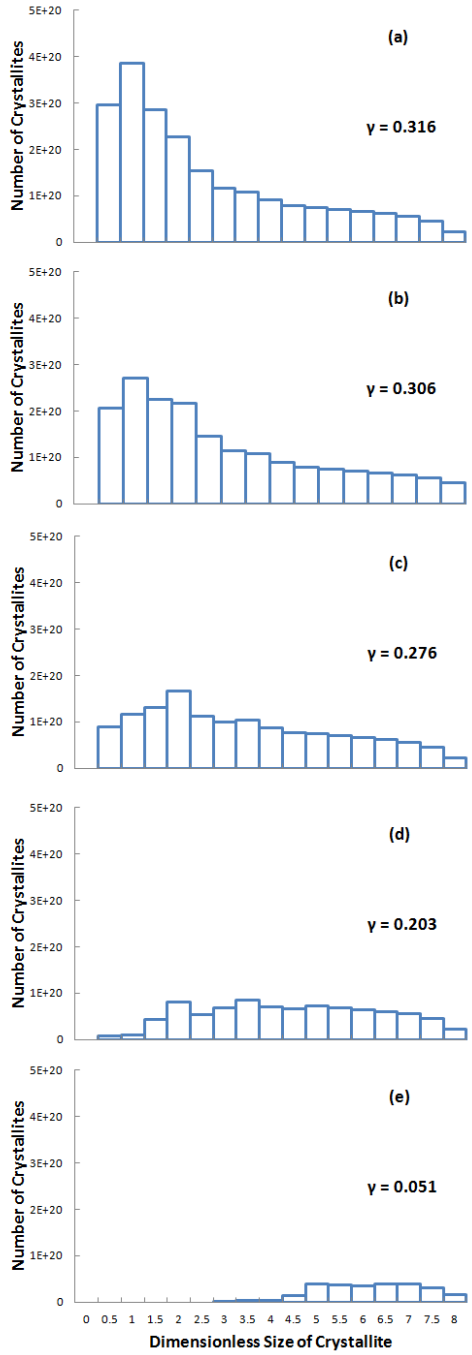

Figure 6.9-Evolution of the Crystallite Size distribution for the thermal dissociation of the $AuCu_3$alloy. The temperatures of each graph are as follows: (a) 300K (b) 1000K (c)1100K (d)1200K (e) 1400K. The degree of crystallinity of the structure γ is shown for each graph.

6.9 Number of Atoms in the Glassy Matter.

As the nano-crystallites in the alloy specimen dissociate due to temperature change, the number of atoms in the glassy matter increases. After each temperature step the number of atoms in the glassy matter increases according to the different degrees of dissociation through the formula

$$N_A = N_{A0} + \sum_{i=2}^{i=max} N_{i0} \prod_{j=1}^{j=i-1} \alpha_{i,j} + \sum_{i=2}^{i=max} (N_i - N_{i0}) \tag{6.42}$$

N_{A0} is the number of atoms in the glassy matter prior to the temperature step, because we are concerned with increases in temperature there will be no decrease in the number of atoms in the glassy matter. The first term in the formula accounts for all the atoms that were already in the glassy matter before the temperature increase. The second term accounts for all of the fully dissociated nano-crystallites. If a nano-crystallite fully dissociates there will be a resulting atom added to the glassy matter. The third term accounts for all the thermal dissociation reactions that happen after each temperature step. With each thermal dissociation reaction there will be an atom added to the glassy matter. The figure 6.10 shows the number of atoms in the glassy matter as a function of temperature for the alloy$AuCu_3$. The vertical line in figure 6.10 corresponds to the melting point of the alloy. As can be seen in figure 6.10 the thermal dissociation in the alloy shows good agreement with the alloys melting temperature.

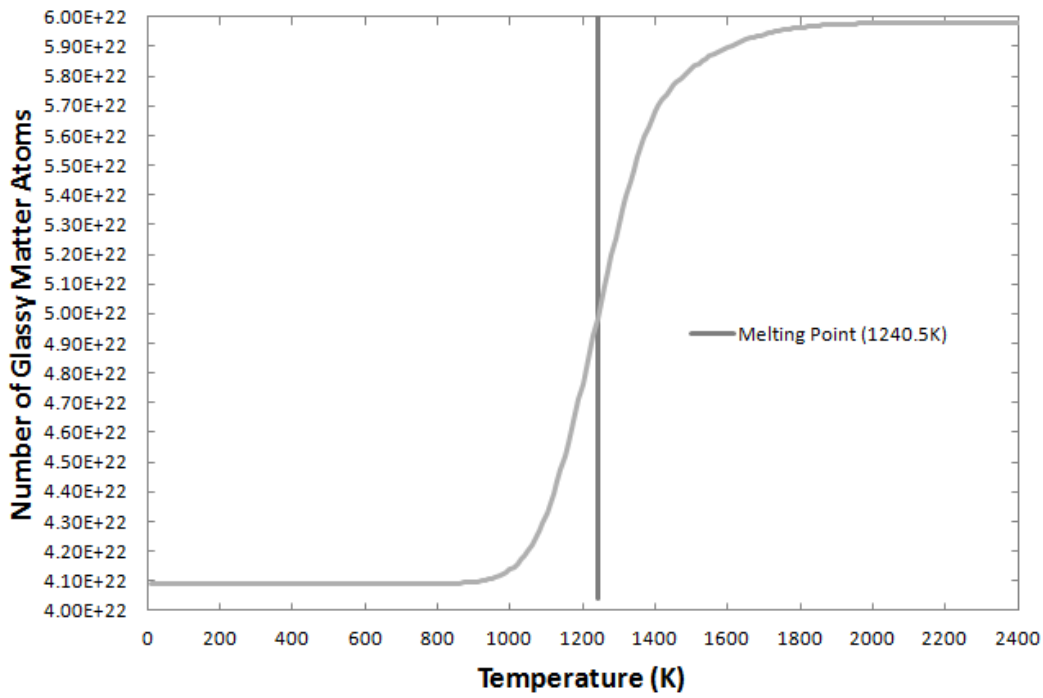

Figure 6.10-Evolution of the number of atoms in the glassy matter as a function of temperature for the $AuCu_3$alloy. The data shows a clear correlation with the alloys melting temperature.

The degree of crystallinity of the alloy also changes with temperature. In figure 6.11 it is seen that the degree of crystallinity drops from its initial value down to zero crystallinity at a sufficiently high temperature suggesting that all nano-crystallites have been thermally dissociated.

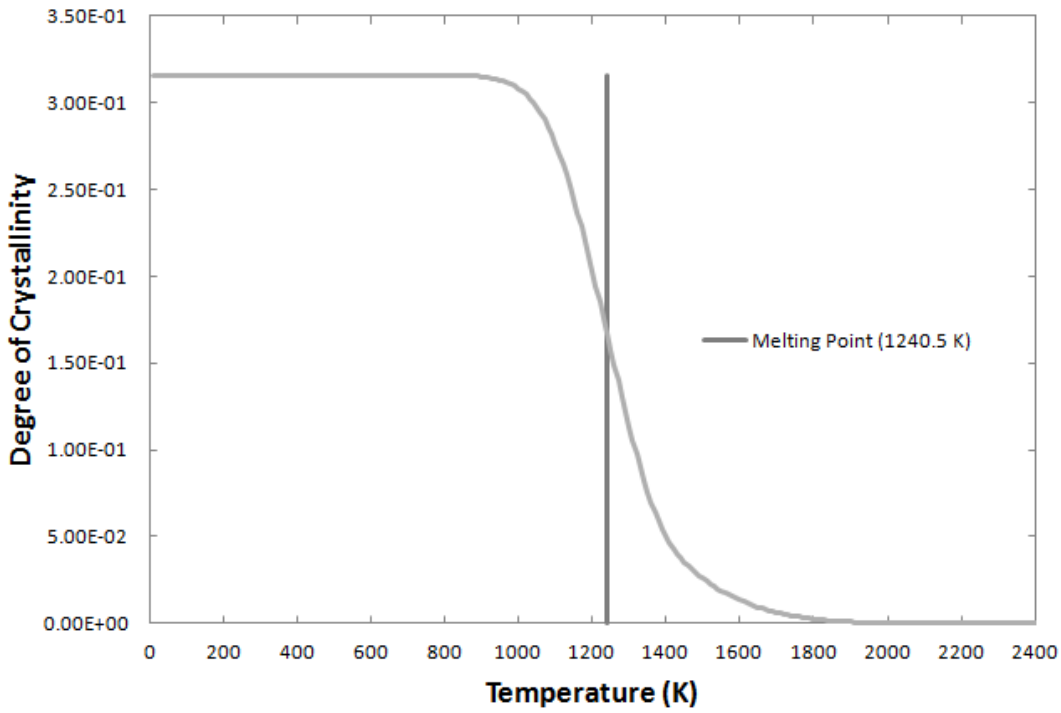

Figure 6.1- Evolution of the degree of crystallinity as a function of temperature for the $AuCu_3$ alloy. The data shows a clear correlation with the alloys melting temperature.

This technique was used to predict the melting temperature for various metallic elements and a group of six binary alloys. The results can be seen in the table below. The dissociation shows good agreement with the melting temperatures of the high temperature metals and alloys presented giving us confidence in the validity of our approach. The limited number of binary alloy calculation is due to the lack of unit cell structure information for binary alloys necessary for our approach. The presented technique provides a first principles approach to modeling the morphology of a disordered binary alloy under thermal forcing. The result's agreement with the

accepted melting temperatures of the metallic elements and binary alloys suggests success in portions of the assumptions made in this treatment of binary alloys.

Refractory Metallic Elements

Element	Symbol	σ (A)	ε (eV K)	Lattice Constant (A) [59]	Known Melting Point, K [59]	Predicted Melting Point (@ 50% Dissociation) K
Rhodium	Rh	2.4622	0.6699	3.8	2233	2360
Iridium	Ir	2.4839	0.8077	3.84	2716	2730
Vanadium	V	2.4391	0.6459	3.02	2163.15	2770
Tantalum	Ta	2.6819	0.9809	3.31	3269	2905
Chromium	Cr	2.3357	0.4988	2.88	2163	2245
Tungsten	W	2.5618	1.0644	3.16	3653	3840
Niobium	Nb	2.6819	0.9032	3.3	2741	3460
Hafnium	Hf	2.8917	0.750989	3.2	2423	2160
Rhenium	Re	2.518	0.945888	2.76	3453	2660
Ruthenium	Ru	2.4447	0.788343	2.7	2523	2410
Titanium	Ti	2.6841	0.568102	2.95	1948	1900
Zirconium	Zr	2.9318	0.738442	3.232	2125	2230

Binary Alloys

Alloy [56,60,61,62]	Lattice Constant (A)	Known Melting Point, K	Predicted Melting Point (@ 50% Dissociation) K
$AuCu_3$	3.74	1240.5	1320
AuCu	3.964 (2), 3.672	1183	1410
Au_3Cu	3.964	1151.5	1495
Al_3Ti	3.964	1340	1260
AlTi	4.00 (2), 4.075	1729	1935
$AlTi_3$	a=5.780,c=4.674*	1473	1360

Chapter 7

Thermophysical Property Calculation

7.1 Thermal Conductivity

The law of mass action model described in chapter 6 produces temperature based morphology of the structure of a disordered binary alloy. The morphology is represented by the evolution of the nano-crystallite size distribution. Relating this morphology to a model of thermal transport will involve taking into account the contributions from the separate portions of the structure. Thermal transport will be affected differently by the two different phases present in our structure. The disordered glassy matter will affect thermal transport in a different way than the ordered nano-crystallites. There is also the issue of boundaries between the two media that will contribute to the transfer of heat energy. These factors will have to be accounted for in an estimate of the thermal conductivity of our model structure. The different contributions would then change as the structure evolved with temperature and a temperature based evolution of the thermal conductivity could be established.

The thermal conductivity k of a solid is defined with respect to the solid-state flow of heat down a long rod with a temperature gradient $\frac{dT}{dx}$: as

$$j_U = -k\frac{dT}{dx} \tag{7.1}$$

Where j_U is the flux of thermal energy, or the energy transmitted across unit area per time unit. The process of thermal energy transfer is random, energy does not enter one

end of the specimen and proceed directly in a straight path to the other end. For our purposes we would like to be able to establish a simple approximation of thermal conductivity based on the structure model presented. The simplest form of the lattice thermal conductivity comes from the kinetic theory of gases

$$k = \frac{1}{3} C v l \tag{7.2}$$

Where C is the heat capacity per unit volume, v is the phonon velocity, and l is the phonon mean free path. The phonon mean free path is determined principally by two processes, geometrical scattering and scattering by other phonons. Collisions between different phonons come from the anharmonicity of the movements of the atoms. Geometrical scattering is limited by the crystal structure as well as imperfections in the crystals. Important collisions between phonons are the three-phonon umklapp processes that cause thermal resistivity; such processes are always possible in periodic lattices and are the phonon processes which affect the mean free path.

The contributions from electron transport also have to be considered in the thermal conductivity. The thermal conductivity of a Fermi gas is of the same form

$$k = \frac{1}{3} C_{el} v l \tag{7.3}$$

$$C_{el} = \frac{\pi^2 N {k_B}^2 T}{2 T_F} \tag{7.4}$$

N is the number of free electrons and T_F is the Fermi temperature. In pure metals the electronic contribution is the dominant part of the thermal conductivity at all temperatures. In impure metals and disordered alloys the electron mean free path is

reduced by collisions with impurities, and the contributions from both the electronic and lattice thermal conductivities are comparable. The nano-crystallites in the structure of the model alloy would have a thermal conductivity based on the basic theories of crystal transport as disorder in the structure is handled separately as glassy matter.

For glass, the thermal conductivity is very low, and is limited by the scale of the disorder of the structure. The structure of the disorder determines the mean free path of the dominant phonons in the glass. The key to predicting the differences in the contributions due to the ordered and disordered parts of our model structure will be to understand the structure of each portion of the structure. The important piece of information in characterizing this structure is the mean free path which will depend on the atomic spacing in the two phases of matter in the model alloy. To explore this spacing it would be beneficial to look at the pair distribution function for both the nano-crystallites and the glassy matter to determine how best to treat their mean free path difference.

7.2 Treatment of Boundaries

The treatment of the different parts of our structure is only part of the contribution to the thermal transport. The boundaries between the different sized nano-crystallites as well as the boundary between a nano-crystallite and glassy matter will also play a significant role in the thermal conductivity calculation. Previous work in binary liquids and granular physics treat the transfer of energy between two spheres in a way that could be beneficial in a prediction for our model [63]. The assumption is

that nano-crystallites are represented by spheres of a given size (which is represented in the crystallite size distribution). Glassy matter would also be assumed to be made up of small spheres. The heat transfer can then be based on the transfer of heat energy from sphere to sphere.

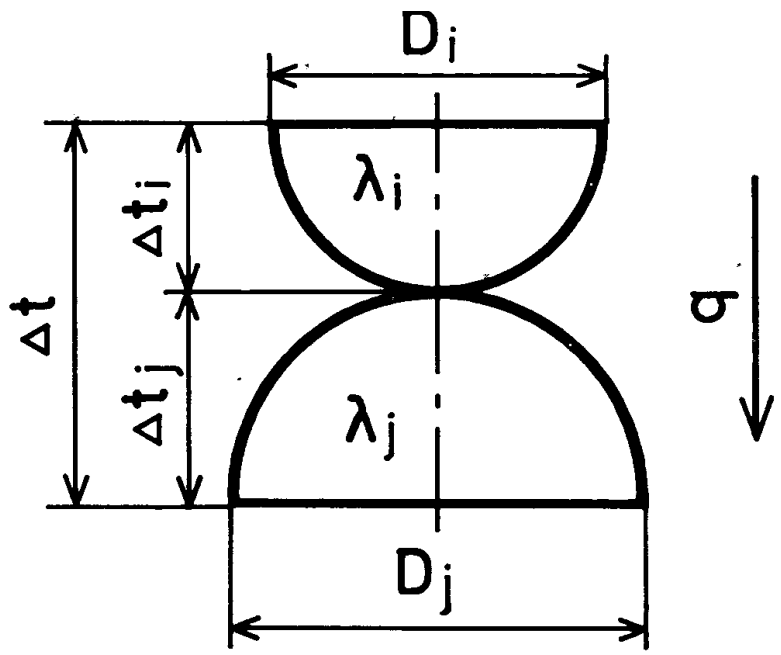

Figure 7.1-Diagram illustrating the heat transfer through a spherical contact point [63].

We assume that heat is transferred through contact points in the material between the different nano-crystallite sizes and the glassy matter. There will be many contact points, and each contact point will be evaluated and its contribution to the thermal conductivity will be included. For each contact point a unit cell of heat conduction is considered as seen in figure 7.1. The figure is a 2-D representation of

two hemispheres with one contact point. The heat flux q through particle i and j can be written as

$$q_i = \lambda_i \frac{\pi}{4} {D_i}^2 \frac{\Delta t_i}{D_i/2} \tag{7.5}$$

$$q_j = \lambda_j \frac{\pi}{4} {D_j}^2 \frac{\Delta t_j}{D_j/2} \tag{7.6}$$

Here, λ_i and λ_j are the thermal conductivities of the two spheres and Δt represents the difference in temperature. The contact point unit cell can be considered as a cylinder with a diameter equal to $\sqrt{D_i D_j}$, and a length of $\frac{D_i + D_j}{2}$. The heat flux through the cylindrical unit cell will be

$$q = \lambda_{ij} \frac{\pi}{4} \sqrt{D_i D_j}^2 \frac{\Delta t}{(D_i + D_j)/2} \tag{7.7}$$

In this equation λ_{ij} is the thermal conductivity through the cylinder, which for our purposes represents the thermal conductivity contribution from the boundary between two spheres. Rearranging these equations to solve for λ_{ij} gives

$$\lambda_{ij} = \left[\frac{D_i D_j}{D_i + D_j} \left(\frac{1}{D_i \lambda_i} + \frac{1}{D_j \lambda_j} \right) \right]^{-1} \tag{7.8}$$

This result provides a simple treatment of the contact points with only the size of the spheres and the thermal conductivity of the spheres being needed for calculation. For binary liquid mixtures this techniques has been used to predict the total thermal conductivity successfully. The treatment of our structure would involve different sized nano-crystallite spheres with a certain thermal conductivity, as well as glassy

spheres of a different conductivity and size. To calculate the total thermal conductivity, the calculation will have to account for all of the contact points present in the structure. The total conductivity will then be the average of the contributions of all of the contact points. The structure will have to be summarized in terms of the types of contact points present in the structure. This can be found with the crystallite size distribution and the degree of crystallinity as the number of each nano-crystallite size as well as the amount of glassy matter is contained in these parameters. Once the structural information is known, the calculation will then only require a prediction of the thermal conductivity of the nano-crystallites and glassy matter as discussed in Chapter 7.1

7.3 Treatment of the Glassy Matter

The nano-crystallites in the alloy are summarized based on effective radius by the crystallite size distribution. The glassy matter on the other hand is not characterized in a way that can easily translate to the spherical contact points necessary for the calculation discussed in the previous chapter. In order to summarize our structure as a group of different contact points, the size and treatment of the glassy matter has to be established for the structure. In order to predict how the thermal transport will be different from the structured nano-crystallites it is important to classify the density of the glassy matter. Since our structure is based on three dimensional random close packing, the total packing fraction of the structure is known. Experimental data is also available for the mass density of each alloy simulated. The density in the structure will fluctuate based on the two different

phases of the structure. The nano-crystallites will have their density determined by their unit cell structure for the alloy. The glassy matter then will compensate for the high nano-crystallite density by lowering the total density in relation to the atomic composition's degree of crystallinity. For a given alloy the relationship between the different mass densities will be

$$\rho_m = \gamma\rho_{Crystallite} + (1-\gamma)\rho_{Glass} \tag{7.9}$$

For the alloy $AuCu_3$, the face centered cubic unit cell is composed of one gold atom and three copper atoms which has a cubic dimension of 3.747 Angstroms. This calculates to be a mass density of $\rho_{Crystallite} = 12.223\frac{g}{cm^3}$. The experimental mass density of $AuCu_3$ is $\rho_m = 10.9946\frac{g}{cm^3}$. For the composition of $AuCu_3$ the degree of crystallinity is $\gamma = 0.316$. The mass density of the glassy matter in the alloy can then be calculated

$$\gamma\rho_{Crystallite} + (1-\gamma)\rho_{Glass} = 10.9946\frac{g}{cm^3} \tag{7.10}$$

$$\rho_{Glass} = 10.423\frac{g}{cm^3} \tag{7.11}$$

If we assume that the glass is just like the crystal structure with a larger lattice constant this relates to a lattice constant of 3.952 Angstroms, or an inflation of 5.48%. This information about the density of the glassy matter is important in determining the difference in thermal transport between the glassy matter and the nano-crystallites. In order to make a prediction of the thermal conductivity with our desired contact point technique it is necessary to break the glassy matter into a group of effective spheres

that will be in contact with the different sized nano-crystallites. In random close packing we know the packing fraction in three dimensions, we also know the packing fraction of a close packed system which is $\eta_{rcp} = 0.6366$ and $\eta_{cp} = 0.740$ respectively. Similarly to the treatment of the mass density, we can use this information to calculate the size of the glassy matter spheres in our structure that satisfy the packing fraction of random close packing in a way that creates the contact infrastructure necessary to facilitate our thermal conductivity calculation. The packing fraction for the glass can be written in term of the known values for the packing fraction as well as the degree of crystallinity

$$\eta_g = \frac{(1-\gamma)\eta_{rcp}\eta_{cp}}{\eta_{cp} - \gamma\eta_{rcp}} \tag{7.12}$$

Using this formula the size and number of effective glassy matter spheres can be calculated for a given alloy with the formula

$$\eta_g = \frac{N_{Glass}\frac{4}{3}\pi {r_{Glass}}^3}{V_{Glass}} \tag{7.13}$$

This formula can be used to find the size of the glassy matter spheres to be used in the thermal conductivity calculation, while the mass density can be used to predict the difference in individual thermal conductivity contributions from the nano-crystallites and the glassy matter.

Chapter 8

Summary and Conclusions

8.1 Summary and Conclusions

We have established a framework for modeling the morphology of disordered metallic binary alloys as a randomly closed packed structure. The RCP structure is treated as a mixture of nano-crystallites and glassy matter. The fraction of crystallite atoms contained in the structure defines the degree of crystallinity. The sizes of nano-crystallites in the structure are expressed through the crystallite size distribution. Both of these characterizations are dependent on composition, and provide an initial structure for the alloy at room temperature when transformed into 3-D. At six different compositions, RCP media in two dimensions were measured experimentally to establish the degree of crystallinity and the crystallite size distribution. To further explore 2-D RCP media, a numerical simulation code was developed to model arbitrary concentrations; the design was based on the information gained from the experimental measurement.

A mechanical oven experiment was developed to test the response of 2-D RCP media to thermal forcing. The analysis of the data gained from the mechanical oven experiment demonstrated dissociation of crystallites, and thus the evolution of the morphology of the medium, as the effective temperature of the temperature of the mechanical oven was raised.

The law of mass action was used to model this dissociation of crystallites in a disordered alloy specimen. The room temperature structure of the alloy specimen was

provided by the 2-D RCP crystallite size distribution after transformation to 3-D. Law of mass action equations are required for each possible dissociation step. The degree of dissociation is a measure of the amount of a certain size crystallite that dissociates at a certain temperature. Various alloy parameters are important in the calculation of each degree of dissociation equation, but the main determining parameter for the temperature at which dissociation happens is the dissociation potential for the nano-crystallite of a given size. This parameter was calculated by assuming a spherical crystallite and summing the potential energy seen by a surface atom on a crystallite due to all the other atoms. This potential was calculated based on Lennard-Jones parameters for the pairs of atoms in the alloy; the Kong combination rules were used for dissimilar pairs of atoms.

The success of the model is demonstrated by the accurate prediction of the melting temperature for disordered high temperature refractory metals as well as the binary alloy samples. The morphology of the disordered alloy structure can be predicted analytically at arbitrarily high temperature. This makes it possible to predict the thermal transport properties for disordered alloys as a function of temperature. The important features of our structure that pertain to a calculation of thermal conductiviy are the structure of the nano-crystallites and the glassy matter as well as the boundaries between them.

8.2 Future Research

Our morphology model leaves us with a lot of potential for further exploration. The number of calculation techniques discussed in chapter 7 requires further

evaluations to arrive at an eventual sample calculation needed to compare the validity with experimental results. A successful prediction of thermal conductivity can lead to predictions of other thermophysical properties such as thermal diffusivity, electrical resistivity, spectral emissivity, etc. The success of this model should also be thoroughly analyzed to discover what can be learned to further develop future theoretical alloy design approaches. Assumptions in this model should be tested in order to see the effect of factors deemed unimportant in this study. The partition function used is rather simple, considering many other energies in a crystallite. Rotational and vibrational energy states should be examined more closely, and the effect of a non-spherical crystallite on the dissociation potential should be examined.

A more in depth look at 3-D RCP media would also be beneficial. The experimental results presented here only offer a small glimpse of the many possible 2-D RCP structures. We only tested one ratio of particle sizes experimentally for the classification of the degree of crystallinity and crystallite size distribution of a 2-D RCP system. The size-ratio dependence of the RCP structure should be further explored in order to capture a more complete characterization of the structure.

List of References

[1] Kim, Y.W., “Routes To Development of Near-Surface Alloy Composition Anomaly,” *Int. J. Thermophysics* 26, 1051 (2005).

[2] Kim, Y.W., “Development of Transport Property-Composition Relationship by Thermal Modification of Alloy Composition Profile,” High Temperatures – High Pressures 38, 1 (2009).

[3] Kim, Y.W., “Surface Position-Resolved Thermophysical Properties for Metallic Alloys,” *Int. J. Thermophysics* 28, 732 (2007).

[4] Kim, Y.W., “Simultaneous Multitemperature Measurements of Thermal Diffusivity and Composition,” *Int. J. Thermophysics* 31, 926 (2010).

[5] Y.W. Kim and R.P. Cress, “Effects of thermal forcing on morphology of disordered binary metallic alloys: local equilibration and modification of near-surface elemental composition,” High Temperature – High Pressure 40 (2011).

[6]Gottstein G, Shvindlerman, Grain Boundary Migration in Metals: Thermodynamics, Kinetics, Applications, 2nd Edition. CRC Press. (2009).

[7] Cahill, David G. et al., “Nanoscale Thermal Transport”, *J. Appl. Phys.* 93, 793 (2003).

[8] Matsumoto, Shigenori, Tomoaki Nogawa, Takashi Shimada, and Nobuyasu Ito, "Heat Transport in a Random Packing of Hard Spheres." APS 060301 (2010)

[9] Ho, C. Y., M. W. Ackerman, K. Y. Wu, S. G. Oh, and T. N. Havill. "Thermal Conductivity of Ten Selected Binary Alloy Systems." *Journal of Physical and Chemical Reference Data* 7.3 (1978): 959.

[10] Smith, C. S., and E. W. Palmer. "Thermal and Electrical Conductivities of Copper Alloys."AIMME Inst. Metals. Div. Tech. Pub. 648 (1935): 1-19. Print.

[11] Jaeger, W., and H. Diesselhorst. "Heat Conduction, Electric Conduction, Heat Capacity, and Thermal Power of Some Metals." Wiss. Abh. Phys.-Tech. Reichsanst 3 (1900): 269-425.

[12] Smith, A. W. "The Thermal Conductivities of Alloys." Ohio State Univ. Exptl. Station Bull.31.61 (1925).

[13] Sager, G. F. "Investigation of the Thermal Conductivity of the System Copper-Nickel."Rensselaer Polytech. Inst. Bull. Eng. and Sci. Ser. 27 (1930): 3-48.

[14] Klemens, P. G. "Deviations from Matthiessen's Rule and the Lattice Thermal Conductivity of Alloys." *Aust. J. Phys* 12 (1959): 199-202

[15] Klemens, P. G. "Thermal Conductivity of Solids at Low Temperatures." *Handbuch Der Physic* 14 (1956): 198-281

[16] Mott, N. F. "A Discussion of the Transition Metals on the Basis of Quantum Mechanics."*Proceedings of the Physical Society* 47.4 (1935): 571-88.

[17] Mott, N. F., and H. ,. Jones. *The Theory of the Properties of Metals and Alloys,*. Oxford: Clarendon, 1936.

[18] Ho, C. Y., R. W. Powell, and P. W. Liley. "Thermal Conductivity of the Elements: A Comprehensive Review." *Supplement 1 to Volume 3 of the Journal of Physical and Chemical Reference Data* 796 (1974)

[19] Ho, C. Y. "Thermal Conductivity of the Elements." *J. Phys. Chem. Ref. Data,* 1 (1972): 279-421.

[20] Ho, C. Y., et al. "Thermoelectric Power of Ten Selected Binary Alloy Systems." *Thermal Conductivity* 18 (1985): 163-64.

[21] Ziman, J. M. Electrons and Phonons: The Theory of Transport Phenomena in Solids. Oxford: Clarendon, 1960.

[22]Klemens, P. G. "The Lattice Component of the Thermal Conductivity of Metals and Alloys."*Aust. J. Phys* 7 (1954): 57-63.

[23] Ackerman, M. W., and P. G. Klemens. "Lattice Thermal Resistivity Due to Dense Arrays of Dislocations." *Physical Review B* 3.8 (1971): 2375-379.

[24] Pippard, A. B. "Theory of Ultrasonic Attenuation in Metals and Magneto-Acoustic Oscillations." *Proceedings of the Royal Society A: Mathematical, Physical and Engineering Sciences* 257.1289 (1960): 165-93.

[25] Klemens, P. G. "Thermal Resistance Due to Point Defects at High Temperatures." *Physical Review* 119.2 (1960): 507-09.

[26] Callaway, Joseph. "Model for Lattice Thermal Conductivity at Low Temperatures." *Physical Review* 113.4 (1959): 1046-051. Print.

[27] Ackerman, M. W. "Phonon Scattering by Impurity Atmospheres Surrounding Dislocations. III. Combined Mass and Distortion Scattering." *Journal of Applied Physics* 42.3 (1971): 968.

[28] Maurizio, C., et. al. "Deviation from the Virtual Crystal Approximation in Disordered Au–Cu Alloy Nanocrystals: EXAFS and GIXRD Investigation." *Nuclear Instruments and Methods in Physics Research Section B: Beam Interactions with Materials and Atoms* 200 (2003): 178-84.

[29] Y. W. Kim, High Temp. Sci. 26, 59 (1990).

[30] Y. W. Kim, Int. J. Thermophysics 14, 397 (1993).

[31] Van Swygenhoven, H., and J. Weertman. "Deformation in Nanocrystalline Metals." *Materials Today* 9.5 (2006): 24-31.

[32] Tongjai, Chookajorn, Heather A. Murdoch, and Christopher A. Schuh. "Design of Stable Nanocrystalline Alloys." *Science* 337.6097 (2012): 951-54.

[33] Von Arx, Martin, Oliver Paul, and Henry Baltes. "Process-Dependent Thin-Film Thermal Conductivities for Thermal CMOS MEMS." *Journal of Microelectromechanical Systems* 9.1 (2000).

[34] Cahill, David G. et al., "Nanoscale Thermal Transport", *J. Appl. Phys.* **93**, 793 (2003).

[35] C. J. Glassbrenner and G. A. Slack, Phys. Rev. A 134, 1058 ~1964.

[36] M. Asheghi, K. Kurabayashi, K. E. Goodson, R. Kasnavi, and J. D. Plummer, in *Proceedings of the 33rd ASME/AIChE National Heat Transfer Conference* ~Asme, New York, 1999.

[37] S. Uma, A. D. McConnell, M. Asheghi, K. Kurabayashi, and K. E. Goodson, Int. J. Thermophys. **22**, 605 ~2001.

[38] A. D. McConnell, U. Srinivasan, M. Asheghi, and K. E. Goodson, J. Microelectromech. Syst. **10**, 360 ~2001.

[39] Weissmuller, J. "Alloy Effects in Nanostructures." *Nanostructured Materials* 3.1-6 (1993): 261-72.

[40] Barker, J. A., M. R. Hoare, and J. L. Finney. "Relaxation of the Bernal Model." *Nature* **257**, 120 (1975).

[41] W. O. Smith, P. D. Foote, and P. F. Busang, Phys. Rev.34, 1271 (1929).

[42] J. D. Bernal, Proc. R. Soc. London, Ser. A 280, 299(1964).

[43] C. H. Bennett, J.Appl. Phys. 43, 2727 (1972).

[44] C. A. Rogers, Packing and Covering (Cambridge University Press, Cambridge, 1964).

[45] J. L. Finney, Proc. R. Soc. London, Ser. A 319, 479 (1970).

[46] G. D. Scott and D. M. Kilgour, Br. J. Appl. Phys. (J. Phys. D) 2, 863 (1969).

[47] Berryman, J. G. "Random Close Packing of Hard Spheres and Disks." *Phys. Rev.* **A27**, 1053 (1983).

[48] Rintoul, M. D., and S. Torquato. "Hard-sphere Statistics along the Metastable Amorphous Branch." *Phys. Rev*. **A 58,** 532 (1998).

[49] Lubachevsky, B. D., and F. H. Stillinger. "Geometric Properties of Random Disk Packings" *J. Stat. Phys.* **60** (1990).

[50] Lu, G., and X. SIll. "Computer Simulation of Isostatic Powder Compaction by Random Packing of Monosized Particles." *J. Mat. Sci. Letters* **13,** 1709 (1994).

[51] Finney, J. L. "Modelling Structures of Amorphous Metals and Alloys." *Nature* **266**, 309 (1977).

[52] Brostow, Witold, Mieczyslaw Chybicki, Robert Laskowski, and Jaroslaw Rybicki. "Voronoi Polyhedra and Delaunay Simplexes in the Structural Analysis of Molecular-dynamics-simulated Materials." *Phys. Rev.* **B 57,** 21 (1998).

[53] Torquato, S., T. M. Truskett, and P. G. Debenedetti. "Is Random Close Packing of Spheres Well Defined?" *Phys. Rev. Lett.* **84,** 2064 (2000).

[54] Anikeenko, A. V., and N. N. Medvedev. "Structural and Entropic Insights into the Nature of the Random-close-packing Limit." *Phys. Rev.* **E 77**, 031101 (2008).

[55] Anikeenko, A. V., and N. N. Medvedev. "Polytetrahedral Nature of the Dense Disordered Packings of Hard Spheres." *Phys. Rev. Lett.* **98**, 235504 (2007).

[56] Han, X. J., M. Chen, and Z. Y. Guo. "Thermophysical Properties of Undercooled Liquid Au–Cu Alloys from Molecular Dynamics Simulations." *Journal of Physics: Condensed Matter* 16.6 (2004): 705-13.

[57] Zhen, Shu, and G. J. Davies. "Calculation of the Lennard-Jones N-m Potential Energy Parameters for Metals." *Phys. Stat. Sol.* 78.595 (1983)

[58] Kong, Chang Lyoul. "Combining Rules for Intermolecular Potential Parameters. II. Rules for the Lennard-Jones (12–6) Potential and the Morse Potential." *The Journal of Chemical Physics* 59.5 (1973): 2464.

[59] Lide, David R. *CRC Handbook of Chemistry and Physics: A Ready-reference Book of Chemical and Physical Data*. N.p.: CRC

[60] Okamoto, H., D. J. Chakrabarti, D. E. Laughlin, and T. B. Massalski. "The Au−Cu (Gold-Copper) System." *Journal of Phase Equilibria* 8.5 (1987): 454-74.

[61] Batalu, D., Georgeta Cosmeleata, and A. Aloman. "Critical Analysis of the Ti-Al Phase Diagrams." *U. P. B. Sci. Bull.* B 68.4 (2006): n. pag.

[62] Djanarthany, S., J. C. Viala, and J. Bouix. "An Overview of Monolithic Titanium Aluminides Based on Ti3Al and TiAl." *Materials Chemistry and Physics* 72.3 (2001): 301-19.

[63] Tobitani, Atsumi, and Tatsuo Tanaka. "Predicting Thermal Conductivity of Binary Liquid Mixtures on Basis of Coordination Number." *The Canadian Journal of Chemical Engineering* 65.2 (1987): 321-28.

Vita

Ryan Cress was born in the year 1986 in the state of Montana to Bryan and Laura Cress. He Attended Moravian College in Bethlehem, Pennsylvania and received a Bachelors of Science with honors in Physics in May, 2008. In July of 2008 he began researching at Lehigh University under the direction of Professor Y.W. Kim. In September of 2008 he entered the graduate program at Lehigh University. He received an M.S. in Physics in December, 2009. While at Lehigh University he worked as a teaching assistant for 5 years.